Study of Electronic Transport Through Carbon Nanotubes and Their Performance in Electronic Circuits

by

Amr Ahmed Essawi Saleh

A Thesis Submitted to the
Faculty of Engineering at Cairo University
in Partial Fulfillment of the
Requirements for the Degree of
MASTER OF SCIENCE
in
Engineering Physics

FACULTY OF ENGINEERING, CAIRO UNIVERSITY
GIZA, EGYPT
July 2008

Study of Electronic Transport Through Carbon Nanotubes and Their Performance in Electronic Circuits

by

Amr Ahmed Essawi Saleh

A Thesis Submitted to the
Faculty of Engineering at Cairo University
in Partial Fulfillment of the
Requirements for the Degree of
MASTER OF SCIENCE
in
Engineering Physics

Under the Supervision of

Nadia H. Rafat   Hossam A. H. Fahmy

Associate Professor   Assistant Professor
Math. and Eng. Physics Dept.   Elec. and Com. Dept.

FACULTY OF ENGINEERING, CAIRO UNIVERSITY
GIZA, EGYPT
July 2008

Study of Electronic Transport Through Carbon Nanotubes and Their Performance in Electronic Circuits

by

Amr Ahmed Essawi Saleh

A Thesis Submitted to the
Faculty of Engineering at Cairo University
in Partial Fulfillment of the
Requirements for the Degree of
MASTER OF SCIENCE
in
Engineering Physics

Approved by the
Examining Committee

_____
Prof. Dr. Salah El-Din El-Nahawy (Member)

_____
Prof. Dr. Amr Shaarawi (Member)

_____
Dr. Nadia H. Rafat (Thesis Main Advisor)

FACULTY OF ENGINEERING, CAIRO UNIVERSITY
GIZA, EGYPT
July 2008

Abstract

Scaling down of CMOS transistors dimensions is the major factor responsible for the great advancements in today's electronics industry. Such scaling can not continue forever. Today, we are very close to the physical limits of the dimensional scaling. Thus, different materials and architectures were introduced to extend CMOS era or even replace it. Among the very promising candidates we find Carbon nanotubes. This work aims at evaluating CNTs as electronic devices and suggests a novel method to use CNTs as interconnects.

Most of recent studies tend to evaluate individual CNT devices. In order to evaluate CNT devices accurately, we should study their performance in electronic circuits as well. To achieve this goal, we developed a circuit simulation environment using Matlab. We integrated an already developed SB CNTFET device model in this environment and studied the characteristics of the inverter gate. After adjusting the flat band voltage of the transistors, simulations showed that this transistor is a good choice for high performance applications.

As interconnects, CNTs are also very promising. Most studies concentrate on fabricating bundles of CNTs to replace copper interconnects. In this thesis, we introduced another possible method to use single CNT as an interconnect. Starting from the basic physics of CNTs, we stated that it is possible to multiplex different signals simultaneously and transmit them along the tube. We tried two different types of wave packets propagating along the tube: wrapped-around packet and pulsed packet. The wrapped around packet can be constructed using a single CNT energy mode. In order to send different packets with different modes

simultaneously through the same tube, we will need to develop a receiver that can differentiate between packets according to their energy modes. The other packet type is a multimode packet, but it allows for multiplexing different signals by dividing the circumference of the CNT into segments such that each segment carry a packet. We expect that developing transmitters and receivers for such packet would be simpler.

The thesis is organized as follows: In chapter 1 we introduce the difficulties facing dimensional scaling down of CMOS, its physical limits and suggested solutions to overcome this problem. A quick review for the basic properties of CNTs and their structure is available in chapter 2. The circuit simulation procedure we developed for SB CNTFET is described clearly in chapter 3. This chapter contains also our simulation results for SB CNTFET inverter. In chapters 4 and 5 we describe in details our analysis to find out the possibility of transmitting different wave packets simultaneously over the CNT. Chapter 6 summarizes our conclusion and introduces some open points that still need further research.

Acknowledgment

I would like to express my heartiest gratitude to my thesis advisors: Dr. Nadia Rafat and Dr. Hossam Fahmy.

I can not find suitable words to describe the unlimited support I got from Dr. Nadia throughout my work even during the moments of depression I faced. Her continuous encouragement pushed me to do my best in every moment of this research. My experience of working as a student of Dr. Hossam is another invaluable treasure. His insight into science and life inspired me and guided me to discover new horizons in this world and even inside me.

I am also very grateful to the great teacher and talented researcher prof. Ahmed Alaa Aboulsaoud who devoted a lot of his precious time to this work. His effective advices added significant weight to this work.

I would like also to thank Engineer Mohamed Nabil, PhD student at University of California Santa Barbara, and Engineer Tamer Ashour Ali, PhD student at Rice University, for supporting me with a lot of papers I needed. I am also indebted to Engineer Hazem Nassif for his invaluable help. I would also like to thank my study partner and my friend Osman Sayed and all staff in Math. and Engineering Physics Department.

I do not know how to express my gratefulness and appreciation to my beloved parents who taught me nearly everything in this life. None of this work would have been possible without them. Finally, I want to say thank you to my sister and my brother who gave me lots of support during this work.

Contents

List of Figures

Chapter 1

Introduction

The major factor responsible for the great development in electronic applications in the last few decades is the Integrated Circuits (IC). The first IC was introduced to the scientific and industrial society at the beginning of the 1960s. Since then, ICs experienced great advancements in their capabilities and performance. Such improvements were achieved by integrating more transistors on the same chip and scaling down the transistor dimensions. In 1965, Gordon Moore — co-founder of Intel Corporation — predicted that the number of transistors on a chip will double about every two years [1]. Later, this prediction was named as Moore's law. The validity of this law was kept successfully for decades. However, it is expected that this exponential growth will continue for only one or two decades. This pessimistic vision arises from the limitation of the CMOS technology which is the heart of today's ICs. An expected progress in CMOS technology is shown in Fig.(1.1). As depicted in the figure, we are facing two different challenges. First, we have to keep CMOS technology progress by pushing it toward its real physical limits. Then, we have to find a new technology with completely different concepts to start a new generation of development. In this chapter we will summarize challenges facing CMOS scaling and its physical limits. Then, we will give a quick overview for some of the proposed CMOS replacements. Finally, we will identify thesis layout.
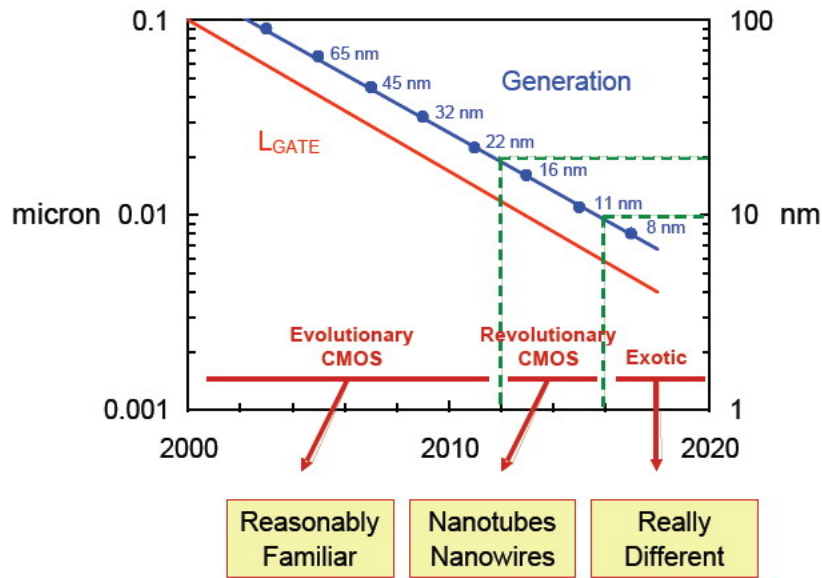
Figure 1.1: **Expected road map for CMOS technology (Source:Mark Bohr, Intel).**

1.1   Scaling CMOS challenges

The continuous scaling of the conventional transistor resulted in unwanted characteristics and caused significant degradation in its performance. In the following points, we review quickly the major scaling challenges.

- Scaling of gate oxide

  According to International Technology Roadmap for Semiconductors (ITRS) [2], scaling down the Effective Oxide Thickness (EOT) of the future devices is the most difficult challenge to improve the performance. The importance of the gate oxide thickness arises from the fact that the MOS transistor current is directly proportional to the oxide capacitance and the gate voltage ($I_D \propto C_{ox}, V_G$). Any scaling down in the dimensions should be accompanied by scaling down the operating voltage. Thus, to improve the transistor performance while scaling down the voltage, we have to increase the oxide capacitance by reducing oxide thickness. Unfortunately, the gate tunneling current increases exponentially with the decrease in oxide thickness as shown in Fig.(1.2) [3].
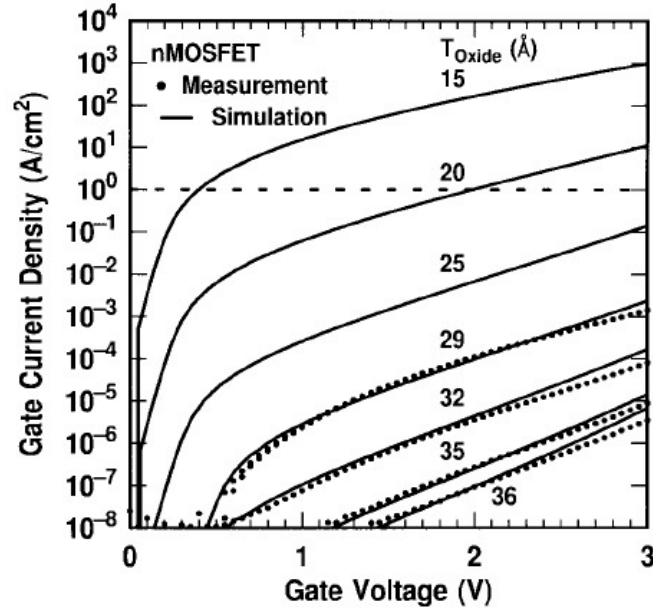
Figure 1.2: **Gate current density vs. gate voltage for various oxide thicknesses [3].**

To reduce this unwanted tunneling current, high-k dielectric materials were introduced to replace the conventional SiO_2 gate insulator. A gate dielectric with a dielectric constant (k) substantially higher than that of SiO_2 (k_{ox}) will achieve a smaller equivalent electrical thickness (t_{eq}) than the SiO_2, even with a physical thickness (t_{phys}) larger than that of the SiO_2 (t_{ox}) [4]:

$$t_{eq} = (\frac{k_{ox}}{k})t_{phys}$$

Choosing appropriate gate dielectric is not straight forward. Experiments showed that dielectrics with higher dielectric constants have narrower band gaps. This leads to higher tunneling currents. In addition, the interface between suggested dielectric materials and Si is poor and causes significant channel mobility degradation. To eliminate this side effect, an SiO_2 interfacial layer is grown between the channel and the high-k dielectric. However, this technique limits the total EOT. Theoretical study conducted by Kauerauf et. al. [5] about the optimal gate stack showed that Hf based oxides would provide the lowest leakage current even for sub 1 nm EOT.
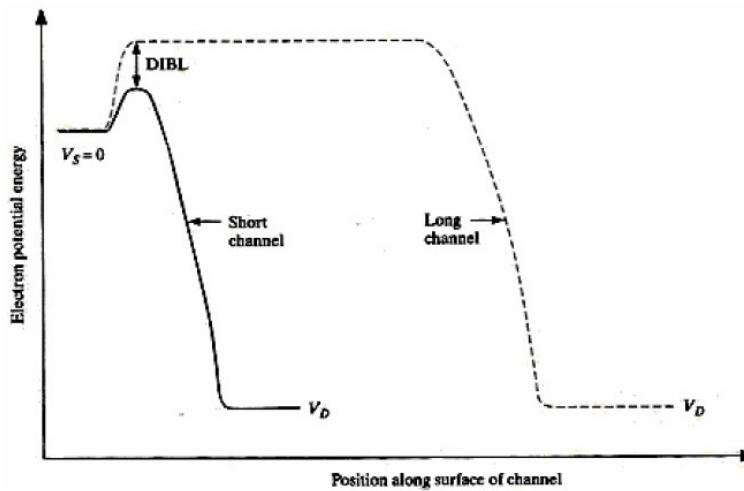
Figure 1.3: **Potential distribution of long channel and short channel MOSFETs showing the effect of DIBL [7].**

Another problem in the gate stack is the use of poly-Si gate. Gate depletion that occurs in the poly-Si contributes to the EOT by $0.3 - 0.4 \ nm$ [6] which is relatively large for thicknesses less than 2nm. Researchers suggested that the use of metal gates will eliminate this problem.

- Drain induced barrier lowering

As the transistor channel becomes shorter, the depletion region of both source and drain become closer to each other and may merge. Hence, the potential barrier at the source junction is reduced and electrons tunnel easily from source to drain. Consequently, off current increases and degrades switching characteristics of the transistor. This effect can be reduced by fabricating highly doped regions localized near the source/drain [7] to reduce source/drain depletion widths. This is known as halo implant. Localized doping is used because doping the whole channel results in channel mobility degradation.

- Channel mobility degradation

Channel mobility is very important to obtain high performance transis-

tor. Though Si is not the highest mobility semiconductor, the combination Si-SiO$_2$ was the most successful combination used in fabricating MOS structures due to the excellent interface between Si and SiO$_2$. In practical devices, the mobility of charge carriers in the channel is greatly affected by the surface roughness and the quality of the interface between the semiconductor and the oxide. To continue the scaling down of the transistor, we have to use high-k materials instead of SiO$_2$ as we stated earlier. This replacement is accompanied by considerable mobility degradation due to the poor interface between the Si and the other high-k materials. So, different trials were done to improve the mobility of the channel. One of these successful trials was strained Si in which strain to silicon lattice was introduced to improve mobility. This method has already been used in 90 nm technology processors produced by Intel. Fig(1.4) explains the fabrication of such a strained Si layer and the resulting mobility enhancements. Another way is to change the surface orientation of the channel. The standard orientation of Si wafers is (100) which achieves the highest mobility for electrons. However, it was discovered that the orientation (110) improves the hole mobility by a factor of 2.5 [6]. Thus it was suggested to use hybrid Si wafer with different crystal orientations to fabricate higher mobility transistors. Using high mobility materials in the channel instead of Si is another mobility enhancement technique. III-V compounds are among those promising materials. They have 50-100x higher mobility than Si and can be fabricated using conventional lithography and etching techniques. However, they suffer from low hole mobility and difficulty in integration with Si [8].

1.2 End of CMOS scaling

Scaling CMOS transistors to the 16 nm node may be difficult but it is possible. Sub 10 nm transistors were successfully fabricated and reported by Wakabayashi et. al. [10] (Fig.(1.5)). Beyond this point, fundamental and unavoidable limits
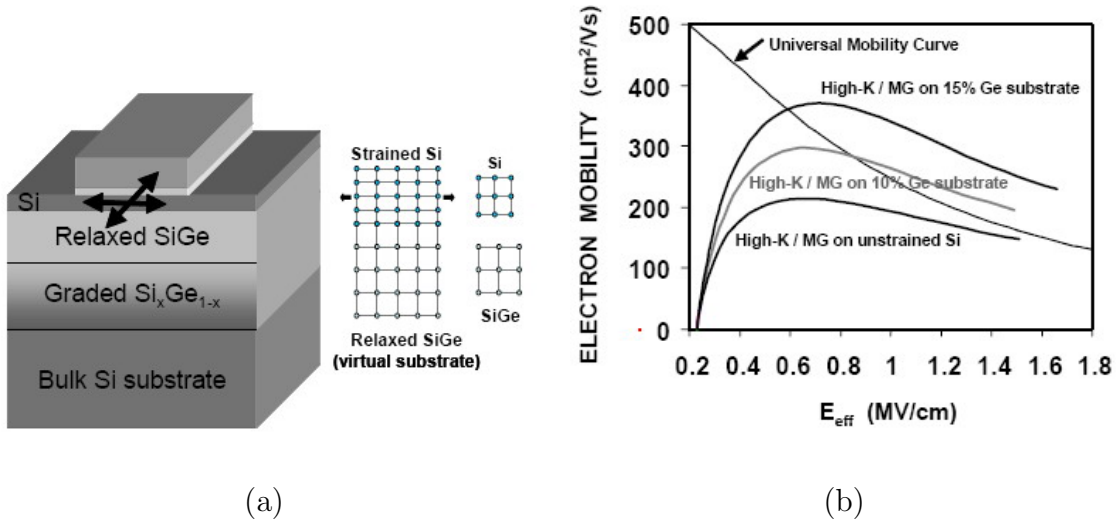
Figure 1.4: **(a)NMOS transistor with strained Si channel over relaxed SiGe layer (b) Transistor mobility for different Ge concentrations [9].**
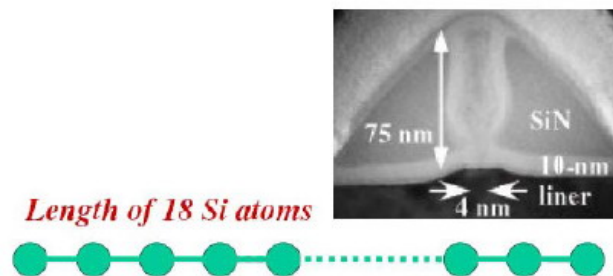
Figure 1.5: **Cross-sectional TEM view of a 5 nm gate length MOS transistor [10].**

arise. According to ITRS [2], it is expected that the physical gate length of the transistor will be around 5 nm by the year 2022 which is equivalent to 18 adjacent silicon atoms. Further scaling for the channel dimension will result in devices with completely different characteristics as we are running out of atoms.

Dissipated power density is another limiting factor. As the number of transistors per chip increases, the power dissipated per unit area increases significantly because the supply voltage in not scaled down with the same rate. This increase in power density will reach a critical limit very soon as we can see in Fig.(1.6).

Wafer patterning and fabrication is a fundamental physical and financial road-
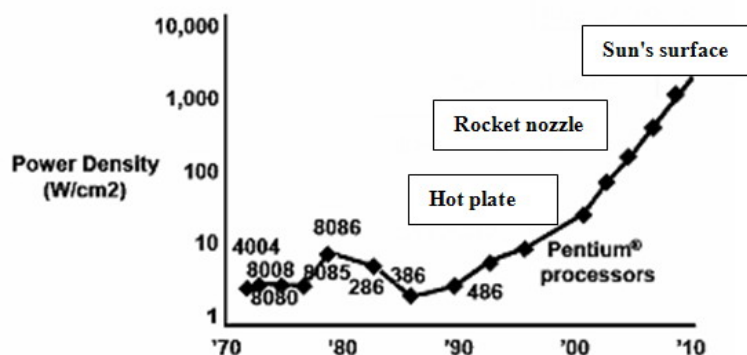
Figure 1.6: **Power density extrapolation for Intel microprocessors.**
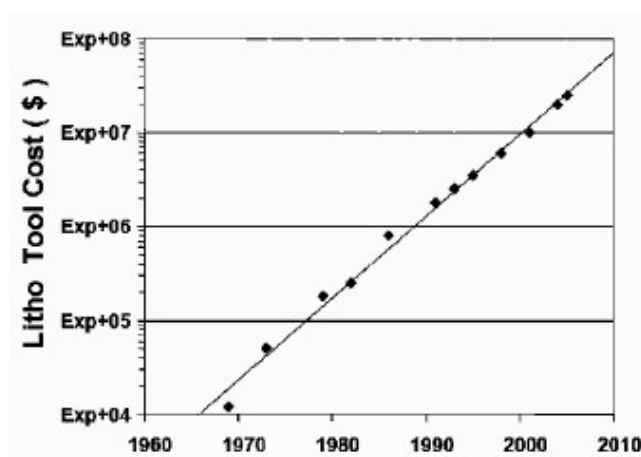
Figure 1.7: **Exponential increase in Lithography equipments cost (Source:Intel).**

block that faces scaling. Lithography techniques that will be used in future technology nodes is still not clearly defined. Besides, the cost of the equipment required to fabricate such state of the art devices is very high. Fig.(1.7) shows the exponential increase in the cost of lithography equipment.

The yield of CMOS manufacturing process becomes a critical issue. Many new materials are being used in fabrication such as high-k materials for gate oxide and low-k materials for interconnects. This introduction of new materials was accompanied by increasing number of manufacturing steps as well as more difficulties in contamination control.

To sum up, we have to find a new revolutionary technology that addresses the problems we have discussed. Such technology should be able to produce higher performance logic gates over smaller area with reduced complexity, higher yield and lower cost.

1.3   Beyond CMOS: More Moore

Continuous geometrical scaling of CMOS transistor dimensions kept the validity of Moore's law for decades. From our previous discussion, this scaling approach will end in the next few years. According to ITRS [2], we can keep the validity of Moore's law through two approaches: *Effective scaling* and *Post CMOS devices*.

The effective scaling approach aims at improving the performance and the capabilities of ICs by using innovative integration techniques such as 3D integration and/or advanced architectures such as multicore architecture. ITRS [2] expects that this approach will lead semiconductor industry in this and the next decade. This approach is beyond the scope of this study.

A real breakthrough in electronics industry will depend on Post CMOS devices. New devices will start a new era of superior ICs. Some of the suggested promising devices can be classified as CMOS extension; they use the same concept and almost the same structure of the conventional MOS transistor. The difference lies in the novel materials used to fabricate them. This category includes Carbon Nanotube (CNT) and Nanowire FETs. Integrating these new technologies to the current CMOS platform is still difficult, but it is not impossible. This is the most important issue for industry because it means that the current investments in semiconductor facilities will gain revenues even with these emerging devices.

On the other hand, non-traditional devices such as Spin transistor, Molecular transistors and many others are still far from real applications. Most of them suffer from essential problems like low gain and weak fan out capability. Thus, it is expected that we will make use of CMOS technology to design suitable interface between such futuristic devices and real world. CMOL
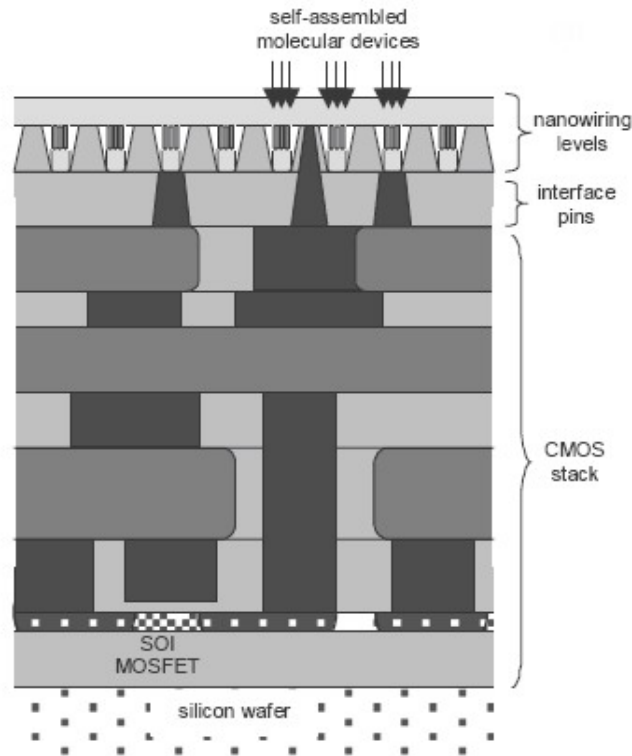
Figure 1.8: **Suggested CMOL structure [11].**

(CMOS/nanowire/MOLecular) system suggested by Likharev is an example for a hybrid electronic system [11]. The basic advantage of this system is that it will get the best from both CMOS and molecular devices. CMOS circuits are responsible for functions that require high gain and high ON currents such as I/O functions, while molecular devices take care of functions that require high density integration and low power [12]. Fig(1.8) shows an example of the CMOL structure.

Among the wide spectrum of proposed devices and materials of interest, Carbon Nanotubes (CNTs) possess a distinctive position. CNTs were first introduced in 1991 by Sumino Iijima [13]. Since then, they have attracted a lot of researchers in different fields due to their unique electrical and mechanical properties. Such activity in the field of CNTs qualified them to be the fastest growing real nanoscale

building block. Extensive studies of CNTs showed that they can be involved in wide range of applications. This encouraged us to concentrate our research on this promising material.

1.4   Thesis objectives

This thesis studies The main objective of this work is to examine the use of CNTs as both parts of electronic devices and as interconnects. Those two elements are the two basic milestones in ICs. Proper integration of both paves the way to all-Carbon ICs.

In order to evaluate the CNT transistors in digital circuits, we will develop a circuit simulation environment using Matlab. We will concentrate on coaxial SB CNTFETs to study their performance in inverter circuit.

As interconnects, we are willing to use the CNTs in a new way such that we can transmit different signals simultaneously over the same tube. First, we will study the basic physics of CNTs to investigate the role of subbands in electronic conduction. Then, we will make use of that unique band structure of CNTs to transmit several signals simultaneously over individual CNTs. Successful implementation of this technique opens the way to a new generation of electrical interconnects with higher bandwidth.

1.5   Thesis layout

Our work consists of two main parts. In the first part, we investigated the performance of CNTFETs in logic circuits. Most of recent publications regarding CNTFETs concentrates on single device characteristics and performance. This is because of the complexity of single device models and the difficulty of integrating them into circuit simulation environments. In this work, we developed a circuit simulation environment for SB CNTFET devices and used it to simulate the inverter circuit. This environment can be extended simply to other devices and for

more complex circuits. The procedure we used and the results we obtained are illustrated in chapter 3 after reviewing CNT properties in chapter 2.

In the second part of our work we tried to make use of the unique band structure for CNTs. For the first time in literature, we proved the possibility of multimode transport through CNTs. This means that individual CNTs can carry multiple signals simultaneously like optical fiber. This concept will open new opportunities and applications for CNTs. Our effort regarding this topic is discussed in chapter 4 and chapter 5.

Finally, we have addressed some open questions that still need further studies in chapter 6.

Chapter 2

CNTs Structure and Properties

Properties of carbonic materials are determined by the order of carbon atoms within the crystal structure. For example, both diamond and graphite consist of pure carbon atoms, however they have contradicting physical properties. Diamond is transparent, hard and has low electrical conductivity, whereas, graphite is opaque, soft and is considered a good conductor.

Carbon nanotubes are a recently discovered carbonic material with very interesting properties. They consist of pure carbon atoms with very special arrangement. Such arrangement is responsible for their unique properties. In this chapter, we will review briefly the physics of CNTs, their properties and their applications.

2.1   Hybridization of carbon atom orbitals

In general, hybridization of atomic orbitals is the process in which two or more orbitals in an atom mix together and produce a new set of hybridized orbitals. The electronic structure of carbon atoms allows for different configurations for orbital hybridization. That is why we find various bonding configurations in carbon compounds.

A carbon atom contains 6 electrons. Two of them are tightly bound and
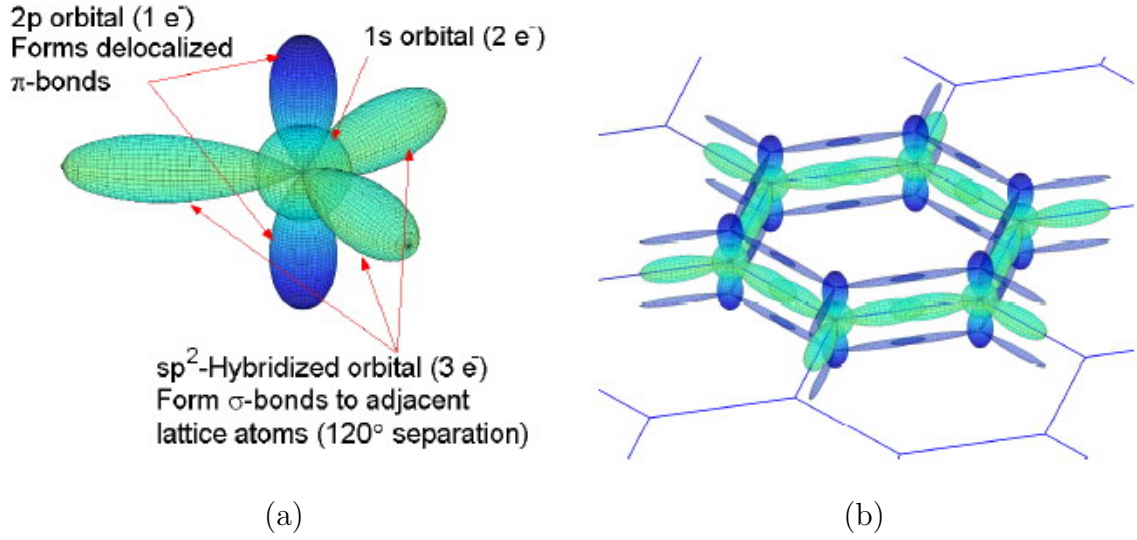
Figure 2.1: **(a)**sp^2 **hybridization of a carbon atom (b) Hexagonal lattice of graphene**

occupy $1s^2$ orbital. The remaining 4 atoms are weakly bound and occupy $2s^2$ and $2p^2$ orbitals. These electrons are called valence electrons and produce 4 orbitals $2s$, $2p_x$, $2p_y$, $2p_z$ in crystalline phase. There are three possible hybridizations for carbon atoms: sp, sp^2 and sp^3. We are interested only in sp^2 hybridization which occurs in CNTs.

2.1.1 sp^2 **hybridization**

In this hybridization type, $2s$ orbital mixes with two $2p$ orbitals producing three hybridized orbitals in x–y plane (we assume hybridization between $2s$, $2p_x$, $2p_y$) separated by 120° angle. The remaining orbital ($2p_z$ orbital)will be perpendicular to x–y plane as shown in Fig.(2.1) . Each atom will be connected to three nearest neighbor atoms through strong σ bonds. This bonding configuration is responsible for the hexagonal shape of graphene sheets (Fig.(2.1)). This hexagonal structure is the core structure of graphite and CNTs. The three electrons involved in the three σ bonds are tightly bounded and do not contribute in electronic conduction. In contrast, the remaining electron involved in π bond is weakly coupled and is responsible for electrical properties of the material.
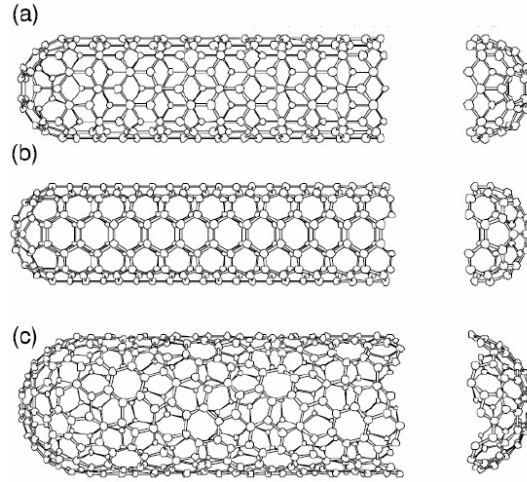
Figure 2.2: **Carbon Nanotubes classification: (a) zigzag, (b) armchair, and (c) chiral nanotubes**

2.2   Carbon Nanotube structure

Carbon nanotubes can be considered as a graphene sheet rolled to form a cylindrical shape. The diameter of a Single Wall Carbon Nanotube (SWCNT) varies from fractions of nanometers to several nanometers. Theoretically, the smallest possible diameter of a CNT is 0.3 nm [14]. CNTs with diameters $\approx$ 0.3 nm were fabricated and reported by Zhao et.al. [15]. Though there are no physical constraints on the CNT length, the longest nanotube that was ever reported was 4 cm in length [16]. The real parameter that limits the length of fabricated CNTs today is the available fabrication facilities. SWCNTs are classified according to the shape of their cross section into three families: (a) zigzag, (b) armchair, and (c) chiral nanotubes as shown in Fig.(2.2).

The structure of CNTs is defined by two basic vectors: *Chiral vector* $\vec{C_h}$ and *Translational vector* $\vec{T}$. The values of these vectors determine the type of the CNT and its geometrical properties.
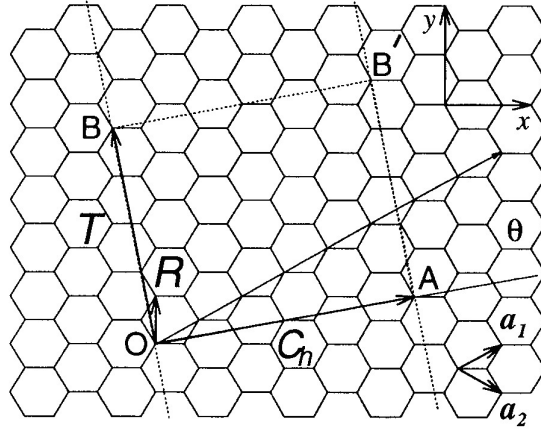
Figure 2.3: **Unrolled graphene sheet. Nanotube is constructed when the points** O **and** A **, and** B **and** B' **are connected together. Vectors** $\vec{OA}$ **and** $\vec{OB}$ **define chirality vector** $\vec{C_h}$ **and translational vector** $\vec{T}$ **respectively. The rectangle** $OAB'B$ **defines the nanotube unit cell [17].**

2.2.1 Chiral vector $\vec{C_h}$

Chiral vector defines the two points on a graphene sheet that coincide when that sheet is rolled to form a CNT. This can be understood from Fig.(2.3), where a CNT is constructed by rolling the sheet such that the two points O and A coincide. The vector $\vec{OA}$ defines the chiral vector which can be expressed in terms of the primitive vectors of the honeycomb lattice $\vec{a_1}$ and $\vec{a_2}$ as follows:

$$\vec{C_h} = n\vec{a_1} + m\vec{a_2} \equiv (n, m) \tag{2.1}$$

The values of the integers n and m specify the type of a CNT. When $\vec{C_h} = (n, n)$ that is $n = m$, it corresponds to an armchair nanotube and when $\vec{C_h} = (n, 0)$, it corresponds to a zigzag nanotube. Other values for (n, m) correspond to a chiral nanotube.

The circumference of a CNT (L) is the magnitude of the chiral vector $\vec{C_h}$ and is given by:

$$L = \left| \vec{C_h} \right| = \sqrt{\vec{C_h} . \vec{C_h}} = \sqrt{3} a_{c-c} \sqrt{n^2 + m^2 + nm} \tag{2.2}$$

and the diameter of the nanotube (d) will be:

$$d = L/\pi = \frac{\sqrt{3}a_{c-c}}{\pi}\sqrt{n^2 + m^2 + nm} \tag{2.3}$$

where a_{c-c} is carbon–carbon bond length and equals 1.42 A^o.

2.2.2   Translational vector $\vec{T}$

As depicted in Fig.(2.3), the intersection of the vector $\vec{OB}$ (normal to $\vec{C_h}$) with the first lattice point defines the translational vector $\vec{T}$ [18]. The two vectors $\vec{C_h}$ and $\vec{T}$ define the rectangle $OAB'B$ which specify the unit cell of the CNT with chirality vector $\vec{C_h}$. Note that CNT unit cell is different from the unit cell of the graphene sheet defined by the primitive vectors $\vec{a_1}$ and $\vec{a_2}$. The primitive vectors of the CNT unit cell are the vectors $\vec{C_h}$ and $\vec{T}$.

To determine the number of hexagons in the unit cell of a CNT, we use the following relation:

$$N = \frac{Area\,of\,CNT\,unit\,cell}{Area\,of\,the\,Hexagonal\,lattice\,unit\,cell} = \frac{\left|\vec{C_h} \times \vec{T}\right|}{|\vec{a_1} \times \vec{a_2}|} \tag{2.4}$$

2.3   Electronic properties of Carbon Nanotubes

2.3.1   Basic Concepts

- Tight Binding approximation

  When isolated atoms are brought together in a crystal structure, the energy levels of these atoms split to form the energy bands observed in solids. This splitting is a result of the interaction between wavefunctions of adjacent atoms. Outer electrons are the most affected electrons by this overlap between the wavefunctions. In tight binding approximation, we assume that

the electrons remain localized about the atomic core. Thus, there is slight overlap between the wavefunctions of the nearest neighbor atoms only.

- Hamiltonian Matrix

To get the band structure for any particular crystal or molecule, we have first to obtain the Hamiltonian matrix of that particular structure. The eigenvalues of the Hamiltonian matrix represent the band structure of the targeted material. A general procedure was developed by Datta [19] to obtain such matrix for infinite periodic structures. The main advantage of dealing with periodic structures is that we can start from any point and we are sure that the conditions at this starting lattice point are the same as those in other lattice points.

- Ballistic transport

According to Ohm's law, the conductance of any conventional bulk conductor increases as the length of the conductor decreases. Hence, the conductance may approach infinity for nanoscale conductors. This is not true. For nanoscale conductors, there is an upper limit for the conductance known as the quantum conductance and given by:

$$G = \frac{M}{R_Q} = M\frac{e^2}{h} \tag{2.5}$$

where $R_Q \approx 26k\Omega$ is the quantum resistance and M is the number of conducting modes.

The resistance R_Q is the minimum resistance of any ballistic conductor with perfect contacts where electrons travel between the two contacts without any scattering. This resistance arises at the interface between bulk contacts and $1D$ conductors. In bulk contacts, electron transport occurs through infinite number of modes, while in $1D$ conductors there are finite number of

(a)   (b)
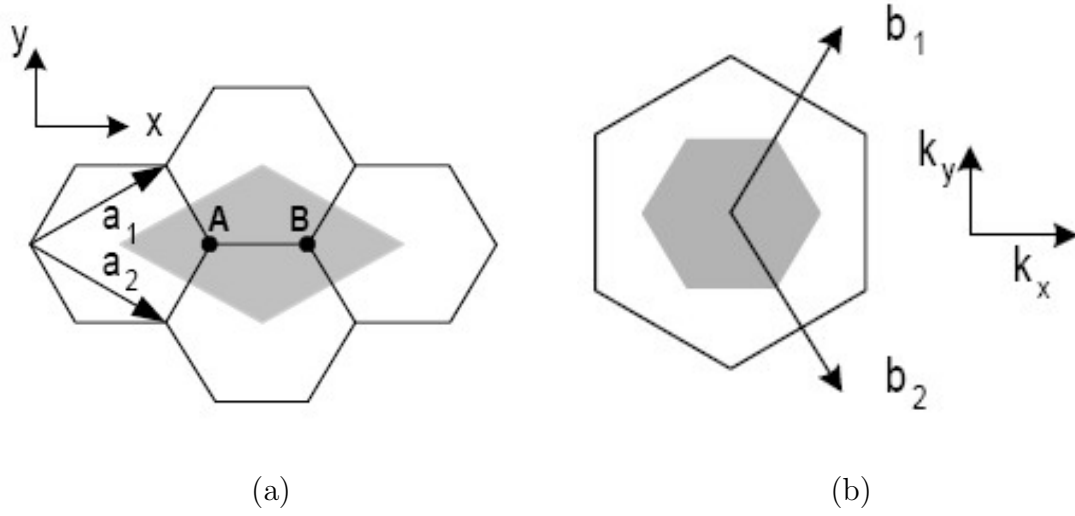
Figure 2.4: **(a)Graphene sheet in real space. The unit cell contains only two atoms A and B and is defined by the gray area (b) Reciprocal lattice of graphene sheet. The first Brillioun zone is defined by the gray hexagon.**

modes (subbands) that can be used in electron transport. This mismatch between the two conductors explains the quantum resistance.

2.3.2 Dispersion relation of CNTs

As we have stated earlier, CNTs stem from $2D$ graphene sheets. Thus, the dispersion relation of CNTs is usually extracted from that of $2D$ graphene sheets [17, 19]. The unit cell of the hexagonal lattice of the graphene sheet consists of two adjacent atoms as shown in Fig.(2.4). The primitive vectors $\vec{a_1}$ and $\vec{a_2}$ are given by:

$$\vec{a_1} = a_0(\frac{\sqrt{3}}{2}\hat{x} + \frac{1}{2}\hat{y}) \qquad (2.6)$$

$$\vec{a_2} = a_0(\frac{\sqrt{3}}{2}\hat{x} - \frac{1}{2}\hat{y}) \qquad (2.7)$$

where $a_0 = \sqrt{3}a_{c-c}$ is the length of the primitive vector.

To deduce the reciprocal lattice primitive vectors $\vec{b_1}$ and $\vec{b_2}$, we make use of their relation with primitive vectors of real space lattice: $\vec{a_i} \cdot \vec{b_j} = 2\pi\delta_{ij}$ which gives the following result:

$$\vec{b_1} = b_0(\frac{1}{2}\hat{x} + \frac{\sqrt{3}}{2}\hat{y}) \tag{2.8}$$

$$\vec{b_2} = b_0(\frac{1}{2}\hat{x} - \frac{\sqrt{3}}{2}\hat{y}) \tag{2.9}$$

where $b_0 = \frac{4\pi}{\sqrt{3}a_0}$ is the length of the basis vector in reciprocal space.

The next step is to obtain the dispersion relation of the specified unit cell using tight binding model where nearest neighbor interaction will be considered only. As we have discussed in Sec.(2.1.1), the hybridization of carbon atoms in graphene is sp^2, where we have three σ covalent bonds and only one π covalent bond formed by $2p_z$ orbital. It is sufficient to include $2p_z$ orbital in calculations because π energy bands are the most important in determining the electronic properties of graphene. Following these facts, the wave vector dependent Hamiltonain of one unit cell is given by [20]:

$$H(\vec{k}) = t \begin{bmatrix} 0 & 1 + e^{i\vec{k}\cdot\vec{a_1}} + e^{i\vec{k}\cdot\vec{a_2}} + e^{i\vec{k}\cdot\vec{a_3}} \\ 1 + e^{-i\vec{k}\cdot\vec{a_1}} + e^{-i\vec{k}\cdot\vec{a_2}} + e^{-i\vec{k}\cdot\vec{a_3}} & 0 \end{bmatrix} \tag{2.10}$$

where $\vec{a_3} = \vec{a_1} - \vec{a_2}$ and $t \approx -3eV$ is the $2p_z$ orbital coupling parameter.

Solving for eigen values of the given Hamiltonian matrix, we obtain the dispersion relation of $2D$ graphene:

$$E(\vec{k}) = \pm |t| \cdot \sqrt{1 + 2cos(\vec{k} \cdot \vec{a_1}) + 2cos(\vec{k} \cdot \vec{a_2}) + 2cos(\vec{k} \cdot \vec{a_3})} \tag{2.11}$$

The positive sign in equation(2.11) refers to conduction band while the negative sign refers to the valence band. Thus graphene has a symmetric band structure for both electrons and holes. This dispersion relation is plotted in Fig.(2.5).
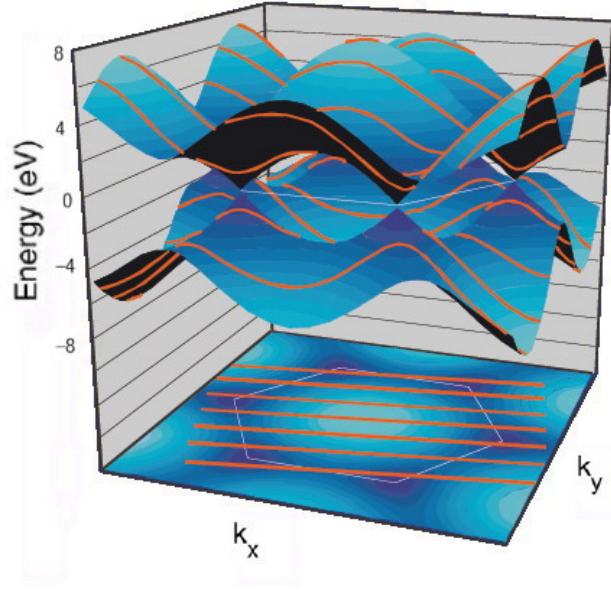
Figure 2.5: **Band structure of graphene.   Notice the vanishing of band gap at the corners of hexagonal Brillouin zone.   Cuts of the graphene bands indicated by the orange lines are the allowed states in CNTs.   If the cut passes through a corner of Brillouin zone (Fermi point), the CNT is metallic; otherwise, the CNT is semiconducting [21].**

We notice that the band gap vanishes at the corners of the Brillouin zone which are called Fermi points and have the wave vector $\vec{k_F}$:

$$\vec{k_F} = (u \pm \frac{1}{3})\vec{b_1} + (v \mp \frac{1}{3})\vec{b_2} \qquad (2.12)$$

where u and v are integers.

Now, to extract the dispersion relation of a CNT, we should make use of the periodic boundary conditions of the transition along the chirality vector. It is well known from Bloch theorem that any translational operation along the primitive vectors of unit cells (say the chirality vector $\vec{C_h}$ in case of CNTs) must satisfy the following condition:

$$R_{\vec{C_h}}\Psi = e^{i\vec{k}\cdot\vec{C_h}}\Psi \qquad (2.13)$$

where $R_{\vec{C}_h}$ is any translational operation in the circumferential direction. But in CNTs, wavefunctions must be periodic along the circumference such that $e^{i\vec{k}\cdot\vec{C}_h}\Psi = \Psi$. This periodicity restricts the values of the electrons' momentum to those values satisfying the following condition:

$$\vec{k}\cdot\vec{C}_h = 2\pi\nu \tag{2.14}$$

where ν is an integer.

As a result, each band of graphene splits into a number of $1D$ subbands labeled by ν. The allowed energy states of the tube are cuts of the graphene band structure. When these cuts pass through a Fermi point, the tube is metallic. In cases where no cut passes through a Fermi point, the tubes are semiconducting [21]. Thus, CNT will have zero bandgap only when $\vec{k_F}$ satisfies equation(2.14). Mathematically, this means that whenever $n - m = 3q$, where q is an integer, the CNT will be metallic. However, it was shown theoretically [22] and experimentally [23] that this is not completely correct. An (n, m) CNT is truly metallic only when $n = m$ (armchair CNT). While it has very small bandgap (quasimetallic) when $n - m = 3q$ and $q \neq 0$. In this case, the bandgap magnitude depends inversely on the square of the CNT radius. CNT is truly semiconductor only when $n - m \neq 3q$. This deviation is a result of the finite curvature of the graphene sheet forming the CNT. Finally, the bandgap of the qth mode of a zigzag CNT was found to be [24]:

$$E_g = 2\left|t\right|\left\{1 + cos(\frac{\pi q}{n})\right\} \tag{2.15}$$

2.3.3 Charge carrier transport in Carbon Nanotubes

Several studies were conducted to understand the nature of electronic transport through CNTs. In an ideal case, CNT is a ballistic conductor. In a metallic CNT, four channels contribute to conduction due to subband degeneracy and
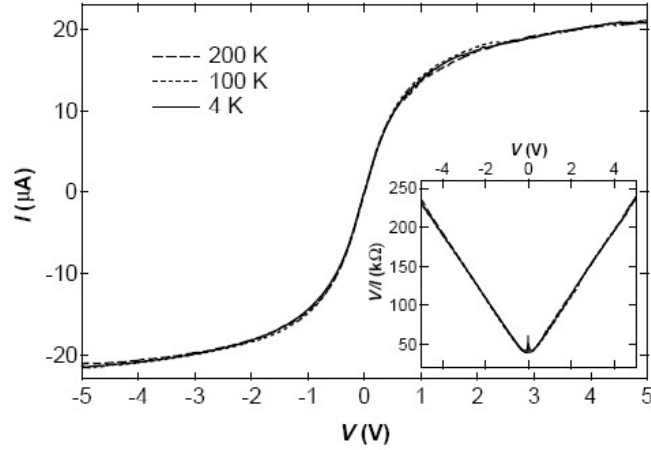
Figure 2.6: **I–V characteristics of** $1\mu m$ **metallic CNT with low resistance contact measured at different temperatures as reported in [25]. The inset show the increase in CNT resistance** $R = V/I$ **with increasing biasing voltage.**

spin degeneracy. Thus, the quantum conductance of a metallic nanotube is $G = 4 \times e^2/h$ which corresponds to quantum resistance $R_Q = 6.5\ K\Omega$.

Zhen Yao and co-workers [25] measured the I–V characteristics of a 1 μm metallic CNT (Fig.(2.6)). Results showed that current saturates at 25 μA which corresponds to current density up to $10^9\ A/cm^2$. The observed degradation in conductivity with increasing biasing was explained by the increasing rate of optical phonon scattering. Later, Park et al. [26] estimated experimentally the mean free paths of electrons in CNTs in both high biasing and low biasing regimes. At low biasing ($\leq 0.1\ V$), scattering is dominated by acoustic phonons with mean free path $l_{ac} \approx 1.6\ \mu m$, whereas, at high biasing, scattering is dominated by optical phonons with mean free path $l_{opt} \approx 10\ nm$. Similar study conducted by Javey et al. [27] using CNTFET structure estimated mean free paths for acoustic and optical phonons to be 300 nm and 15 nm respectively. It also showed that very short CNTs ($\approx 10\ nm$) work as ballistic conductor with significant high current carrying capacity (up to 70 μA) (Fig.(2.7)). Recently, Sundqvist and co-workers [28] studied the variation of CNT resistance with both biasing voltage and length of CNT. The results of this study is summarized in Fig.(2.8)). As
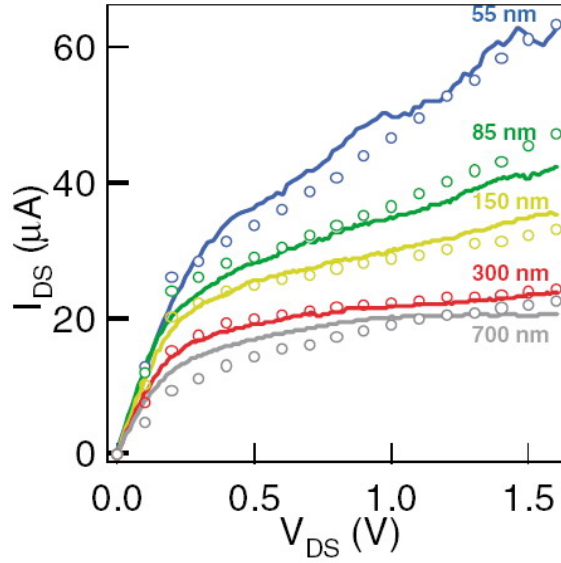
Figure 2.7: **I–V characteristics at different lengths of CNTFET devices [27].**

depicted in the figure, when nondefective CNTs operate in low biasing regime, resistance shows linear dependence on the length and it is controlled by the mean free path of acoustic phonons. At high biasing regime, short nanotubes resistance shows also linear dependence on length and the resistance is mainly controlled by optical phonons scattering mean free paths. We notice that the resistance of CNT saturates at lengths about 1 μm and then degrades and merge with the acoustic branch for very long nanotubes. The reason of this behavior is that in long CNTs, electrons need to be accelerated by the electric field for longer distance to get enough energy to excite optical phonons. Then when this distance becomes larger than l_{ac}, acoustic phonons scattering becomes the dominant scattering mechanism.

2.3.4 Luttinger Liquid: Electrons in $1D$

Systems of interacting electrons in $3D$ and $2D$ can be modeled using Fermi liquid model. In Fermi liquid, interacting electrons are represented by a set of noninteracting quasiparticles eigenstates. In $1D$ systems, Fermi liquid fails in describing
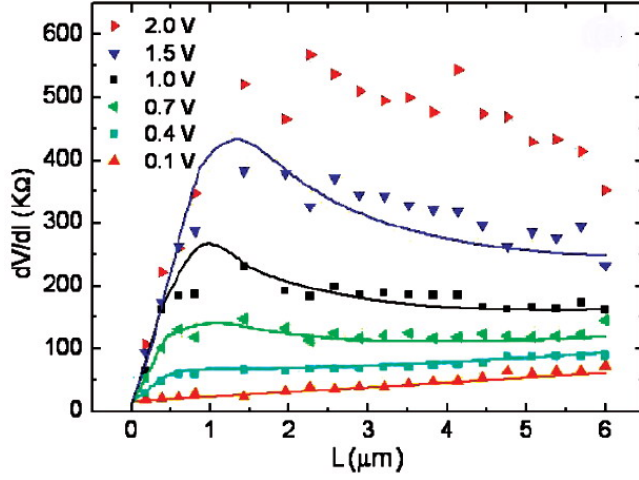
Figure 2.8: **The differential resistance of CNT vs CNT length at different voltages [28]**

interacting electrons. This problem was first resolved in 1950 by Sin-itiro Tomonaga [29] in his pioneering work: "Remarks on Bloch's Method of Sound Waves applied to Many-Fermion Problems". Tomonaga model was modified latter by Luttinger [30] and it was known as Luttinger liquid (LL) model. The eigenstates of a LL are defined by sound like charge density waves and spin density waves. Both wave types propagate independently with different velocities. This is known as spin-charge separation. Creation of an electron in a LL is equivalent to exciting an infinite number of these density waves. Also, a LL is known to have a tunneling density of states that is suppressed as a power-low function of energy ($\rho(E) \propto |E|^{\alpha}$). The exponent α is determined by the so-called Luttinger parameter g which represent the amount of interaction in a LL such that: for non-interacting electrons $g = 1$, while it is ≤ 1 for interacting electrons. More details can be found in [31, 32].

Since CNTs are considered $1D$ conductors, they obey the LL model [18]. The LL behavior of CNTs was verified experimentally by Bockrath and co-workers [33] by observing the tunneling conductance of a junction between a CNT and a bulk contact. As predicted from theory, the conductance showed power-law voltage

dependence. The same behavior was also measured by Yao et al. [34] but through a junction between two metallic nanotubes. The pentagon-heptagon defect between the two tubes acts as a tunnel barrier between two LLs.

2.4 Applications of CNTs

The extraordinary properties of CNTs qualified them to be the backbone of a wide spectrum of applications. In this section we will scan some of CNTs applications.

- CNT based transistors

  In CNTs, electrons are confined in the circumferential direction and are free to move only in forward or backward directions. This nature greatly improves the charge carrier mobility through CNTs over other materials such as Si. Thus, CNTs are one of the most promising candidates to replace Si channel in conventional MOS transistors. It was reported that the effective mobility of CNTFETs is 20 times higher than that of planar Si MOSFETs with 10 nm channel length [35]. Besides, the atomic structure of CNTs is formed such that all chemical bonds are satisfied. So, high-k dielectrics can be used with CNT based transistors without interface problems that causes severe mobility degradation when used with Si MOSFET.

  Also, the band structure of CNTs is identical to the two types of charge carriers (electrons and holes). Hence, we can fabricate p-type and n-type identical transistors with identical sizes. This was not possible in Si MOSFETs because of the significant difference between electrons mobility and holes mobility. Designers tend to use larger p-type transistors to compensate this mobility difference.

- CNT Field Effect Emission displays

  The idea of using CNTs as nano electron guns was first demonstrated in 1995 by Rinzler and co-workers [36]. This study opened the way to use nanotubes in Field Effect displays. A nanotube Field effect display uses
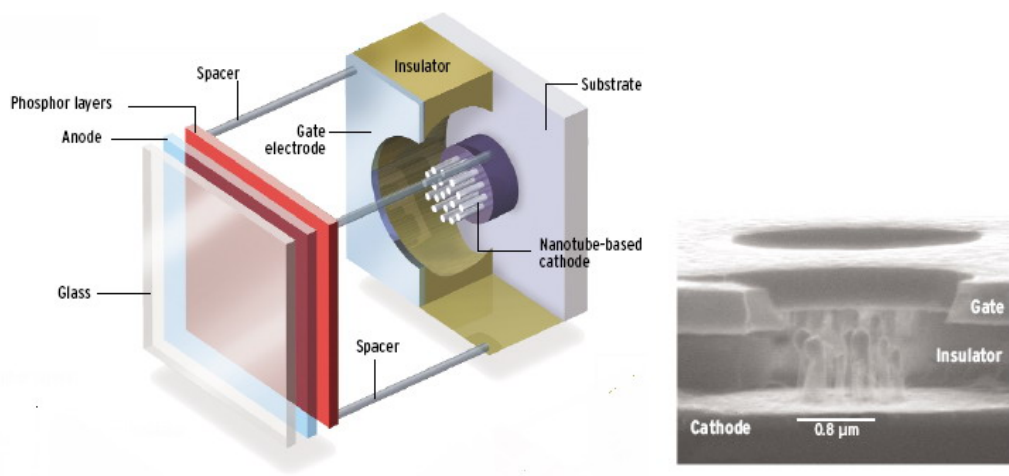
Figure 2.9: **A pixel of nanotube Field Effect display [37]**

bundles of nanotubes as electron emitters. Electrons produced from nanotubes are swept to hit a phosphorus layer to emit visible light (Fig.(2.9)). This is the same idea of normal CRTs, but with significant reduction in its size and weight. Nanotube Field Effect displays will also have advantages over LCD and Plasma displays as they will offer wider viewing angles and less power consumption [37].

• CNT Interconnects

As we have discussed in a previous section, Carbon atoms are bound together through strong σ bonds to form CNTs. These strong bonds are responsible for the immunity of CNTs to electromigration observed in other materials used in interconnects such as Cu. A study of multiwalled CNTs reliability [38] showed that they can conduct high current density ($\geq 10^9 A/cm^2$) at temperatures up to 250^0C and for time intervals up to two weeks without any failure or change in its resistance. Actually, this is a very high current carrying capacity compared to that of Cu which reaches $10^6 A/cm^2$.

The major limiting factor in the performance of CNTs interconnects is the contact resistance. In ideal cases, the contact resistance will be 6.5 $K\Omega$. To overcome this high resistance, dense bundles of CNTs are used as inter-
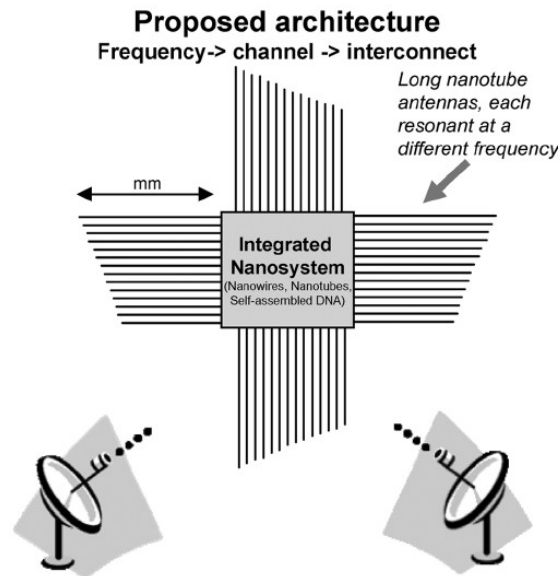
Figure 2.10: **Wireless communication between nanosystems and macroscopic world** [**41**]

connects. The dimensions of these bundles are similar to Cu interconnects dimensions. Different groups tried to investigate the behavior of CNTs interconnects and model them.

- Antennas

  One of the greatest challenges facing emerging nanoscale systems is their interface with larger surrounding systems. One of the suggested solutions is to use nano antennas to connect different systems together (Fig.(2.10)). The size and the characteristics of CNTs qualify them to be ideal choice for such nano antennas. Radiation properties of these antennas were considered in several studies, but they are still in the phase of theoretical study [39, 40].

Chapter 3

CNT Transistors and Circuits

Recently developed device models depend on iterative methods with extensive calculations to solve complex quantum mechanical equations. Integration of such models into circuit simulators like SPICE is not possible. Hence, the performance of CNT devices in digital circuits is still unpredictable. In this study, we developed a Matlab environment that is able to simulate CNTFET digital circuits.

This chapter starts with a quick review for different CNTFET structures. In our study, we concentrated on Schottky Barrier CNTFET (SB CNTFET). We first describe the model we used to simulate individual SB CNTFETs, then, we discuss our circuit simulation strategy in details. Finally, we introduce the results of the inverter circuit static and dynamic behavior [42].

3.1 CNTFET Structures and characteristics

The first fabricated CNTFET was reported in 1998 when Tans et al. [43] fabricated the first operating FET using SWCNT. As shown in Fig.(3.1), the transistor used a semiconducting Si wafer as a back gate covered with 300 nm SiO_2 over which a SWCNT was laid. The characteristics of this transistor showed that it works like p-type transistor. Tans et al. related this behavior to the contact between the CNT and the platinum (Pt) as we will illustrate later. This
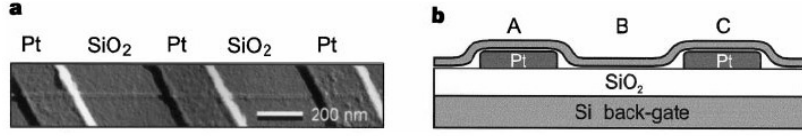
Figure 3.1: **(a)AFM image of the first fabricated CNTFET. (b) Schematic cross section of the device [43].**

early prototype of CNTFET encountered a lot of modifications to improve its characteristics to replace traditional Si CMOS transistors.

Proposed CNTFETs may have planar gate or coaxial gate. It was proved that the optimum gate structure of Si MOSFET is wrap-around gate [44] where the gate wraps around a beam of silicon. However, fabricating this structure in Si MOSFETs is not a simple task. In contrast, the cylindrical shape of CNTs makes the coaxial structure of CNTFETs the most convenient structure and the most suitable one for future $3D$ integration. Guo et al. [45] studied the electrostatics of Metal-Oxide-Semiconductor CNT structures and showed that the planar geometry had comparable performance to Si MOS structure, while the coaxial CNT structure promises significantly higher performance.

Away from the geometry of the CNTFET, CNTFETs can be classified into three major types:1) Schottky Barrier(SB) CNTFET, 2)MOS CNTFET, and 3)Band-to-Band Tunneling (BTBT) CNTFET.

3.1.1   Schottky Barrier(SB) CNTFET

In this type of CNTFETs, a semiconducting CNT channel is connected directly to metallic source and drain contacts. As in ordinary contacts between semiconductors and metals, a Schottky barrier is formed at the interface. Charge carriers transport from the contacts to the channel by quantum mechanical tunneling through the barriers. The tunneling rate of charge carriers, hence the transistor current, is controlled by the gate by changing the thickness of the SB. This way of operation is different from the conventional transistors where the current
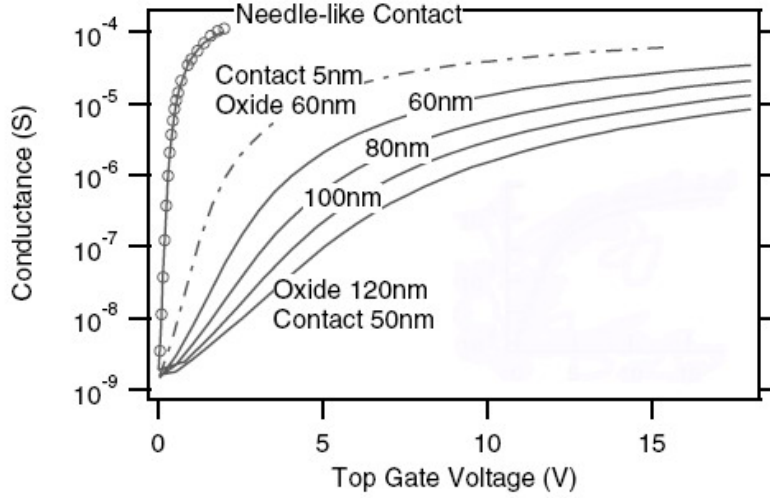
Figure 3.2: **The effect of oxide thickness and contact geometry on the SB CNTFET characteristics. The best transistor performance obtained for coaxial gate with needle contact [46].**

switching is accomplished by modifying the channel conductance not the contact resistance. Thus the operation of the transistor is basically controlled by the electric field near the contact. Hence, transistor characteristics are affected by both the oxide thickness and the geometry of the metallic contact as proved by Heinze et al. [46]. The influence of the oxide thickness and contact geometry on the transistor characteristics is shown in Fig.(3.2). As depicted in the figure, thinner oxides enhance the switching of the transistor. The same study showed that the ideal structure of this transistor type is the wraparound cylindrical gate with needle like metallic contact. Such contact can be fabricated using a nanowire or a metallic CNT. The later choice would be better as it allows us to have a complete CNT electronics and pave the road toward $3D$ integration.

The height of the SB is also an important factor in controlling the transistor performance. This barrier height is specified by the position of the Fermi level of the metallic contact with respect to the valence band (in case of holes tunneling) or the conduction band (in case of electrons tunneling). When the Fermi level of the metallic contact is located along the center of the CNT band gap, identical
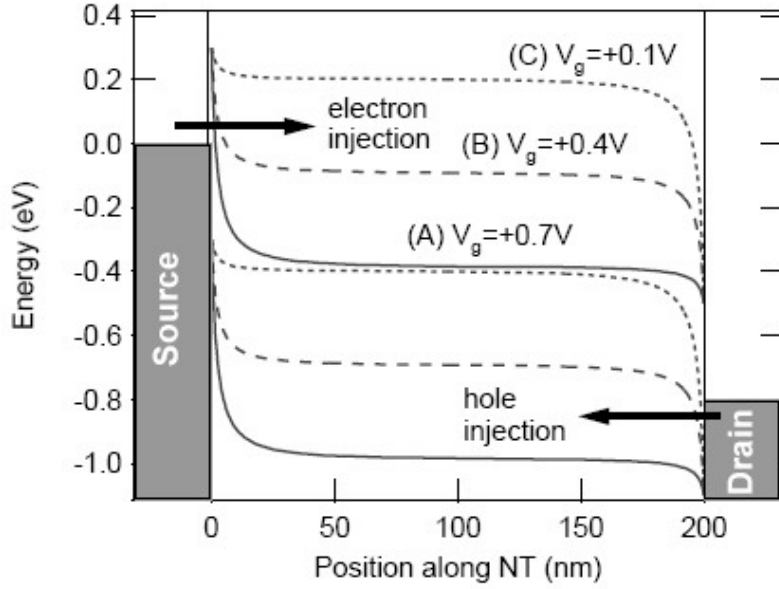
Figure 3.3: **Band diagram of the mid-gap SB CNTFET at $V_D = 0.8V$ and $V_G = 0.1V$, $V_G = 0.4V$ and $V_G = 0.7V$ [47].**

barriers for both electrons and holes is formed and symmetric transistor characteristics is obtained. The symmetric behavior of a mid-gap SB CNTFET with planar structure was verified experimentally and theoretically [47]. The band diagram of the transistor is shown in Fig.(3.3). This band diagram illustrates the I–V characteristics shown in Fig.(3.4) at the three indicated points A, B and C. At biasing point A, the barrier facing electrons injected from the source is very thin, while a thick barrier faces holes injected from the drain. Thus the transistor is ON and the current is dominated by the electrons. This picture is reversed at biasing point C where the transistor is ON but the major contribution of the current comes from the holes. Minimum current of this transistor type is reached only when $V_G = V_D/2$ when a relatively thick barrier faces both electrons and holes.

When the Fermi level of the metallic contact is shifted from the center of the CNT band gap, asymmetric transistor characteristic is produced and its ambipolar behavior is reduced (Fig.(3.5)) [46]. The position of the Fermi level with
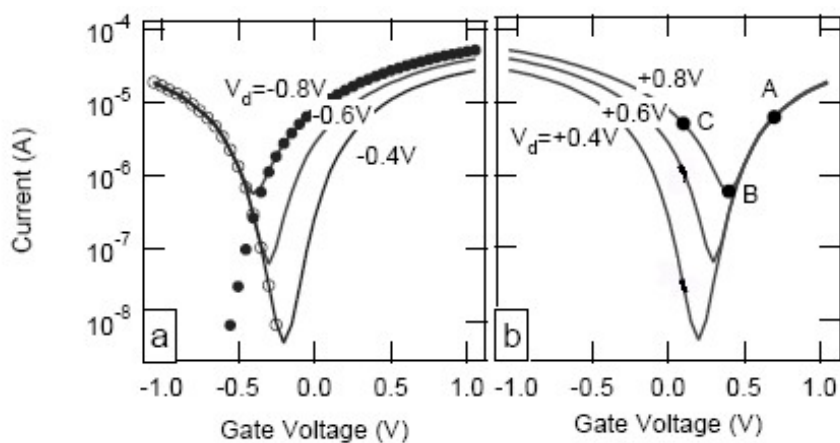
Figure 3.4: **I–V characteristics of the mid-gap SB CNTFET. The difference between a and b is the sign of the drain voltage [47].**
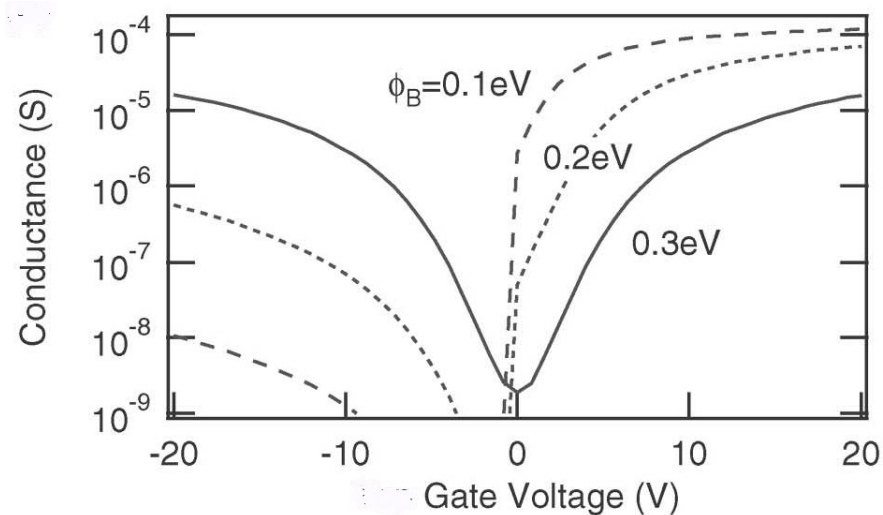
Figure 3.5: **conductance versus gate voltage at different heights of SB. The shown heights refers to electron barrier. The same results will be obtained for holes but the opposite sign of the gate voltage [46].**

respect to the channel band gap is essentially determined by the work function of the metal S/D. This was verified experimentally by Chen et al. [48] where three different metals (namely Al, Ti and Pd) were used as S/D with various CNT diameters (Fig.(3.6)). Changing the nanotube diameter modifies its band gap ($E_g \propto 1/d$). Hence, the barrier height decreases as the nanotube diameter increases (Fig.(3.6)).

3.1.2 Other CNTFET structures

MOS CNTFETs are much similar to conventional Si MOSFETS. The source and drain of these devices are p-doped or n-doped CNT. Recently reported CNTFETs used chemical doping using Potassium (K) atoms to produce n-doped S/D [49] and electrostatic doping using backgate for p-doped S/D [50]. The band diagram and corresponding I–V characteristics of electrostaically doped p-type transistor is shown in Fig.(3.7). This figure illustrates the operation of the transistor at three different voltage points: I_{ON}, I_{min} and $I_{n-channel}$. As depicted in the figure, the top gate modifies the barrier height below the gate which is similar to the ordinary MOSFETs.

Band-to-Band Tunneling (BTBT) CNTFETs is another transistor type that uses different doping for Source and Drain for the same transistor. This structure was first introduced by Appenzeller et al. [51]. The major contribution of this p-i-n structure is that it had sub 60 mV/dec subthreshold swing. Unfortunately, the ON current of this transistor is significantly small compared to other CNTFETs. Thus these transistors are suitable for low power applications, but will not be effecient for high performance applications.
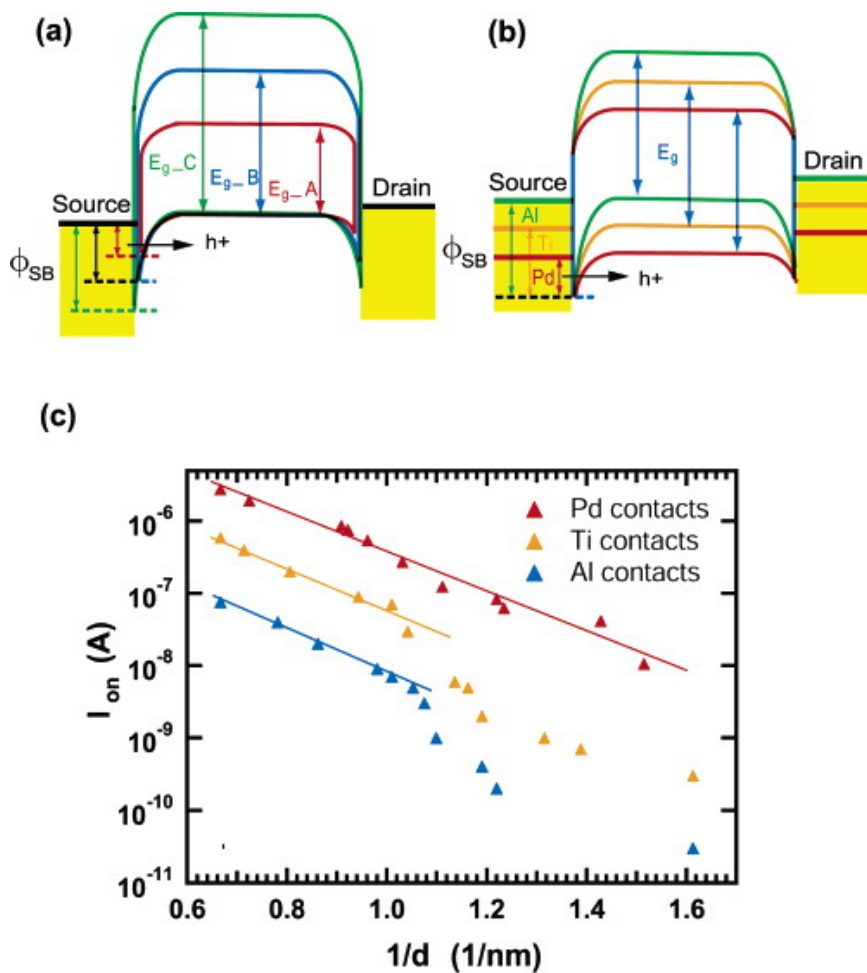
Figure 3.6: **(a)Band diagram shows the effect of changing the CNT diameter on the SB height. (b) Band diagram shows the barrier height for three different metallic contacts (Al, Ti and Pd). (c) Change of the transistor ON current with the CNT diameter for the three different metallic contacts [48].**
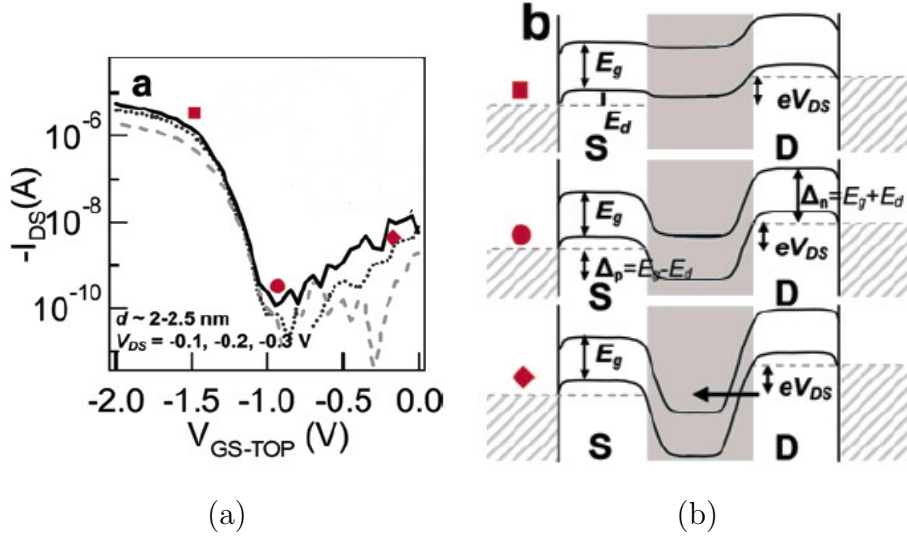
Figure 3.7: **(a)I–V characteristics of p-type MOS CNTFETS at three different drain voltages (dashed curve, VDS = $-0.1V$; dotted, VDS = $-0.2V$; solid, VDS = $-0.3V$) (b) Corresponding band diagram of the transistor at three different points (I_{ON}, I_{min} and $I_{n-channel}$) [50]**

3.2 SB CNTFETs device and circuit models

3.2.1 Why SB CNTFET?

Digital circuit designers may not prefer SB CNTFET for their applications. It suffers from relatively high OFF current and ambipolar characteristics. However, from manufacturing point of view it would be the best choice. As we will describe later in this chapter, SB CNTFET can work as n-type or p-type transistor by adjusting its biasing voltages. This means that we will not need separate manufacturing steps for n and p transistors. Any reduction in the number of fabrication steps enhances the yield of the whole process. This reduction is not possible with other transistors as we will need to produce n-doped and p-doped devices in separate steps.

Doping of CNTs is in itself another problem. Experiments showed that n-doped CNTs lose their doping when exposed to ambient air. This is because of the reactivity of K atoms used for doping [49]. On the other hand, fabricated
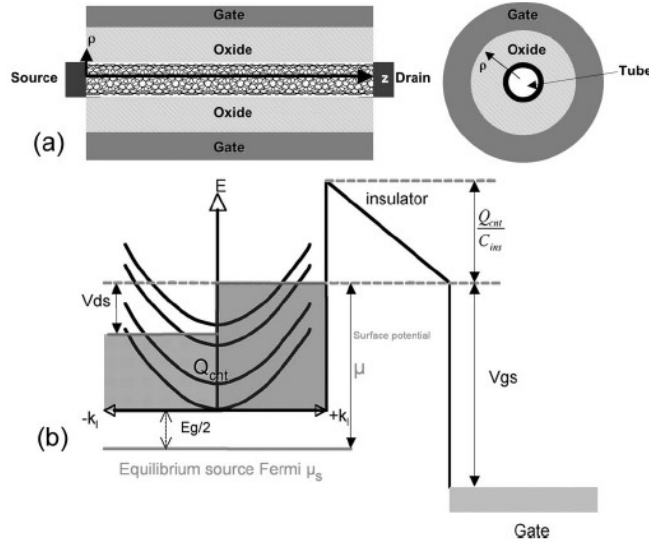
Figure 3.8: **(a)Cross sections of the device along the tube axis and perpendicular to it. (b) Band diagram of the transistor gate stack in the radial direction with** $E - k$ **diagram of the CNT [53].**

p-type MOS CNTFETs used a back gate to make electrostatic doping for the transistor channel. This method is not suitable for coaxial transistors.

Finally, high OFF current of SB CNTFETs may make them inefficient for low power applications, however, they will be useful for high performance digital applications due to their high ON current. State of the art SB CNTFET reported by Javey et al. [52] showed ON current as high as $25\mu A$.

3.2.2 SB CNTFET device model

Though several models were developed to describe the behavior of the SB CNT-FET, only few of them captured the real transistor characteristics. For example, the model developed by Natori et al. [54] failed in describing obtained experimental results. The inaccuracy of the model arises because the authors neglected transistor nonidealities like the Schottky barriers at the CNT/metallic contact interface and considered it as a ballistic device.

In our simulations, we have used Hazeghi model [53] which was an improve-

ment of Natori model [54]. This model considered real device nonidealities and showed a very good agreement with experimental results. In addition it studied the coaxial structure with needle contacts (Fig.(3.8)) which is the optimal choice for these transistor types as we stated earlier in this chapter.

The model begins with the assumption of ballistic transport between ideal S/D reservoirs. When the gate voltage is adjusted to V_{gs} and drain voltage to V_{ds}, we get the band diagram shown in Fig.(3.8). In this case, $+k_l$ states of the CNT are filled by charges injected from the source, while $-k_l$ states are filled by the charges injected from the drain. For such a system, ballistic current I_d can be calculated using Landauer-Buttiker formula:

$$I_d = \frac{2q}{h} \sum_i \int_{E_{i,min}}^{E_{i,max}} (f_s(E, \mu) - f_d(E, \mu))dE \tag{3.1}$$

where μ is the surface potential of the CNT with respect to the Fermi energy of the source and $E_{i,min}$, $E_{i,max}$ are the minimum and maximum energies of the ith subband. Summation is done over all subbands contributing to current conduction.

To calculate the current I_d, we have to obtain the value of the chemical potential μ. According to the biasing voltages applied, the following equation must be satisfied:

$$V_{gs} = V_{fb} + \frac{\mu}{q} + \frac{Q_{CNT}}{C_{ins}} \tag{3.2}$$

where V_{fb} is the flat band voltage, C_{ins} is the oxide capacitance per unit length and Q_{CNT} is the charge per unit length of the CNT which is calculated by:

$$Q_{CNT} = q \sum_i \int_{E_{i,min}}^{E_{i,max}} \frac{g_i(E)}{2} (f_s(E, \mu) + f_d(E, \mu))dE \tag{3.3}$$

where $g_i(E)$ is the density of states of the ith subband.

By solving the two equations (3.2) and (3.3) together self consistently, the surface potential μ is retrieved. Then, the current I_d will be calculated knowing that f_s and f_d are the S/D Fermi distributions given by:

$$f_s(E, \mu) = \frac{1}{1 + e^{\frac{E - \mu}{k_B T}}} \tag{3.4}$$

$$f_d(E, \mu) = \frac{1}{1 + e^{\frac{E - \mu + V_{ds}}{k_B T}}} \tag{3.5}$$

Now, we have to capture the effect of the Schottky barriers and include them into the model. Hazeghi et. al. [53] considered the SBs at the source and drain as two scatterers exist at the CNT/contact interface. To simplify our discussion, assume that we have only one scatterer at the CNT/source interface (Fig.(3.9)) with transmission probability equals $T(E)$. If N_s carriers are trying to jump from the source to the CNT, only $N_s \cdot T(E)$ will succeed and jump to the channel to fill $+k_l$ states carrying the source distribution f_s. Same concept should be applied to the carriers injected from the drain N_d where only $(1 - T(E)) \cdot N_d$ will fill $+k_l$ states carrying the drain distribution. The same actions happen when the scatterer exist at the drain. We have to note that away from the scatterer at lengths exceed energy relaxation length the reflected and transmitted carriers settle down to lower energies to form their Fermi distribution. When we consider the two scatterers at source and drain simultaneously, left movers and right movers carriers will have the following Fermi distributions:

$$f^+ = \frac{T_s f_s + T_d f_d - T_s T_d f_d}{1 - (T_s - 1) \cdot (T_d - 1)} \tag{3.6}$$

$$f^- = \frac{T_d f_d + T_s f_s - T_s T_d f_s}{1 - (T_s - 1) \cdot (T_d - 1)} \tag{3.7}$$

The transmission coefficients T_s and T_d are determined using WKB approximation. Finally, we have to modify the total charge equation (3.3) and the current equation (3.1) by using the modified carrier distributions f^+ and f^- instead of f_s and f_d.

At this point, we can model individual SB CNTFETs accurately, but we still cannot make circuit simulations.
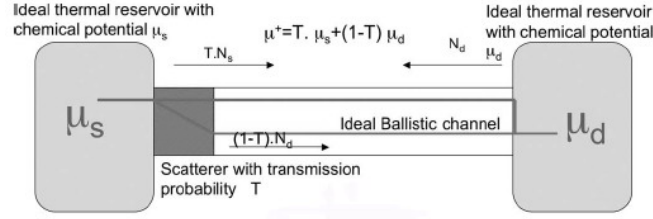
Figure 3.9: **The proposed mesoscopic scattering site at the source side. The drain side is treated in the same way [53].**

3.2.3 SB CNTFET circuit model

The major problem of emerging devices including CNTFETs is the increasing complexity of their physics. Thus analytical models suitable for circuit simulators take a long time and need extreme research efforts to be developed. However, to correctly evaluate any proposed device we need to predict individual device behavior, as well as its performance in larger systems. As a result of that we have to provide a fast and accurate method to figure out the performance of the circuits built with these devices.

As we discussed in Sec.(3.2.2), SB CNTFET model developed by Hazeghi et al. [53] is a very good device model. Unfortunately, we cannot use it directly for circuit simulations because the device equations are solved iteratively. To overcome this problem, we used Look Up Table (LUT) modeling technique.

LUT Model structure

LUT modeling technique is the most suitable method for emerging devices with no available circuit model. It consists of three major parts: (a) Data LUTs, (b) search function, and (c) interpolation function.

The first step of this model is to collect the values of the device parameters such as drain current. These parameters can be obtained using either the device model or practical experiments. The collected data is then stored in indexed tables ready for use in circuit simulation.

In our model, we used SB CNTFET model described earlier to prepare a LUT of the transistor electrical characteristics (V_{gs}, V_{ds} and the corresponding drain current I_d). To improve the accuracy of our simulations, we have prepared high density tables with small step ($0.01V$) between different entries of V_{gs} and V_{ds}. When the given value of V_{gs} or V_{ds} does not exist in the table, we use $2D$ interpolation to find out the drain current. Hence, we can obtain full I–V characteristics of our device as if we have a closed form function for the current $I_d = f(V_{gs}, V_{ds})$. However, this will not work properly for voltages outside the range of the LUT.

The accuracy of this simulation technique can be controlled at three levels: (a) The accuracy of the device model itself, (b) the density of used LUTs, and (c) the interpolation method used. In our simulations, we used linear interpolation method. The main advantage of this method is that it is not time consuming and gives accurate results with high density tables as in our case. More accurate interpolation methods will be necessary with low density LUTs.

Circuit simulation procedure

Now, we can simulate any SB CNTFET circuit using the aforementioned LUT model in a simple way. We first extract the targeted circuit equations in terms of transistor parameters: V_{gs}, V_{ds} and I_d. The resulting set of equations is then solved using the LUT model. Fig.(3.10) summarizes the complete circuit simulation procedure.

Advantages of this simulation procedure are summarized in the following points:

- Easy to implement

- Extendable to other coaxial CNTFET devices.

- Isolate complexity of device model physics from circuit design.

- Controllable accuracy.
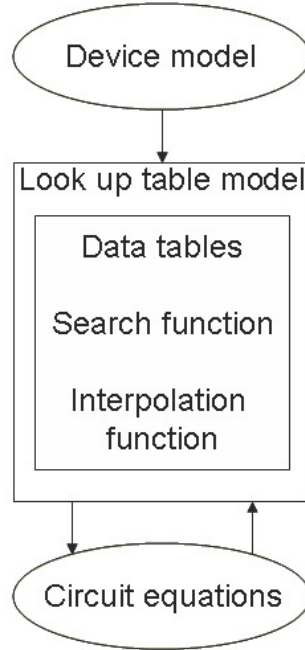
Figure 3.10: **SB CNTFET circuit simulation procedure.**

- Real device nonidealities is included automatically.

3.3 SB CNTFET inverter

3.3.1 SB CNTFET device parameters

In this study, we chose the coaxial SB CNTFET structure with needle contact which is the optimal device structure. A semiconducting CNT with chirality vector: (19,0) and length of 100 nm was used. The metallic source and drain contacts have a cylindrical shape with the same diameter of the tube. We expect that the future devices will use metallic CNTs as the contacts. In this case, the Fermi level of the metallic contact will be aligned to the middle of the channel band gap (i.e. we have mid-gap Schottky Barrier). The gate oxide used is HfO$_2$ with dielectric constant $k \approx 20$. The thickness of the gate oxide is 4 nm (EOT ≈ 0.8 nm). The device structure parameters are summarized in the following
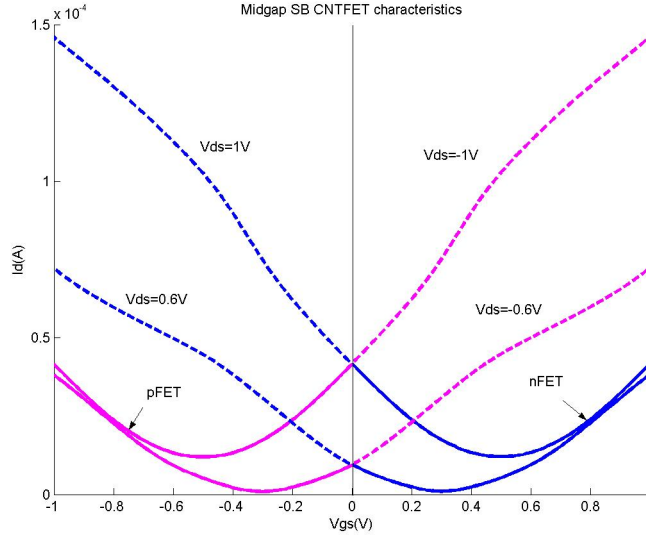
Figure 3.11: **I–V characteristics of our mid-gap SB CNTFET with $V_{fb} = 0$.**

table:

Nanotube Chirality	$(19, 0)$
Nanotube Diameter	1.5 nm
Nanotube Length	100 nm
Oxide Thickness	4 nm
Dielectric Constant	20
Barrier Height	0.5 of channel bandgap

The I–V characteristics of this transistor is shown in Fig.(3.11) for both p-type and n-type transistors. We have to declare that the pFET and nFET transistors characteristics shown are of the same device, but with only an inverted sign of V_{gs} and V_{ds}. The names nFET and pFET are an indicator to the charge carrier type in the region of interest. In addition the names represent their role in the inverter circuit as we will see. This is an advantage for the SB CNTFET as we do not need doping to invert the transistor type. In addition, we have identical performance for the two types. The characteristics shows also the ambipolar behavior of the transistor. Besides, minimum current occurs only when $V_{gs} = V_{ds}/2$, while

at $V_{gs} = 0$ the transistor can be considered ON. This behavior is not suitable for CMOS architecture circuits and will cause significant degradation in their performance as we will present.

We performed all device simulations with "Schottky-Barrier CNFET" simulator available online [55]. We tabulated the results of this device simulator and imported it into Matlab to start circuit simulations.

3.3.2 Inverter DC analysis

Inverter is the stem of all logic gates. Its performance and characteristics can be extended to more complex gates such as NAND and XOR [56]. Thus, we focused our study on SB CNTFET inverter to investigate the capabilities of future SB CNTFET technology. We applied the circuit simulation procedure discussed in Sec.(3.2.3) to estimate the inverter performance. The inverter we designed uses two identical SB CNTFETs one of them works as pFET and the other as nFET (Fig.(3.12)). In this simple circuit we have two equations that govern the currents and voltages of the transistors:

$$I_{d_n} = I_{d_p} \tag{3.8}$$

$$V_{gs_n} + V_{sg_p} = V_{DD} \tag{3.9}$$

We included the two equations in the Matlab environment we prepared to simulate the static behavior of the transistor.

The first point we want to investigate is the capability of the mid-gap SB CNTFET to realize CMOS architecture. The main obstacle is the ambipolar characteristics of the transistor with minimum current at $V_{gs} = V_{ds}/2$. The Voltage Transfer Characteristics (VTC) of the inverter designed using these devices is shown in Fig.(3.12).

The resulting characteristics is very good in terms of gain. As depicted in Fig.(3.12), the gain of this inverter is similar to that of the traditional CMOS inverter. Unfortunately, the voltage swing of the inverter is very poor. Thus we

(a)   (b)
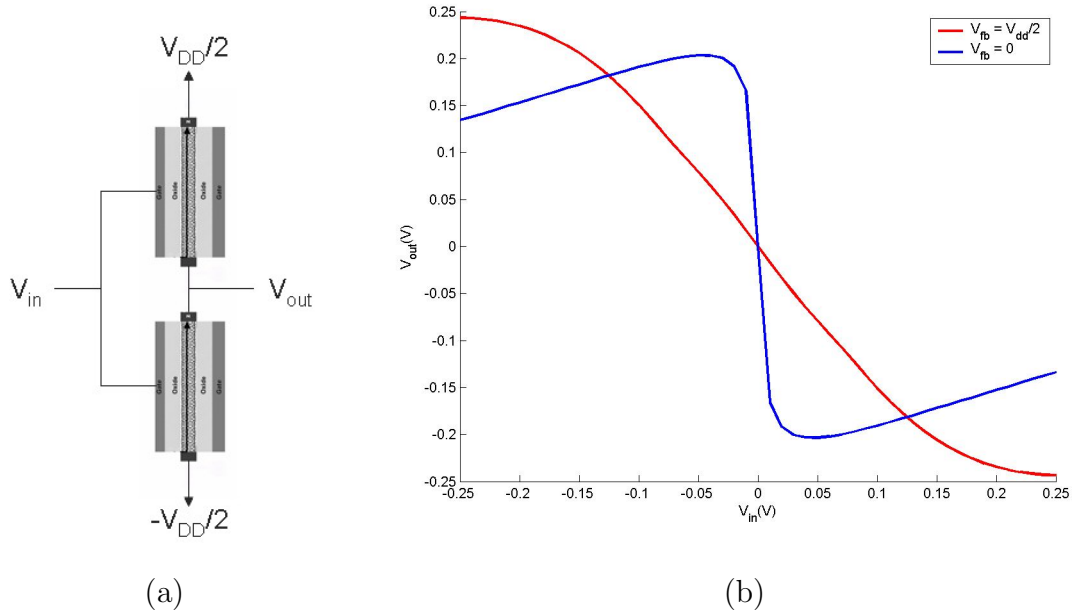
Figure 3.12: **(a)Schematic of inverter circuit (b) VTC of the two inverters:** $V_{fb} = 0$ **(blue curve) and** $V_{fb} = V_{DD}/2$ **(red curve)**

lose a major advantage in CMOS architecture where we have full voltage swing. This problem arises from the current flows through either transistors at $V_{gs} = 0\,V$. In contrast, Si CMOS transistor has almost zero drain current at $V_{gs} = 0\,V$.

To restore the performance of the inverter, we have to shift both of the transistors characteristics such that the minimum current occurs when $V_{gs} = 0$ instead of $V_{DD}/2$. i.e. we have to shift the nFET characteristics to the left by $V_{DD}/2$ and the pFET characteristics to the right by the same value. This can be easily done by adjusting the flat band voltage (V_{fb}) of the two transistors to the value $V_{DD}/2$. This modification greatly enhances the voltage swing as shown in Fig(3.12). Unfortunately, this was accompanied by noticeable degradation in the inverter gain. In Fig(3.13), we compare between the voltage swing of the two circuits ($V_{fb} = 0\,V$ and $V_{fb} = V_{DD}/2$). We notice that the voltage swing degrades in both cases as the supply voltage increases. This is a direct result for the increase in the minimum transistor current at higher biases (refer to Fig.(3.11)).

Practically, V_{fb} can be adjusted by choosing appropriate gate material with
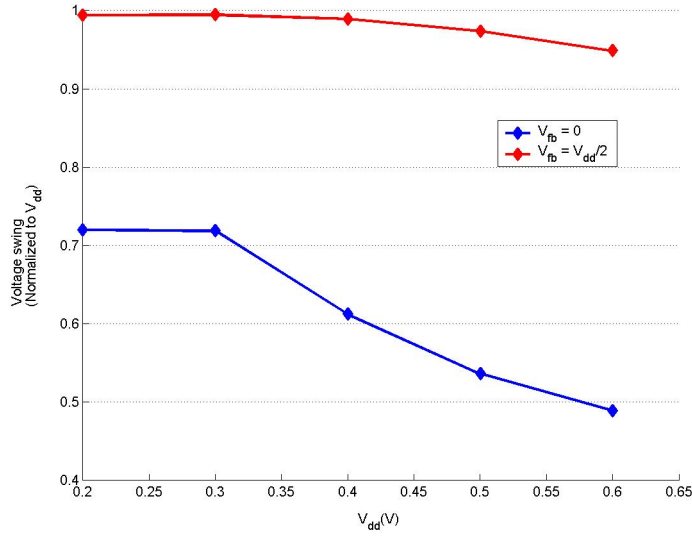
Figure 3.13: **The voltage swing of the two inverters normalized to supply voltage**

suitable work function. This was experimentally verified by Chen et al. [57]. In their study, they fabricated a ring oscillator on a single CNT. to get an adequately operating circuit, they used two different gate materials; Al for the nFET and Pd for the pFET. Fig.(3.14) shows the experimental results of the I–V characteristics of the two transistors and the resulting inverter. As depicted in the figure, the I–V characteristics of the nEFT was not precisely shifted by $V_{DD}/2$ at the supply voltage $V_{DD} = 0.5$ V. This is directly reflected on the resulting non symmetric inverter characteristics (Fig.(3.14)).

The difficulty of this method lies in the necessity of changing the used gate material when the supply voltage (V_{DD}) is scaled down. In addition, we are limited to materials that can be integrated in the manufacturing process.

To estimate static power consumption of CNTFET future chips, we assumed that we have 10^9 inverters/cm^2 as expected by ITRS [2]. Fig.(3.15) shows the static power density using the two transistor types ($V_{fb} = 0$ and $V_{fb} = V_{DD}/2$). Chips fabricated with $V_{fb} = 0$ transistors have unacceptable static power density. For the other types of transistors, static power density is significantly less. At supply voltage $V_{DD} = 0.5$ V the static power density is less than 200 W/cm^2

(a)   (b)
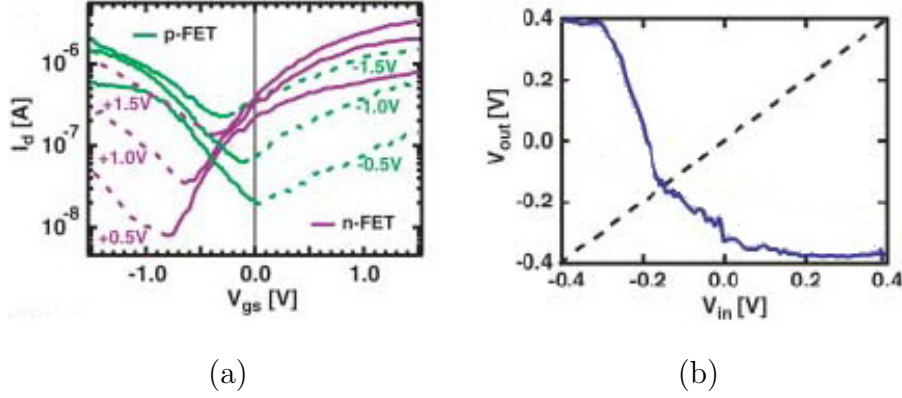
Figure 3.14: **Experimental results of (a) nFET and pFET I–V characteristics and (b) VTC of the inverter [57].**

which is the upper limit of the low power digital applications specified by ITRS.

3.3.3   Inverter transient analysis

To complete the picture, we have to investigate the transient behavior of the SB CNTFET inverter. To obtain an adequate result that reflects the real performance in large integrated circuit, we used a multi-stage fan-out of 4 (FO4) inverter chain.

To start our analysis, we assume that each transistor drives a pure capacitive load C_L representing the load inverter. This is possible as long as we are neglecting the gate tunneling currents which is an acceptable assumption. Study conducted by Lu et al. [58] showed that the gate tunneling current of CNTFETs is in the order of pA for ultra thin (3 nm) high-k dielectric transistors.

The total capacitance of each transistor is given by [59]:

$$C_g^{-1} = C_{es}^{-1} + 4C_Q^{-1} \tag{3.10}$$

where C_Q is the quantum capacitance and C_{es} the total electrostatic capacitance.

The quantum capacitance arises in low dimensional systems such as CNTs due to the quantization effects in these low dimensional systems. In CNTs, the
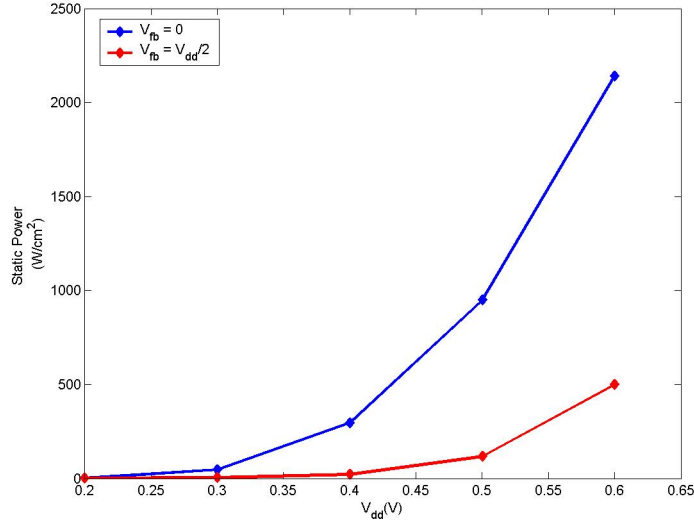
Figure 3.15: **Static power density of the two inverter types**

quantum capacitance is given by [59]:

$$C_Q = \frac{q^2}{\hbar \pi v_F} \tag{3.11}$$

where v_F is the CNT Fermi velocity.

We note that C_Q in equation(3.10) is multiplied by 4. This is because of the bandstructure of the CNT. In CNTs each subband is equivalent to 4 conducting channels: 2 channels due to degeneracy and 2 channels due to spin up and spin down electrons [60]. For CNTs, $C_Q \approx 100 \ aF/\mu m$, thus for our device it is $4 \times 10 \ aF$.

We calculated the total electrostatic capacitance C_{es} using FASTCAP [61]. The input file to the FASTCAP specifies the discretization of the conductor surfaces into panels. We used Matlab to generate the cylindrical conductors grids that describe our transistor geometry.

The electrostatic capacitance includes the parasitic capacitance arising from fringing fields from gate to the metal contacts at both sides. This is the only source of parasitics according to our supposed structure. This parasitic capacitance depends on the thickness of the gate electrode which is determined by the
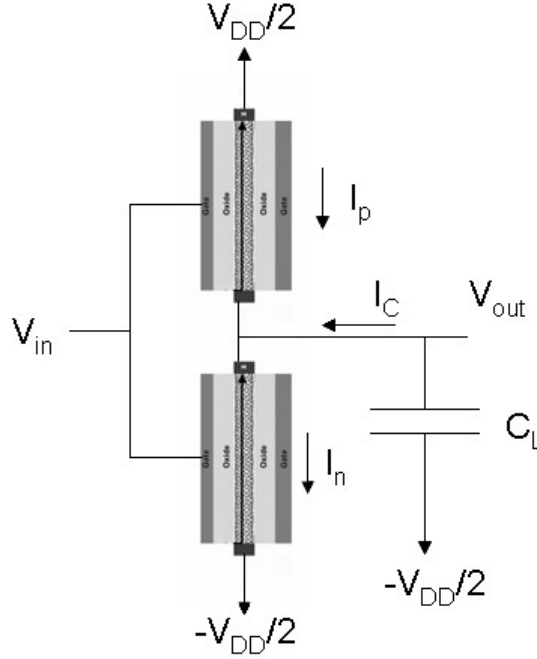
Figure 3.16: **Inverter circuit used for transient analysis**

fabrication technology. Assuming thin gate electrode with respect to other dimensions, the total electrostatic capacitance is about 66 aF. This value is much less than that reported for planar transistors whose parasitic capacitance in the range of fF [62].

We neglected the metal contacts resistance since the minimum channel resistance is at best 6.5 $K\Omega$ and only contacts with resistance 10 $K\Omega$ or higher affect the performance [62].

Fig.(3.16) shows the loaded inverter circuit. In this case the equations govern the circuit are:

$$I_{d_p} + I_C = I_{d_n} \tag{3.12}$$

$$C_L \left(-\frac{dV_{out}}{dt} \right) = I_C \tag{3.13}$$

The input and output signals of FO4 inverter chains with $V_{fb} = 0$ inverter and $V_{fb} = V_{DD}/2$ inverter are shown in Fig.(3.17) and Fig.(3.18) respectively. The inverters operate at $V_{DD} = 0.5\ V$ and the input frequency is 10 GHz. As we can
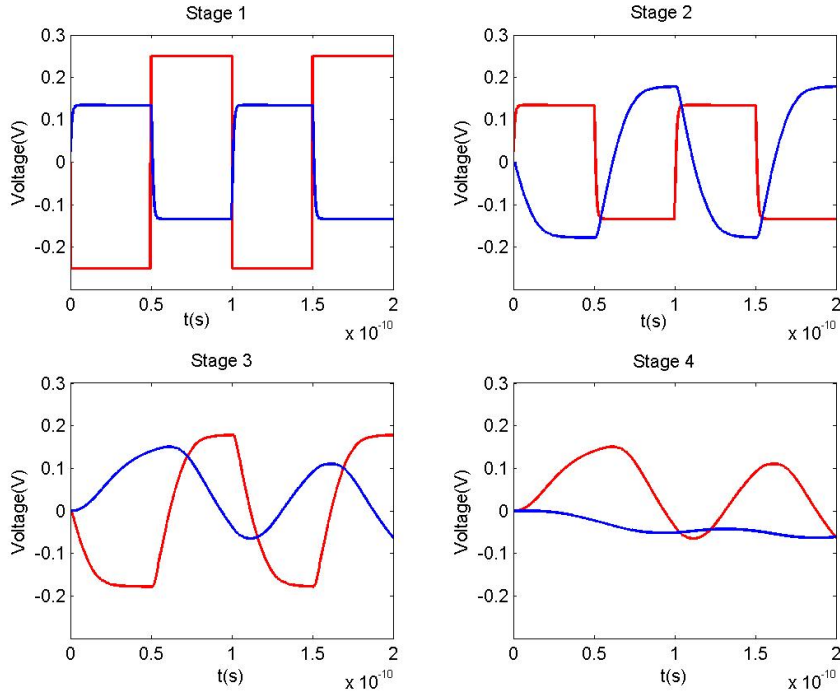
Figure 3.17: **The input (red lines) and output (blue lines) voltages of the inverter chains with $V_{fb} = 0$**

see in the figures, logic is completely destroyed after the 4th stage for the case of $V_{fb} = 0$.

To estimate the propagation delay of the inverter in practical applications, we calculated the propagation delay at stage 3 of the inverter chain. At stage 3, the input signal has more realistic shape than the ideal square wave. Results are shown in Fig.(3.19). It is clear that $V_{fb} = V_{DD}/2$ is much better especially at low supply voltages.

3.4 Conclusion

To correctly evaluate CNTFETs, we should not depend on their individual characteristics, but we should also investigate their performance in electronic circuits. The major advantage of this work is that we could obtain such complete pic-
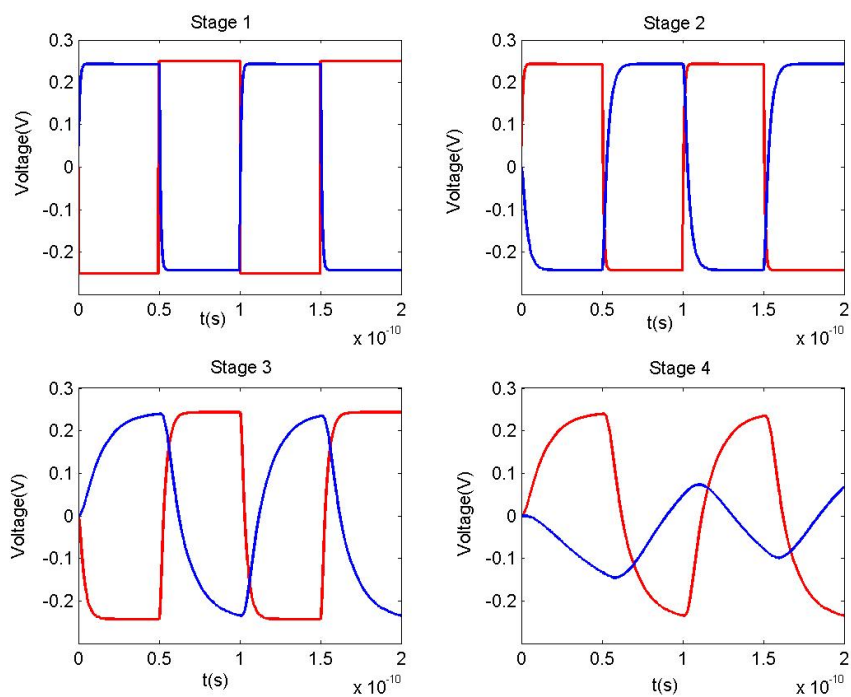
Figure 3.18: **The input (red lines) and output (blue lines) voltages of the inverter chains with** $V_{fb} = V_{DD}/2$
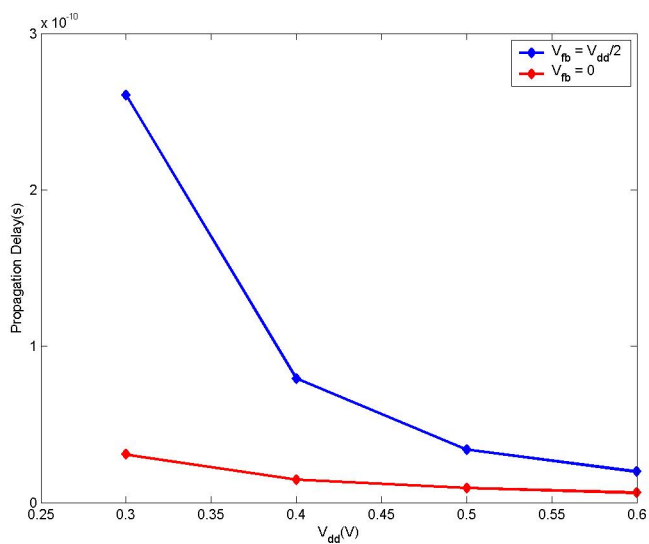
Figure 3.19: **Propagation delay vs supply voltage at stage 3 of the FO4 inverter chain**

ture by providing our circuit simulation environment. Our results regarding SB CNTFETs is a clear evidence for this idea. The performance of individual SB CNTFET as individual device is independent of the flat band voltage. However, our circuit simulations showed that the midgap SB CNTFET with $V_{fb} = 0$ does not satisfy any of the requirements for future digital applications. On the other hand, the DC and transient performance of $V_{fb} = V_{DD}/2$ transistors are better but the fabrication may be more difficult to adjust the correct flat band voltage.

For the power consumption, mid-gap SB CNTFET with $V_{fb} = V_{DD}/2$ satisfies the requirements for low power applications at supply voltage $V_{DD} = 0.5\ V$ expected in the year 2020, taking into consideration the good heat conduction ability of CNTs.

Thus we can say that CNTFETs do not employ the great characteristics of CNTs efficiently. So we are still looking for better device structures to use CNTs efficiently and find a replacement to CMOS.

Chapter 4

Multi mode transport in CNTs

CNT is a very promising material with unique physical properties. In this chapter we try to dive deeper in CNTs physics to get better understanding to the electronic transport through them. Actually, we are interested in the role of subbands in conduction. For the first time in literature, we tried to investigate the possibility of multimode propagation in CNTs. By understanding the nature of subbands and how subbands electrons interact we can find certain excitation modes that improves electron flow in CNTs. To the best of our knowledge, no detailed study has been done to address the interaction between electrons propagating in different subbands. This complicated our study because there is no systematic method to follow. This chapter pave the way to other researchers to make more extensive studies in that direction.

4.1 CNT subbands observation

One of the clear experimental observation of CNT subbands was reported by Appenzeller et al. [63]. Appenzeller and coworkers measured the current of a SB CNTFET with heavily doped n-type CNT. As depicted in Fig.(4.1), current experience step increase at certain biasing voltages. This behavior can be understood from the CNT band diagram shown in Fig.(4.2). The figure shows the position
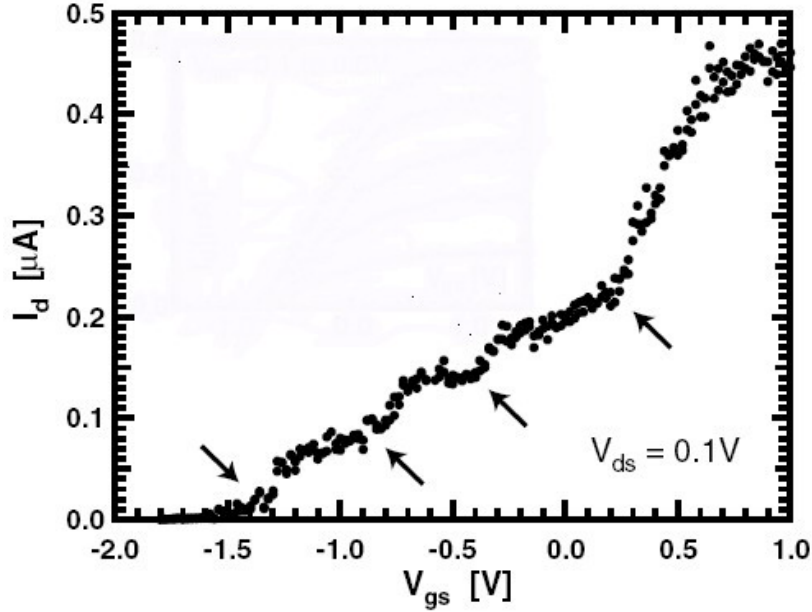
Figure 4.1: **Experimental I–V characteristics of heavily doped channel SB CNT-FET. Small arrows indicate the step increase in current due to new contributing subbands [63].**

of the 1st and 2nd subbands at different biasing voltages. When the 2nd subband enters the conducting region between source and drain, additional conducting channel contribute to the conduction and the current will increase in stepwise manner. Thus, current carrying capacity of CNTs can be improved by allocating more subbands to current conduction.

Burke [60] reported another attractive point regarding subbads. Burke modeled carrier transport through crossing subbands of a metallic CNT using transmission line model. He used four independent transmission lines: 2 of them arises from the degeneracy of CNT subbands and the other 2 lines to represent spin up and spin down electrons in each channel. Due to the interaction between electrons in these four channels, transmission lines are not totally independent, but they are coupled together through the electrostatic capacitance (Fig.(4.3)). This work did not consider the role of higher subbands in carrier transport. Thus, we still need to discover how can we model them. We need also to find out whether they
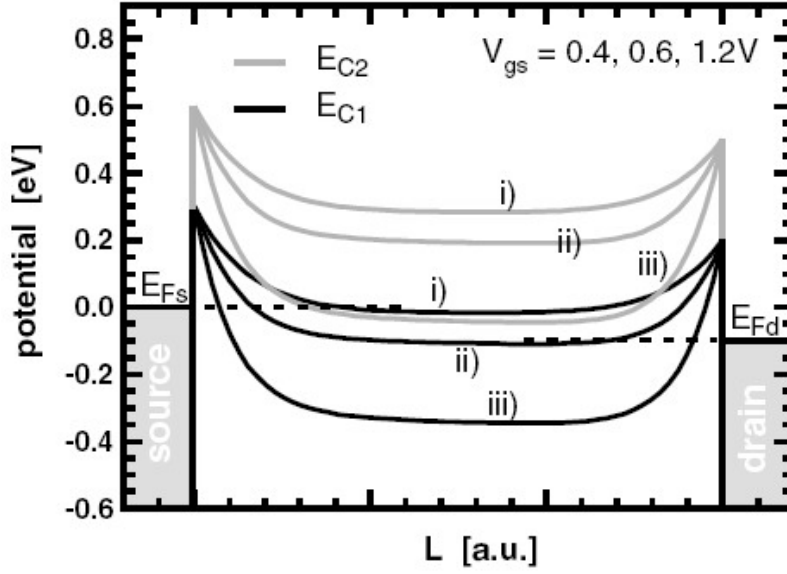
Figure 4.2: **Band diagram of the proposed SB CNTFET indicating the position of the 1st and 2nd subbands at different gate voltages:i)** $V_{gs} = 0.4V$ **ii)** $V_{gs} = 0.6V$ **iii)** $V_{gs} = 1.2V$[**63**].

are really independent like transmission lines or not. We then have to answer the following question: "Can we send different information over different subbands?".

4.2   Hamiltonian and velocity matrices of CNTs

We will start our trials by following Supriyo Datta in his analysis of quantum wires [19]. For any quantum wire including CNTs we can define matrix $[h(k)]$ (we will refer to it as k-dependent Hamiltonian matrix) and the velocity matrix $[v(k)]$. They are related together through the relation:

$$[v(k)] = \frac{1}{\hbar}\frac{d}{dk}[h(k)] \qquad (4.1)$$

If $[h(k)]$ and $[v(k)]$ can be simultaneously diagonalized, then the quantum wire will be represented in terms of independent subbands that can conduct in parallel [19]. In this case the diagonal elements of the velocity matrix will
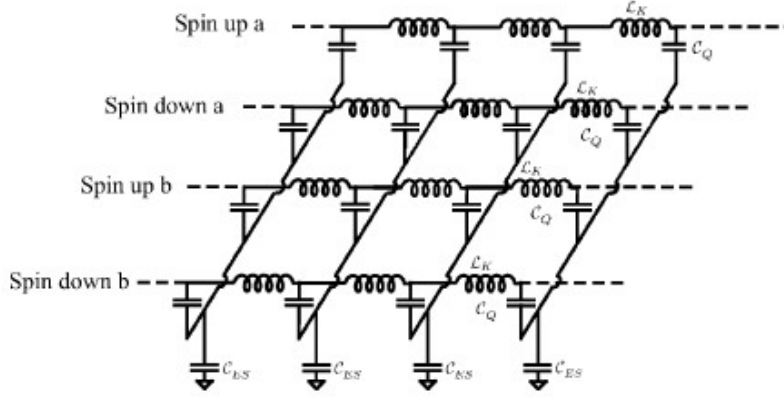
Figure 4.3: **Transmission line model of interacting electrons in CNT [60].**

represent the velocity of each propagating mode. Hence, equ.(4.1) reduces to the usual definition of the Bloch velocity:

$$v_n(k) = \frac{1}{\hbar} \frac{dE_n(k)}{dk} \tag{4.2}$$

where v_n is the group velocity of subband n and $E_n(k)$ is the dispersion relation of subband n.

We will apply this concept to zigzag CNTs to check its subband independence. First, we will deduce $[h(k)]$ and $[v(k)]$ for a zigzag CNT. Then, we will check their commutator to find out the ability of simultaneous diagonalization of both of them.

4.2.1 Origin of $[h(k)]$ and $[v(k)]$

The general Hamiltonian of a $1D$ quantum wire as that shown in Fig.(4.4) is given by:
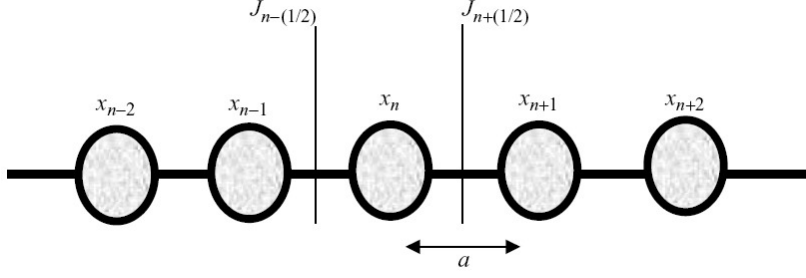
Figure 4.4: 1D **chain of unit cells represents a quantum wire.**

$$[H] \;=\; \begin{bmatrix} \cdots & \cdots & \cdots & \cdots & \cdots & \cdots & \cdots \\ \cdots & \alpha & \beta & 0 & 0 & 0 & \cdots \\ \cdots & \beta^{\dagger} & \alpha & \beta & 0 & 0 & \cdots \\ \cdots & 0 & \beta^{\dagger} & \alpha & \beta & 0 & \cdots \\ \cdots & \cdots & \cdots & \cdots & \cdots & \cdots & \cdots \end{bmatrix} \tag{4.3}$$

$[\alpha]$ and $[\beta]$ are block submatrices represent the coupling within the same unit cell and the coupling between adjacent unit cells respectively. Also, $\beta^{\dagger}$ is the complex conjugate of β. The dimensions of them is determined according to the number of basis functions of each unit cell.

The time independent Schrodinger equation of the wire is:

$$\alpha \psi_n + \beta \psi_{n+1} + \beta^{\dagger} \psi_{n-1} = E \psi_n \tag{4.4}$$

Due to the periodicity of this structure, the wavefunctions must satisfy Bloch theorem:

$$\psi_{n\pm1} = \psi_n e^{\pm ika} \tag{4.5}$$

where a is the separation between adjacent unit cells.

Hence, Schrodinger equation can be written in the form:

$$\begin{aligned} (\alpha + \beta e^{ika} + \beta^{\dagger} e^{-ika}) \psi_n &= [h(k)] \psi_n \\ &= E(k) \psi_n \end{aligned} \tag{4.6}$$

where $[h(k)]$ is the aforementioned reduced Hamiltonian matrix and is given by [19]:

$$[h(k)] = \alpha + \beta e^{(ika)} + \beta^\dagger e^{(-ika)} \tag{4.7}$$

It is clear from equ.(4.6) that the eigenvalues of $[h(k)]$ gives the energy dispersion relation $E(k)$ of the wire. Eigenvectors of these eigenvalues represent the modes or subbands state vectors of the wire.

For our $1D$ chain, the current can be defined as:

$$
\begin{aligned}
J_{n+\frac{1}{2}} &= q\frac{a}{i\hbar}(\psi^\dagger_{n+1}\beta^\dagger\psi_n - \psi^\dagger_n\beta^\psi_{n+1}) \\
\\
&= q\psi^\dagger_n\frac{a}{i\hbar}(\beta^\dagger e^{-ika} - \beta e^{ika})\psi_n \tag{4.8}
\end{aligned}
$$

By comparing equ.(4.8) with the general expression of the current density $J = qnv$, we can define the velocity matrix as [19]:

$$[v(k)] = \frac{a}{i\hbar}(\beta^\dagger e^{(-ika)} - \beta e^{(ika)}) \tag{4.9}$$

4.2.2 $[h(k)]$ and $[v(k)]$ of zigzag CNTs

To obtain α and β of a CNT, we have to choose a suitable unit cell so that the CNT can be represented as a $1D$ chain of unit cells. Fig(4.5) shows a graphene sheet that will form a zigzag $(n,0)$ CNT when rolled parallel to x-axis. This figure illustrates our choice for the CNT unit cell. Each unit cell contains four rings of atoms: two rings of type A and two rings of type B. The number of atoms in each ring is n. Thus, the total number of atoms in each unit cell is $4n$. As we stated earlier in Sec.(2.3.2), it is sufficient to consider p_z orbital of each carbon atom in electronic conduction. Hence, the total number of basis functions in each unit cell is $4n$ and the dimensions of α and β submatrices are $4n \times 4n$.

(a)

(b)

Figure 4.5: **(a) Graphene sheet that forms a zigzag CNT when rolled. The solid rectangle indicates the chosen CNT unit cell. (b) Representation of the CNT as a 1D wire.**
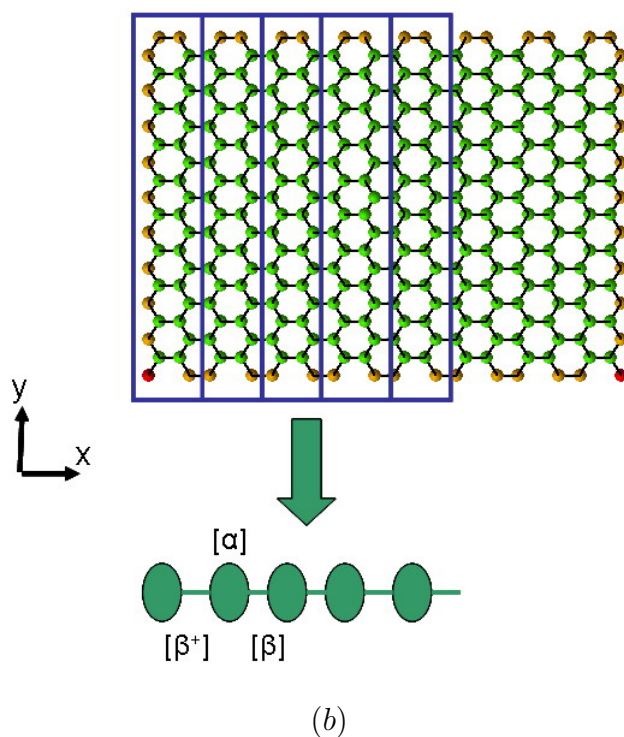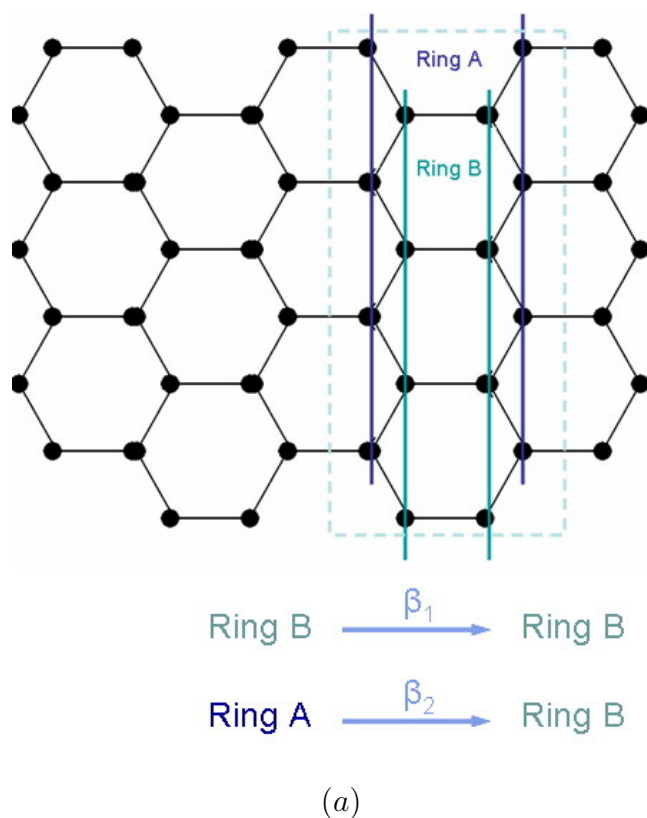
The general Hamiltonain of the shown graphene sheet is given by [20]:

$$[H_{CNT}] = \begin{bmatrix} \cdots & \cdots & \cdots & \cdots & \cdots & \cdots & \cdots & \cdots \\ \cdots & \beta_1^\dagger & \alpha' & \beta_2^\dagger & 0 & 0 & 0 & \cdots \\ \cdots & 0 & \beta_2 & \alpha' & \beta_1 & 0 & 0 & \cdots \\ \cdots & 0 & 0 & \beta_1^\dagger & \alpha' & \beta_2 & 0 & \cdots \\ \cdots & 0 & 0 & 0 & \beta_2^\dagger & \alpha' & \beta_1 & \cdots \\ \cdots & \cdots & \cdots & \cdots & \cdots & \cdots & \cdots & \cdots \end{bmatrix} \qquad (4.10)$$

where submatrix $[\alpha']_{n \times n}$ describes coupling within an A-type or B-type carbon ring and submatrices $[\beta_1]_{n \times n}$ and $[\beta_2]_{n \times n}$ describe the coupling between adjacent rings.

When we apply tight binding approximation to each individual carbon rings of either type (A or B), we find that carbon atoms in the same ring are not coupled together. Thus, the coupling matrix $[\alpha']$ is given by [20]:

$$[\alpha']_{n \times n} = U[I]_{n \times n} \qquad (4.11)$$

where $[I]_{n \times n}$ is the identity matrix and U is the potential of the carbon ring. In our analysis, we assume that the potential U is constant along the CNT. This assumption is valid as long as we are assuming ballistic transport through the CNT [64]. For a ballistic CNT, voltage is divided equally over the two contacts and remains constant along the tube.

Submatrix $[\beta_1]$ describes the coupling between any two adjacent A-type rings or B-type rings and it is given by:

$$[\beta_1]_{n \times n} = [\beta_1]_{n \times n}^\dagger = t[I]_{n \times n} \qquad (4.12)$$

where t is the tight binding parameter of CNTs and approximately equals $3\ eV$ [17].

Submatrix $[\beta_2]$ describes the coupling between adjacent A-type and B-type rings and it is given by:

$$[\beta_2]_{n\times n} \;=\; t \begin{bmatrix} 1 & 0 & 0 & \cdots & 1 \\ 1 & 1 & 0 & \cdots & 0 \\ 0 & 1 & 1 & \cdots & 0 \\ \cdots & \cdots & \cdots & \cdots & \cdots \\ 0 & 0 & \cdots & 1 & 1 \end{bmatrix}_{n\times n} \tag{4.13}$$

Submatrix $[\beta_2]$ is not diagonal like other coupling matrices. As depicted in Fig.(4.5), each atom in an A-type ring is coupled with two atoms from the adjacent B-type ring and vice versa. In addition, the effect of rolling the graphene sheet appears only in the first row of $[\beta_2]$. It shows that first atom in B-type ring is coupled to the first and last atoms of adjacent A-type ring due to the rolling of the graphene sheet.

Comparing Hamiltonian matrix of CNT (equ.(4.10)) with Hamiltonian matrix of general quantum wire (equ.(4.3)), we can deduce the values of α and β for the CNT:

$$[\alpha] \;=\; \begin{bmatrix} \alpha' & \beta_2^\dagger & 0 & 0 \\ \beta_2 & \alpha' & \beta_1 & 0 \\ 0 & \beta_1^\dagger & \alpha' & \beta_2 \\ 0 & 0 & \beta_2^\dagger & \alpha' \end{bmatrix}_{4n\times 4n} \tag{4.14}$$

$$[\beta] \;=\; \begin{bmatrix} 0 & 0 & 0 & 0 \\ 0 & 0 & 0 & 0 \\ 0 & 0 & 0 & 0 \\ \beta_1 & 0 & 0 & 0 \end{bmatrix}_{4n\times 4n} \tag{4.15}$$

Finally, we use equ.(4.7) and equ.(4.9), to get the k-dependent Hamiltonian and velocity matrix of zigzag CNT:

$$[h(k)] = \begin{bmatrix} \alpha' & \beta_2^\dagger & 0 & \beta_1^\dagger e^{-ika} \\ \beta_2 & \alpha' & \beta_1 & 0 \\ 0 & \beta_1^\dagger & \alpha' & \beta_2 \\ \beta_1 e^{ika} & 0 & \beta_2^\dagger & \alpha' \end{bmatrix}_{4n \times 4n} \qquad (4.16)$$

$$[v(k)] = \frac{a}{i\hbar} \times \begin{bmatrix} 0 & 0 & 0 & \beta_1^\dagger e^{-ika} \\ 0 & 0 & 0 & 0 \\ 0 & 0 & 0 & 0 \\ -\beta_1 e^{ika} & 0 & 0 & 0 \end{bmatrix}_{4n \times 4n} \qquad (4.17)$$

When we calculated commutator of $[h(k)]$ and $[v(k)]$, we found that they do not commute. However, we cannot depend on this result to state whether the CNT subbands are independent or not. The current form of velocity matrix leads to this deceiving results as we will illustrate in Sec.(4.2.3).

4.2.3 Validation of $[h(k)]$ and $[v(k)]$ matrices

Validation of $[h(k)]$ matrix

The eigenvalues of the k-dependet Hamiltonian matrix $[h(k)]$ at different values of k represents the dispersion relation of the zigzag CNT $(n,0)$. In order to check the validity of this method we plot the dispersion relation of CNTs: $(9,0)$ and $(7,0)$ and compare the results with those obtained from online simulator CNTbands2.0 [65, 66]. As shown in Fig.(4.6) and Fig.(4.7) the two dispersion relations are identical for the two CNTs. We verified the validity of our dispersion relation calculations to other sizes of zigzag CNTs. Our method can be extended to chiral and armchair CNTs by defining a correct unitcell for both types as we did for zigzag CNT.

We also note that the dispersion relation we have for zigzag CNT are inconvenient at the surface of Brillouin zone. The group velocity at the Brillouin zone face ($k = \pm \pi/a$) must be zero. This condition is not satisfied by the cur-

rent dispersion relation. This means that we are not using the correct Brillouin zone boundaries. The boundaries we used are extracted from the $1D$ CNT lattice. Though we have chosen the smallest possible unit cell for CNT, we must take into consideration the symmetry of the original unrolled graphene sheet. The band structure of CNT is a quantized version of the graphene band structure. Thus, we should use the boundaries of the original graphene Brillouin zone. Fig.(4.8) shows the Brillouin zone of the unrolled graphene sheet and the quantization in k_y direction for zigzag CNT. We note that the correct Brillouin zone boundary will be: $k_y = \pm 2\pi/a$. The final CNT band diagram of (9,0) CNT is shown in Fig.(4.9).

Validation of $[v(k)]$ matrix

The eigenvalues of the velocity matrix should give the group velocities of different subbands. However, when we calculated the Eigenvalues of $v(k)$ at different values of k, we found that we have only three possible eigenvalues: 1.8×10^6 , 0 and $-1.8 \times 10^6 \ m/s$. These eigenvalues are independent of k. From the band diagram of the CNT, this can not be true. In addition, at small values of k (continuum limit), velocity should follow the well defined relation:

$$v = \frac{\hbar k}{m^*} \tag{4.18}$$

Hence, we can not interpret the eigenvalues of the velocity matrix as the group velocities of the system.

To explain this point, we produce the dispersion relation and the velocity matrix for simple $1D$ atomic chain (Fig.(4.10)). We first perform our calculations using a unit cell that contains a single atom. The general Hamiltonian of this simple atomic chain is given by [19]:
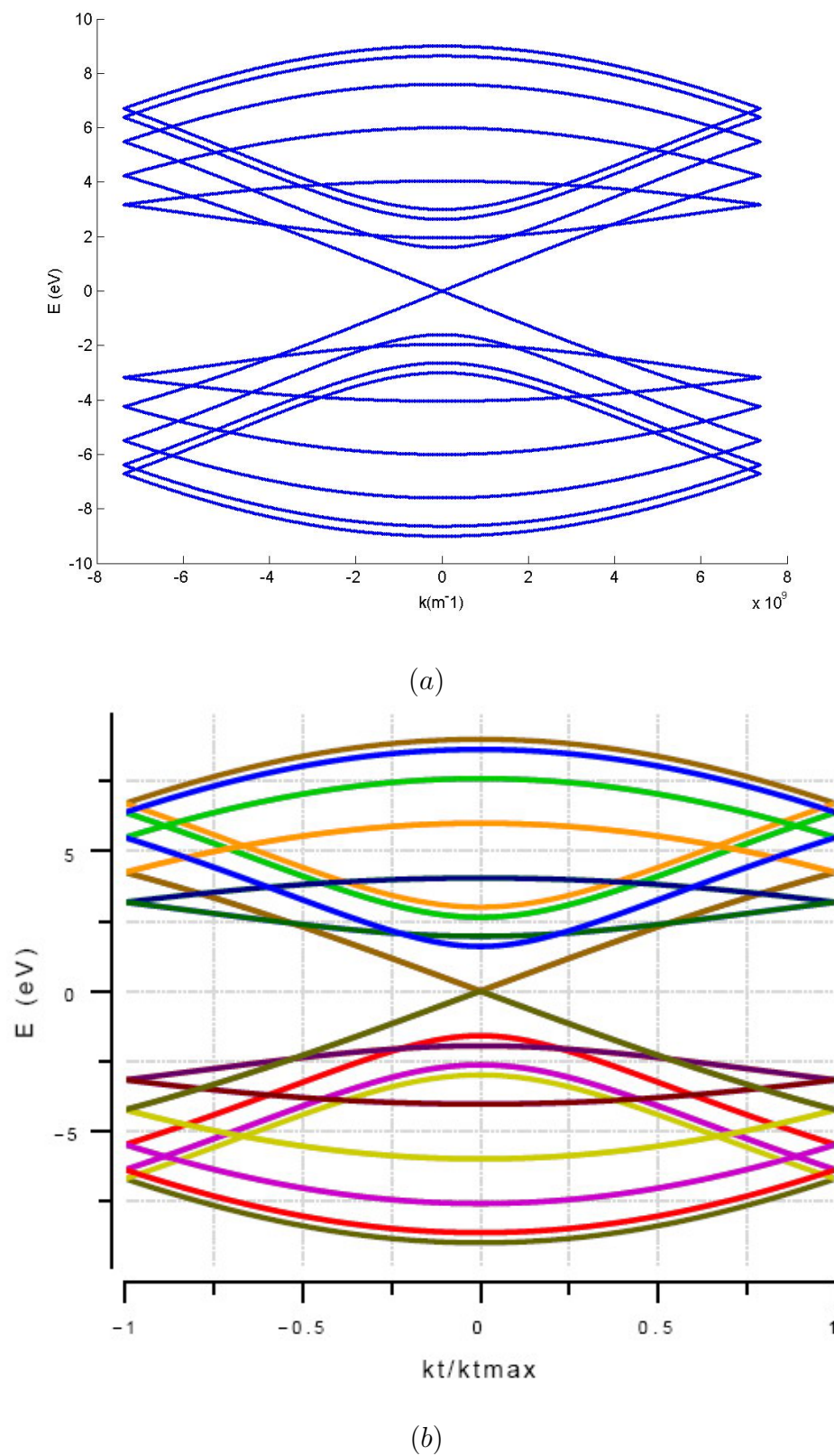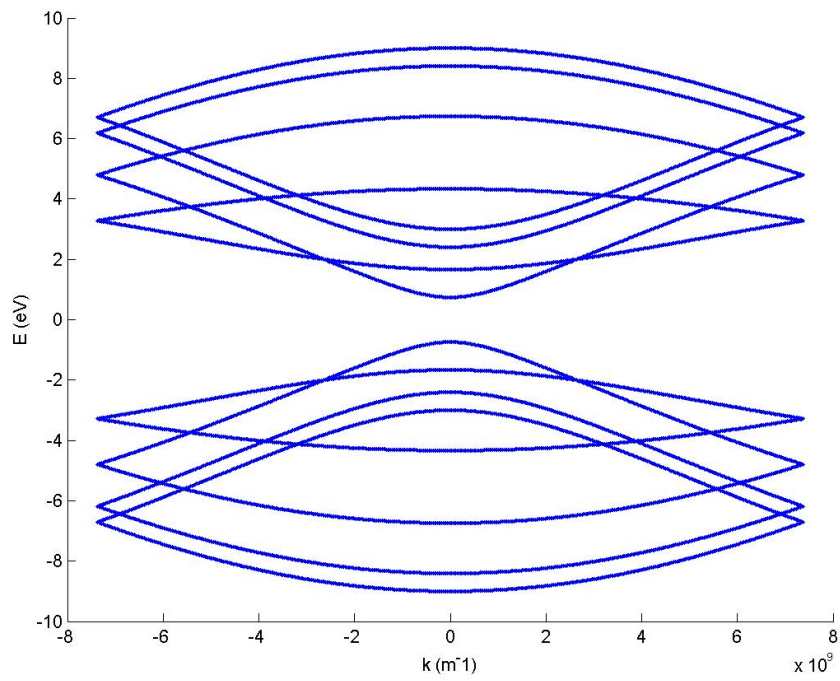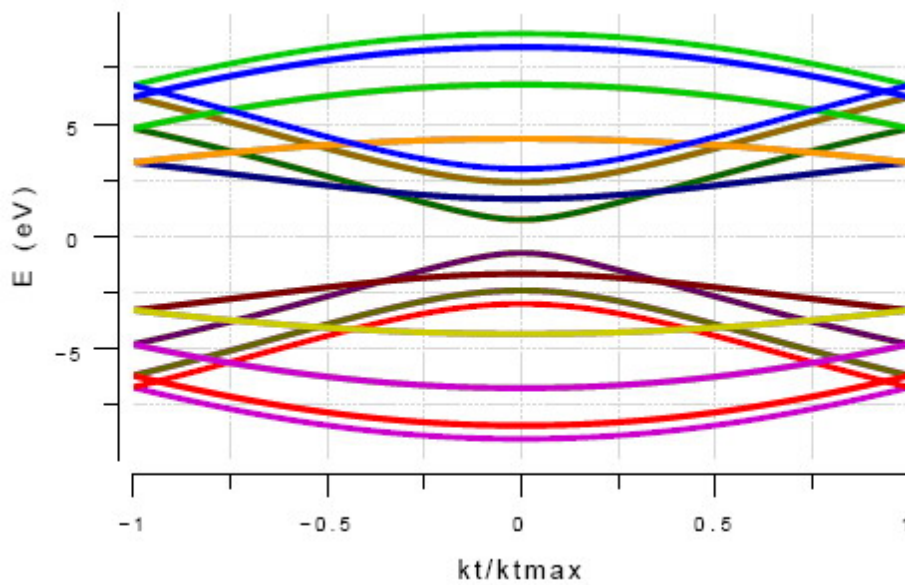
(a)

(b)

Figure 4.6: **Dispersion relation of (9,0) CNT:(a)Eigenvalues of our matrix (b)CNTbands2.0**

(a)

(b)

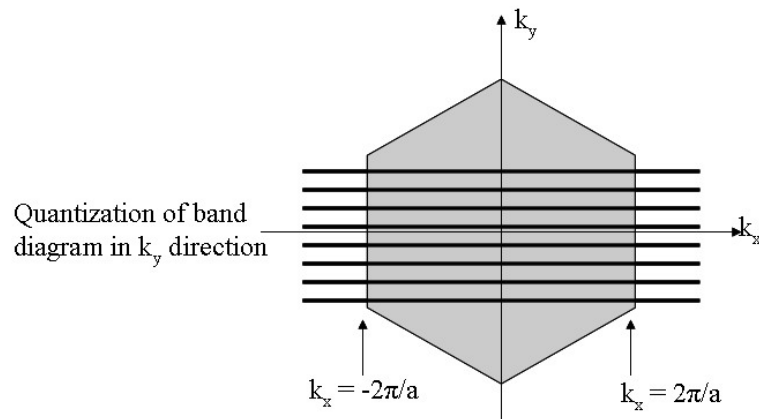Figure 4.7: **Dispersion relation of (7,0) CNT:(a)Eigenvalues of our matrix (b)CNTbands2.0**

Figure 4.8: **Brillouin zone of graphene sheet and the accompanied quantization of CNT k_y.**
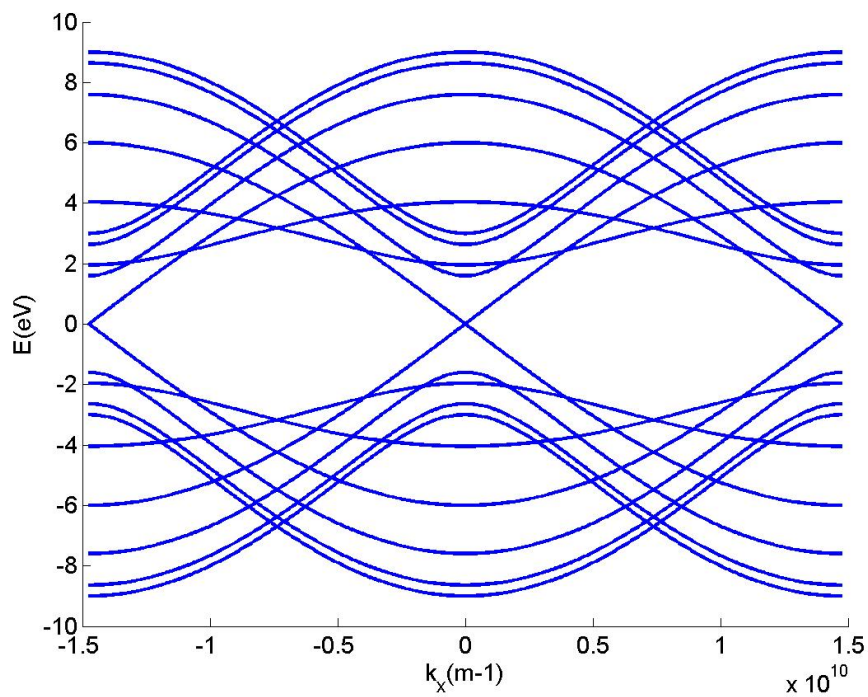
Figure 4.9: **Corrected band diagram of (9,0) CNT.**
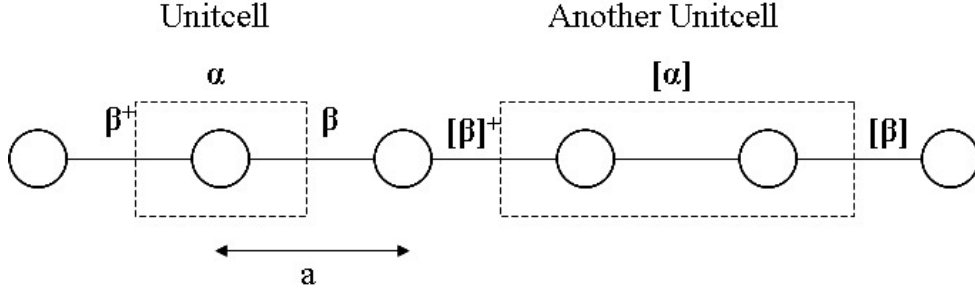
Figure 4.10: **Simple** $1D$ **atomic chain with two different choices for its unitcell.**

$$[H] = \begin{bmatrix} \cdots & \cdots & \cdots & \cdots & \cdots & \cdots & \cdots \\ \cdots & 2t_0 & -t_0 & 0 & 0 & 0 & \cdots \\ \cdots & -t_0 & 2t_0 & -t_0 & 0 & 0 & \cdots \\ \cdots & 0 & -t_0 & 2t_0 & -t_0 & 0 & \cdots \\ \cdots & \cdots & \cdots & \cdots & \cdots & \cdots & \cdots \end{bmatrix} \quad (4.19)$$

where $t_0 = \hbar^2/2ma^2$.

In this case, the coupling matrices are given as: $\alpha = 2t_0$ and $\beta = -t_0$ and the reduced Hamiltonian is:

$$\begin{aligned} h(k) &= 2t_0 - t_0(e^{ika} + e^{-ika}) \\ &= 2t_0(1 - \cos(ka)) \\ &= E(k) \end{aligned} \quad (4.20)$$

The dispersion relation of this simple wire is shown in Fig.(4.11a). The velocity matrix of the wire is:

$$\begin{aligned} v(k) &= -\frac{a}{i\hbar}t_0(e^{-ika} - e^{-ika}) \\ &= \frac{2at_0}{\hbar}\sin(ka) \end{aligned} \quad (4.21)$$

This velocity correctly satisfies the continuum limit and is identical to Bloch velocity (equ.(4.2)).

Now, we will solve the same problem but with a different choice for the unit cells; we will use unit cells that contain two atoms. In this case, the coupling matrices $[\alpha]$ and $[\beta]$ are 2×2 matrices and are given by:

$$[\alpha] = \begin{bmatrix} 2t_0 & -t_0 \\ -t_0 & 2t_0 \end{bmatrix} \tag{4.22}$$

$$[\beta] = \begin{bmatrix} 0 & 0 \\ -t_0 & 0 \end{bmatrix} \tag{4.23}$$

The reduced Hamiltonian matrix is then given by:

$$[h(k)] = \begin{bmatrix} 2t_0 & -t_0(1 + e^{-ika}) \\ -t_0(1 + e^{ika}) & 2t_0 \end{bmatrix} \tag{4.24}$$

The eigenvalues of the $[h(k)]$ matrix and hence the dispersion relation is:

$$E(k) = 2t_0(1 \pm \cos(ka/2)) \tag{4.25}$$

The dispersion relation is shown in Fig.(4.11b). This dispersion relation seems different from that we obtained using the single atom unitcell. Actually, they are the same. We just have to shift upper branch to the left and to the right by a distance equal to the Brillouin zone length to obtain the original band diagram for this problem. This is similar to what we have done with the CNT band structure.

The velocity matrix in this case is given by:

$$[v(k)] = \begin{bmatrix} 0 & -t_0 e^{-ika} \\ -t_0 e^{ika} & 0 \end{bmatrix} \tag{4.26}$$

We have two eigenvalues for this matrix: $\pm t_0$. It is clear that they are independent of k and do not agree with continuum limit velocity. Also, the two matrices $[h(k)]$ and $[v(k)]$ do not commute. This means that the problem we described in CNTs is repeated here again.
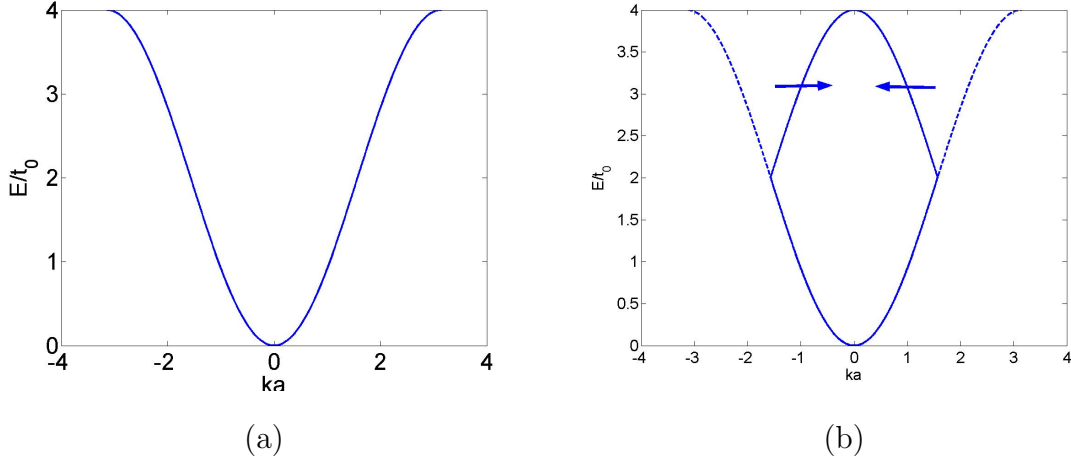
(a)   (b)

Figure 4.11: **Band diagram of simple atomic chain with different choices for unit cells (a)Containing single atom (b)Containing two atom unit cells (Solid line). The origianl band diagram (dashed line) is obtained by folding the upper two branches (solid line) to the left and to the right by**

In principle, changing the unitcell of the wire must not lead to different results. Thus, we can state that the velocity matrix $[v(k)]$ can be considered as a velocity operator that can be used to calculate the current or the expectation values of mode velocities. However, we can not always interpret the eigenvalues of this matrix as the mode velocities of $1D$ wire. In addition, we cannot depend on the commutator $[h(k), v(k)]$ to check the coupling between different modes of a quantum wire. This concept introduced by Datta [19] can not be generalized for any system as it depends on the unitcell of the system. Generalization of this concept may lead to fake conclusions as happened with CNTs. Thus, we still need to find a method to measure the coupling between CNT modes.

4.3   Crossing current between modes

In this section we follow another track to find out the leakage current between different subbands. The current flow through the CNT at the point between

unitcells n and $n+1$ is [19]:

$$J_{n+\frac{1}{2}} = \psi_n^\dagger [v(k)] \psi_n \tag{4.27}$$

In general, the wavefunction ψ can be represented in terms of CNT modes eigenvectors u_n such that: $\psi = \sum_n a_n u_n$. Hence, we can express the current as:

$$\begin{aligned} J &= \sum_{n,n^`} a_n^* a_{n^`} \langle u_{n^`} | v(k) | u_n \rangle \\ &= \sum_n |a_n|^2 \langle u_n | v(k) | u_n \rangle + \sum_{n \neq n^`} a_n^* a_{n^`} \langle u_{n^`} | v(k) | u_n \rangle \end{aligned} \tag{4.28}$$

Thus the total current flow through the CNT consists of two components: individual mode currents $J_n = |a_n|^2 \langle u_n | v(k) | u_n \rangle$ and crossing current between the modes $J_{n,n^`} = a_n^* a_{n^`} \langle u_{n^`} | v(k) | u_n \rangle$. So, by calculating the ratio between these two components we can determine the contribution of the crossing current term to the total current. Assuming that a_n are the same for all the modes, the ratio can be expressed as follows:

$$Current\ ratio = \frac{\sum_{n \neq n^`} | \langle u_{n^`} | v(k) | u_n \rangle |}{\langle u_n | v(k) | u_n \rangle} \tag{4.29}$$

We have calculated this ratio for different modes of different CNTs and found that it is always in the order of 10^{-27} which means that the leakage currents between different subbands is negligible.

Chapter 5

Wave packet propagation in CNT

In this chapter, we prove the possibility of sending independent identities simultaneously over the CNT making use of its separate energy subbands. To the best of our knowledge, there are no previous studies regarding this topic. To simplify our analysis, we neglected electron-phonon interaction and electron-electron interaction. We also, assume that we are dealing with a defect free infinite tube in order to avoid the effect of contacts and defects.

5.1 CNT eigenvectors

The energy eigenvectors of a system like CNTs can be considered as the basic (x, y, z) axes in the real $3D$ space. So, we can represent any state vector ψ in terms of these orthogonal axes. This orthonormal set is obtained simply from the k-dependent Hamiltonian matrix $[h(k)]$. In the previous chapter we wrote the Hamiltonian matrix $[h(k)]$ of zigzag CNT and solved the eigenvalue equation:

$$[h(k)]\phi_l(k) = E_l(k)\phi_l(k) \tag{5.1}$$

where l is the subband or mode number.

Each energy eigenvalue $E_l(k)$ has a corresponding eigenvector $\phi_l(k)$. The dimensions of each eigenvector are $4n \times 1$. Each element in the vector represents

the value of the wavefunction at the corresponding atom in the unit cell. These eigenvectors represent the orthonormal basis set. So, we can write any arbitrary state vector ψ in terms of these eigenvectors using the relation:

$$\psi(x,t) = \sum_l \int_k b_l(k)\phi_l(k,x)e^{-i\frac{E_l(k)t}{\hbar}} dk \tag{5.2}$$

where $b_l(k)$ are the expansion coefficients. Note that the summation is done over the $4n$ modes.

If ψ is a single mode state vector, then equation(5.2) reduces to:

$$\psi(x,t) = \int_k b_l(k)\phi_l(k,x)e^{-i\frac{E_l(k)t}{\hbar}} dk \tag{5.3}$$

The expansion coefficient $b_l(k)$ for any energy mode is calculated using the relation:

$$b_l(k) = \int \psi(x,0)\phi_l^*(x,k)dx \tag{5.4}$$

According to our definition for CNT unit cell, we can consider it as a $1D$ discrete periodic lattice. Hence, the eigenvectors at any arbitrary lattice point sa must satisfy the relation:

$$\phi_l(sa,k) = \phi_l(0,k)e^{iksa} \tag{5.5}$$

where s is an integer and a is the distance between the CNT unit cells. Thus, equation(5.4) is modified to:

$$b_l(k) = \sum_s \psi(sa,0)\phi_l^*(0,k)e^{iksa} \tag{5.6}$$

Using equation(5.2) and equation(5.6) we can synthesize any arbitrary state vector ψ from the basis CNT eigenvectors.

5.2 Single mode wave packet synthesis

The question we want to answer in this section is:"Can we construct a Gaussian wave packet using a single CNT energy mode?". Actually, there is no direct

method to check the feasibility of this. We will start our trials by assuming coefficients $b_l(k)$ for different modes and synthesizing the corresponding packet in real space.

To choose appropriate expansion coefficients, we refer to the simple case of a $1D$ Gaussian wave packet propagating in free space with initial momentum k_0. In free space, the basis functions are plane waves ($e^{ik_x x}$) with continuous values of momentum k_x. In this case, the expansion coefficient is given by [67]:

$$b(k_x) = \sqrt{\frac{2\sigma}{\sqrt{2\pi}}} e^{-\sigma^2(k_0-k_x)^2} \tag{5.7}$$

which is a Gaussian packet in k_x-space.

We assume that the expansion coefficients $b_l(k_x)$ of different modes have the same Gaussian form we obtained in free space. Using equation(5.3), we can synthesize single mode state vectors over the CNT unit cell for different modes. Samples of the resulting wavefunction distributions are shown in Fig.(5.1-5.2) for a (9,0) CNT. As depicted in the figures, the resulting distributions are not smooth over the unit cell and are far from the Gaussian distribution we target. This problem arises from the current eigenvectors. As we declared in sec.(4.2.3), subbands arises from the quantization in the wave vector k_y. The matrix $[h(k)]$ is function only in the longitudinal wave vector k_x. Hence, the vectors arises from the Matlab calculations are not function of k_y. Thus, they do not represent the CNT subbands. So, we have to find a set of vectors that are function of both k_x and k_y. Each vector in the current set will be represented in terms of these new vectors. This illustrates the inadequate result we obtained because the vectors used are mixture from the original modes defined by k_y.

5.2.1   Alternative set of CNT eigenvectors

To form a new set of CNT eigenvectors, we use graphene eigenvectors as the seeds for CNT eigenvectors. Fig.(5.3) shows the graphene sheet with its two atoms unit cells. To find the eigenvectors of the graphene, we use $[h(k)]$ matrix
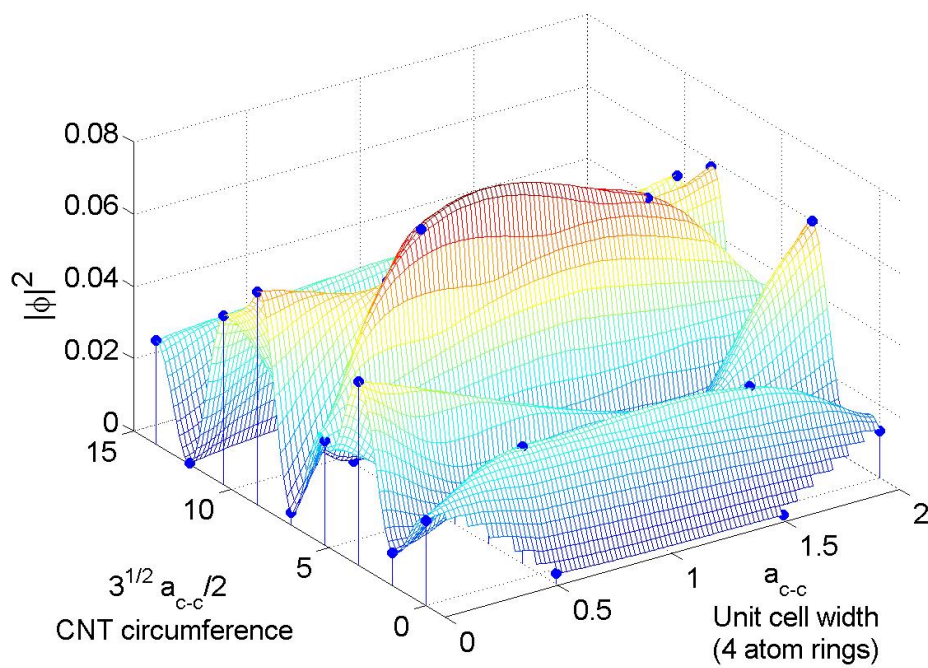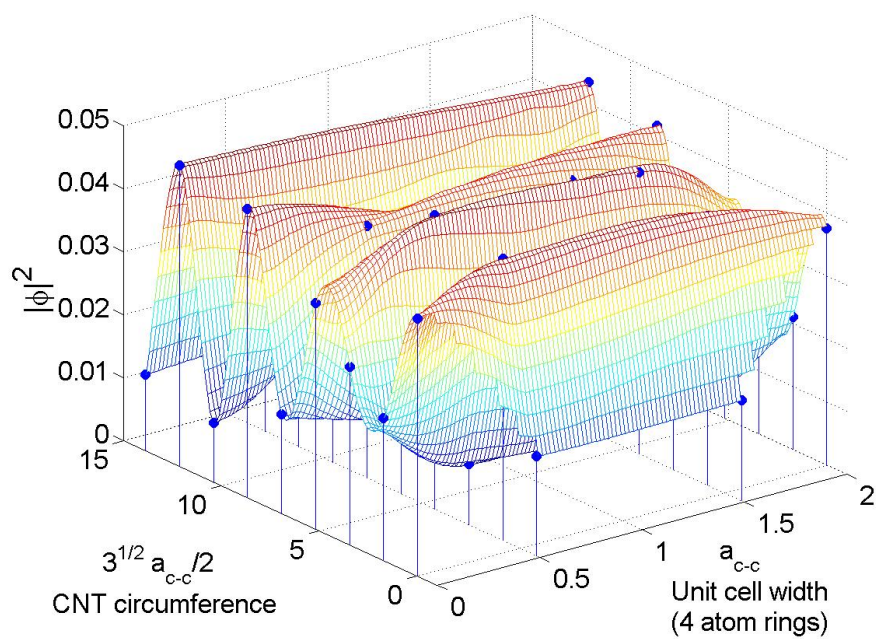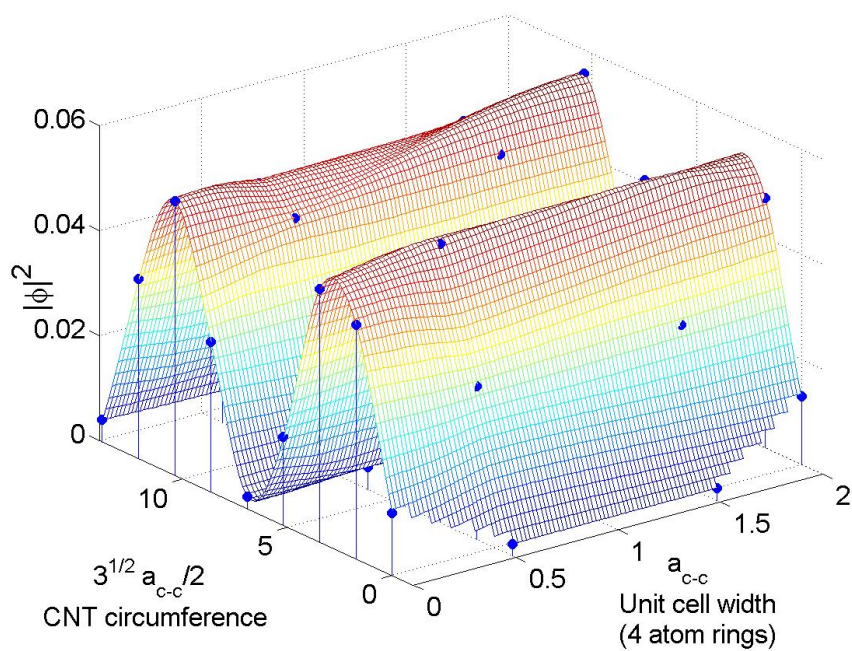
(a)
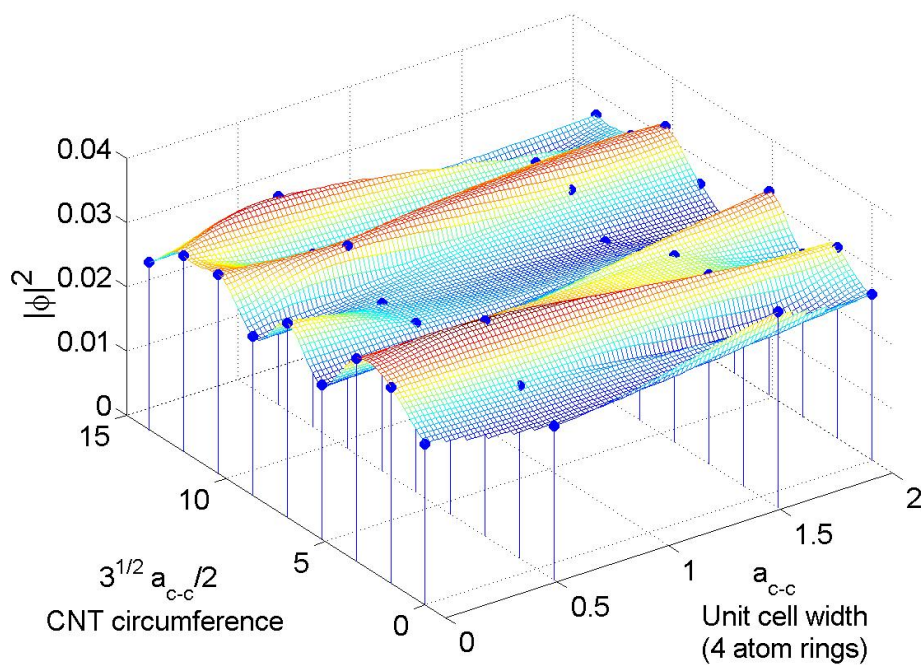
(b)

Figure 5.1: **Wavefuntion of (9,0) CNT at:(a)mode = 1 (b)mode = 9**

(a)

(b)

Figure 5.2: **Wavefuntion of (9,0) CNT at:(a)mode = 14 (b)mode = 17**
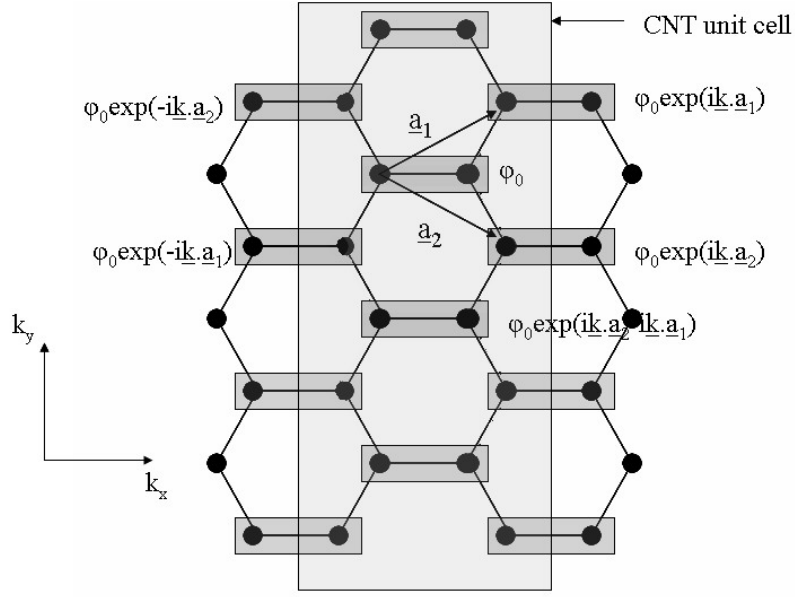
Figure 5.3: **Graphene sheet unit cells and eigenvectors**

of the graphene mentioned in chapter 2 (equation(2.10)):

$$[h(k)] = \begin{bmatrix} 0 & h_0 \\ h_0^* & 0 \end{bmatrix} \tag{5.8}$$

where $h_0 = -t(1 + e^{-i\vec{k}\cdot\vec{a_1}} + e^{-i\vec{k}\cdot\vec{a_2}} + e^{-i\vec{k}\cdot\vec{a_3}})$ and the vectors $\vec{a_1}$ and $\vec{a_2}$ are the graphene primitive vectors defined in equations(2.6,2.7).

This matrix has two eigenvalues: $\lambda = \pm\|h_0\|^2$ with two corresponding eigenvectors:

$$\phi_0 = \frac{1}{\sqrt{2}} \begin{bmatrix} 1 \\ \pm 1 \end{bmatrix} \tag{5.9}$$

From Bloch theory, we can get the vectors of any other unit cell at any arbitrary position $u\vec{a_1} + v\vec{a_2}$ by the relation:

$$\phi_n = \phi_0 e^{iu\vec{k}\cdot\vec{a_1}+iv\vec{k}\cdot\vec{a_2}} \tag{5.10}$$

where $\vec{k} \cdot \vec{a_1} = \frac{3}{2}k_x a_{c-c} + \frac{\sqrt{3}}{2}k_y a_{c-c}$ and $\vec{k} \cdot \vec{a_2} = \frac{3}{2}k_x a_{c-c} - \frac{\sqrt{3}}{2}k_y a_{c-c}$.

The final form of the eigenvector of a zigzag CNT unit cell is:

$$\phi_{0_{CNT}} = \omega \begin{bmatrix} \pm e^{-ia_{c-c}(\frac{3}{2}k_x + \frac{\sqrt{3}}{2}k_y)} \\ \pm e^{-ia_{c-c}(\frac{3}{2}k_x + 3\frac{\sqrt{3}}{2}k_y)} \\ \pm e^{-ia_{c-c}(\frac{3}{2}k_x + 5\frac{\sqrt{3}}{2}k_y)} \\ \vdots \\ 1 \\ e^{ia_{c-c}(-\sqrt{3}k_y)} \\ e^{ia_{c-c}(-2\sqrt{3}k_y)} \\ \vdots \\ \pm 1 \\ \pm e^{ia_{c-c}(-\sqrt{3}k_y)} \\ \pm e^{ia_{c-c}(-2\sqrt{3}k_y)} \\ \vdots \\ e^{ia_{c-c}(\frac{3}{2}k_x - \frac{\sqrt{3}}{2}k_y)} \\ e^{ia_{c-c}(\frac{3}{2}k_x - 3\frac{\sqrt{3}}{2}k_y)} \\ e^{ia_{c-c}(\frac{3}{2}k_x - 5\frac{\sqrt{3}}{2}k_y)} \\ \vdots \end{bmatrix}_{4n \times 1} \tag{5.11}$$

where ω is a normalization constant.

The previous vector has four groups of elements. The first group (the first n elements) represents the first carbon atoms ring in the unit cell and the second group (the next n elements) represents the second carbon atoms ring ... etc. The wavevector k_x can take any value. Typically, we take it in the range $-\frac{2\pi}{a}$ to $\frac{2\pi}{a}$ which are the boundaries of the graphene Brillouin zone. This is not the case for k_y. Due to the rolling of graphene sheet in y direction, the wavevector k_y must satisfy the following condition:

$$\begin{aligned} n\sqrt{3}a_{c-c}k_y &= 2\nu\pi \\ k_y &= \frac{2\nu\pi}{\sqrt{3}a_{c-c}n} \end{aligned} \tag{5.12}$$

where n is the CNT chirality and ν is an integer.
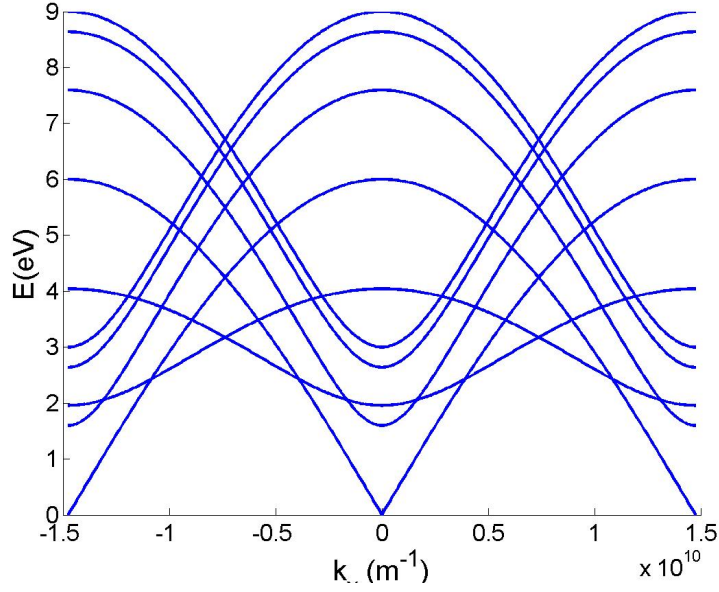
Figure 5.4: **(9,0) CNT conduction band diagram**

This quantization in k_y values is the responsible for the rising of CNT subbands. To avoid the repetition in the energy subbands, we take only the values of ν in the range: $-(n-1)$ to n. Thus the total number of eigenvectors is $2 \times 2n$ as we have two possibilities for the vector: the plus sign or the negative sign in addition to the $2n$ possible values for k_y. Vectors with positive sign corresponds to conduction band modes, while vectors with negative sign corresponds to valence band modes.

This group of vectors are also eigenvectors for the Hamiltonian $[h(k)]$ of the CNT. So, to check the validity of this set of eigenvectors, we will extract the dispersion relation of the CNT using the eigenvalue equation as follows:

$$E_l(k) = \frac{|[h(k)]\phi_l(k)|}{|\phi(k)|} \tag{5.13}$$

The conduction band of a (9,0) CNT produced by this calculation is shown in Fig.(5.4). The results are identical to those we obtained earlier in the thesis.

This new set of eigenvectors is much better than those we obtained numerically

using Matlab. The current vectors are expressed analytically. Besides, they consists only of exponential terms. This simplifies the process of synthesizing and analyzing state vectors in terms of these vectors as the process will be like simple Fourier transform.

5.2.2 Single mode Gaussian packet

Now, we will use the new set of eigenvectors we developed to construct a single mode Gaussian packet. The Gaussian expansion coefficient $b_l(k)$ are those of equation(5.7). To synthesize the packet in the real space we use the equation:

$$\psi(sa,t) = \int b_l(k_x)\phi_l(k_x)e^{ik_x sa}e^{-i\frac{E_l(k_x)t}{\hbar}}dk_x \qquad (5.14)$$

This equation constructs the state vector ψ using only the mode number l.

The distribution of the resulting wavefunction over the unrolled surface of a (9,0) CNT is shown in Fig.(5.5). The figure shows a perfect bell shaped packet uniformly distributed around the CNT circumference. This result is common for any mode number. Hence, we finally could construct a single mode wave packet.

5.2.3 Wave packet engineering

There is an inverse proportionality between the width of the packet ψ in free space and the width of its expansion coefficient $b_l(k)$ in k-space. Increasing the width of $b_l(k)$ in k-space reduces the width of the resulting packet in real space and vice versa. Fig.(5.6-5.7) show two cases of Gaussian packets with standard deviation equals to $100a_{c-c}$ and $20a_{c-c}$ respectively. Both packets has initial momentum $k_0 = \frac{\pi}{2a}$.

The current wave packet is equally distributed over the CNT circumference and we will refer to it as a wrapped around packet. To localize it at certain location on the circumference, we consider it as a multiplication of two wave
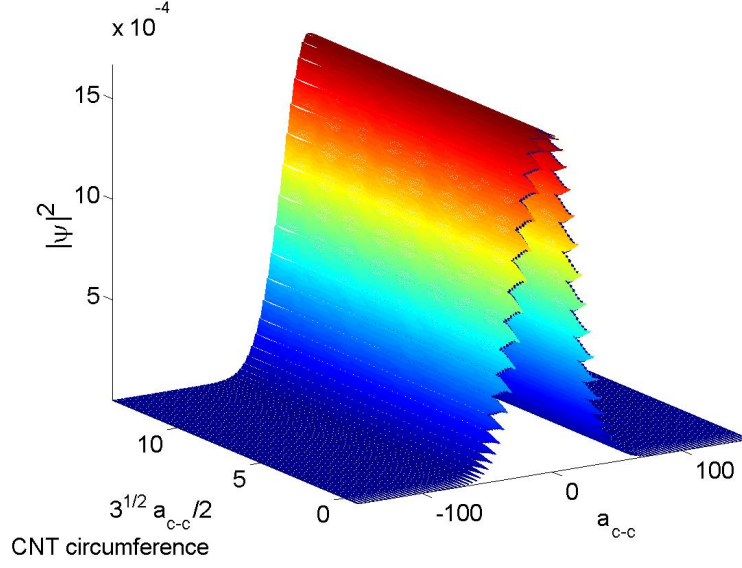
Figure 5.5: **Bill shaped wave packet over the CNT surface**

packets in x and y direction:

$$\psi(x,y) = \psi_x(x)\psi_y(y) \tag{5.15}$$

In the present case, the packet has two expansion coefficients: $b(k_x)$ and $b(k_y)$. the coefficient $b(k_x)$ remains the same Gaussian one we stated before. To find a suitable expression for $b(k_y)$ we assume that we have a Gaussian function in the y direction (CNT circumference direction):

$$\psi(y) = \frac{1}{\sigma^{1/2}(2\pi)^{1/4}}e^{-(y-y_0)^2/4\sigma^2} \tag{5.16}$$

where y_0 determines the position of the packet center over the tube circumference.

The corresponding coefficient takes the same form in equation(5.7):

$$b(k_y) = \sqrt{\frac{2\sigma}{\sqrt{2\pi}}}e^{-\sigma^2 k_y^2} \tag{5.17}$$

This is different for $b(k_x)$ in that it does not have initial momentum and that the wavevector k_y is quantized and can take only the values stated in equation(5.12).
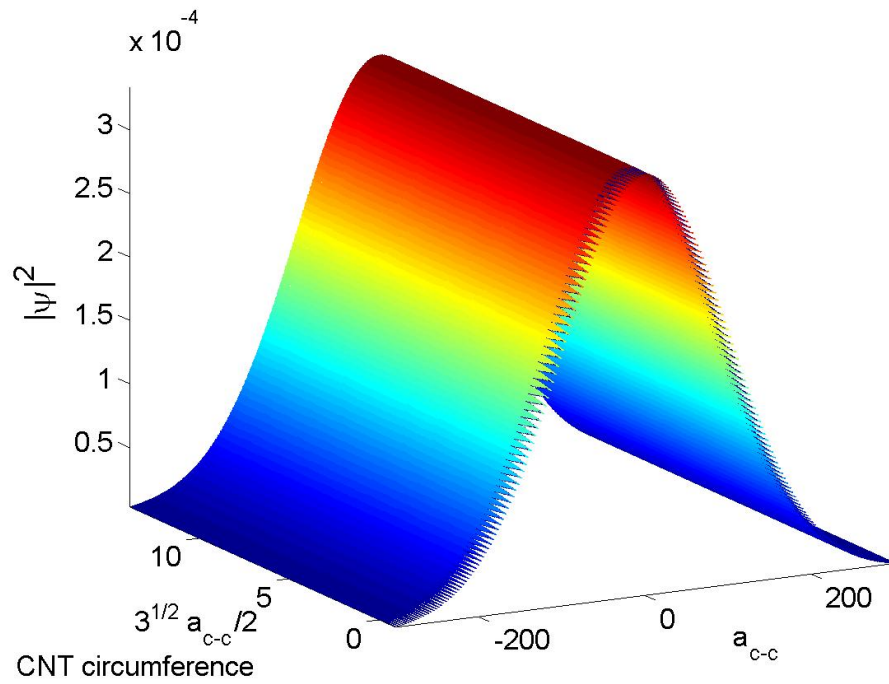
(a)
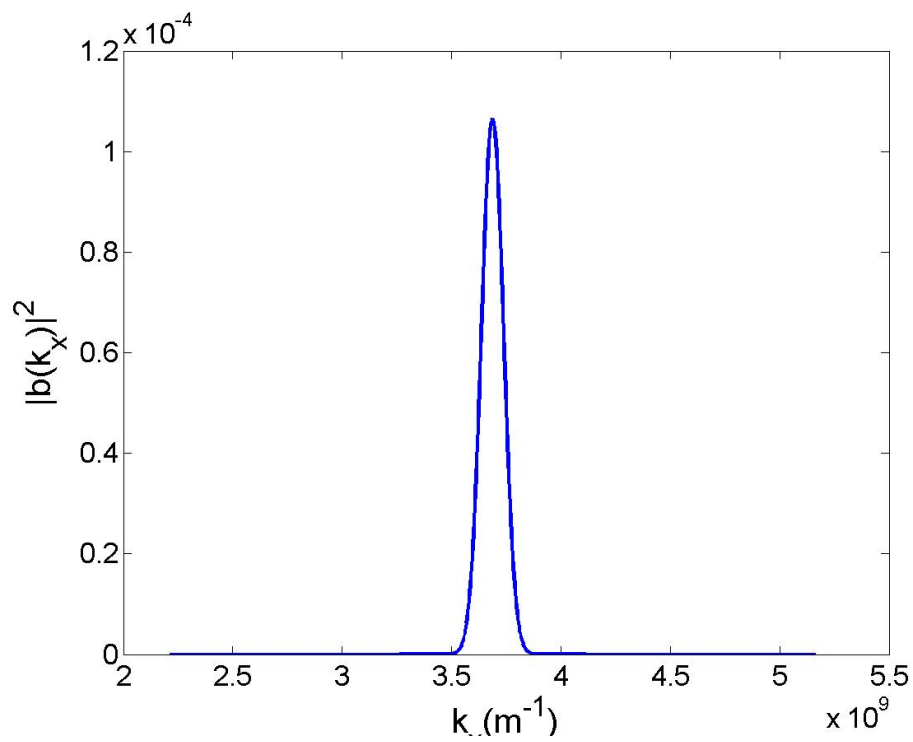
(b)

Figure 5.6: **(a)Gaussian packet in real space ($\sigma = 100a_{c-c}$)(b)Corresponding expansion coefficient $|b(k_x)|^2$ in k_x space**

(a)

(b)

Figure 5.7: **(a)Gaussian packet in real space ($\sigma = 20a_{c-c}$) (b)Corresponding expansion coefficient $|b(k_x)|^2$ in k_x space**

The process of synthesizing the final wave packet is similar to inverse $2D$ Fourier transform. The final packet is obtained using the relation:

$$
\begin{aligned}
\psi(sa, y, t) &= \int \sum_{k_y} b(k_x)b(k_y)\phi_l(k_x, k_y)e^{ik_x sa}e^{-i\frac{E_\nu(k_x)t}{\hbar}}dk_x \\
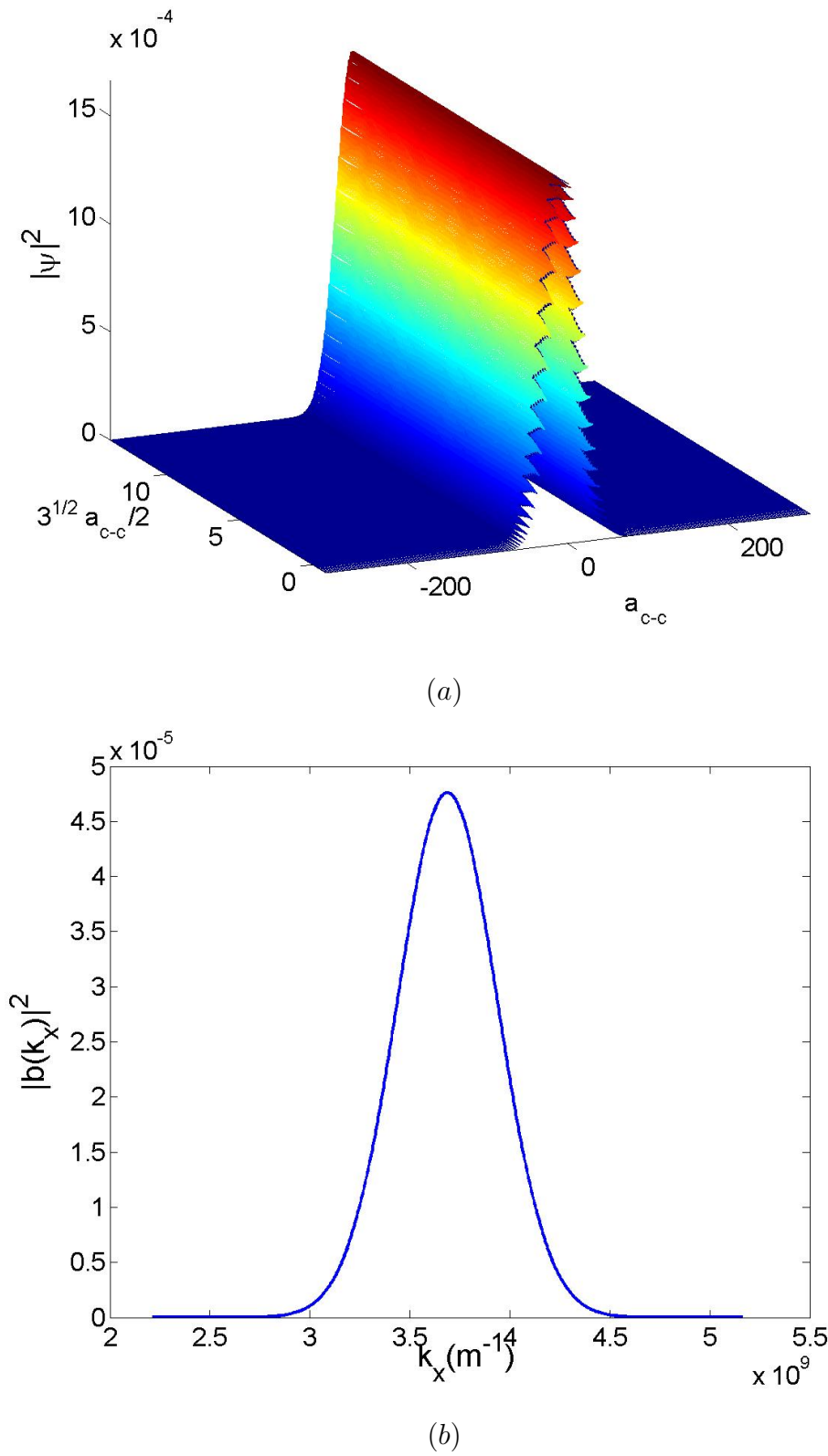&= \int \sum_{\nu} b(k_x)b(\nu)\phi_l(k_x, \nu)e^{ik_x sa}e^{-i\frac{E_\nu(k_x)t}{\hbar}}dk_x \qquad (5.18)
\end{aligned}
$$

where $k_y = \frac{2\nu\pi}{\sqrt{3}a_0 n}$.

An example of the resulting packet is shown in Fig.(5.8) for a (19,0) CNT. The figure also shows the expansion coefficient versus the integer ν that represents the mode number. We note that this packet is no more a single mode one as it contains different components of k_y.

5.2.4   Multiple signals multiplexing

In order to transmit multiple signals simultaneously over the same CNT, we suggest two possible techniques:

Energy Multiplexing

As we showed, we can construct single mode wave packets that can propagate in a certain subband. Thus, we can transmit various signals simultaneously over different subbands without interference between these signals. In this case, we will need to develop receivers that can differentiate between signals according to there energy mode.

Space Multiplexing

We suggest that we can divide the CNT surface into communication channels. We can divide the CNT circumference into equal portions and send signals over each portion independently using the pulsed packet. Hence, dividing the CNT surface into 4 portions means that we can transmit 4 bits simultaneously over
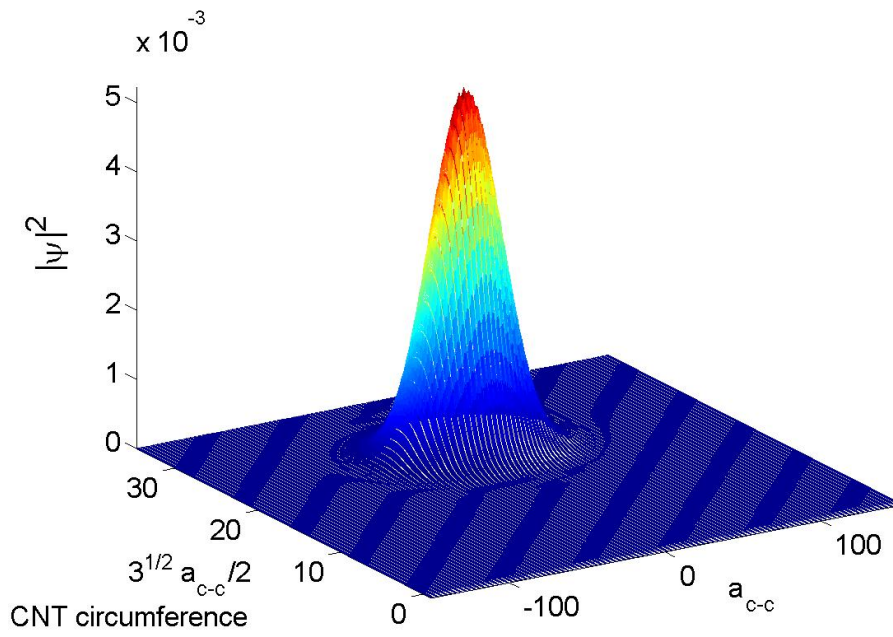
(a)
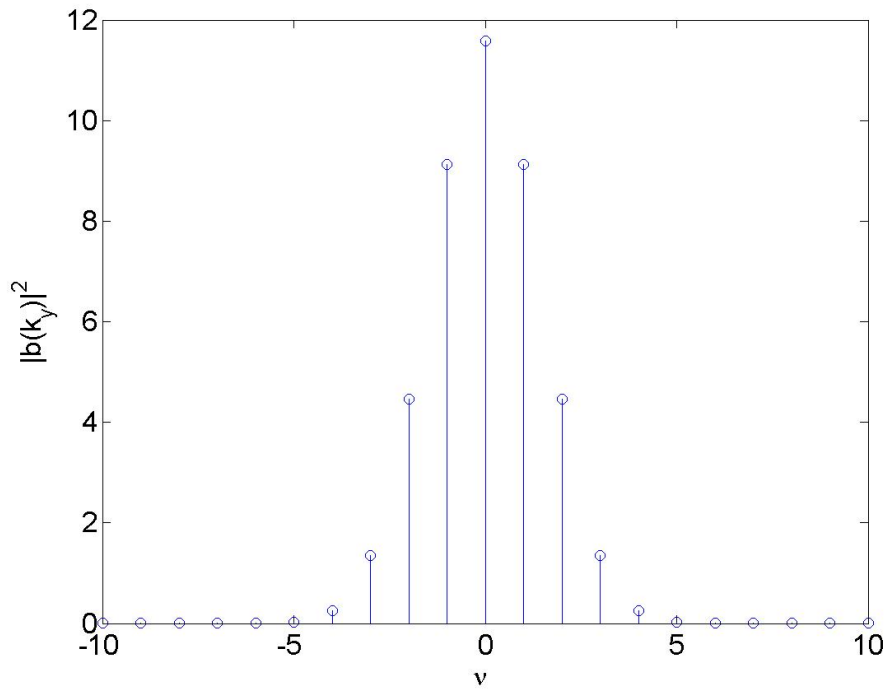
(b)

Figure 5.8: **(a)Modified Gaussian packet in real space (b)Corresponding expansion coefficient** $|b(k_y)|^2$ **vs** ν**.**
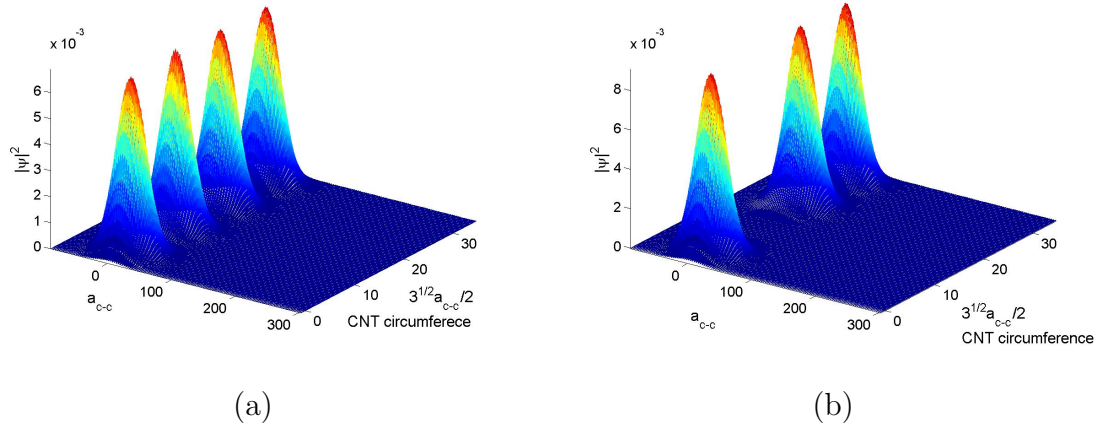
Figure 5.9: **(a)CNT surface divided into 4 portions with 4 pulsed packets representing 4 bits: (a)1111 (b)1011.**

the CNT. Fig.(5.9) shows an example for this possible communication technique. Increasing the number of bits transmitted is possible by generating narrower pulses. Narrower pulses will suffer from greater dispersion as it will contains larger number of propagating modes. Studies should be conducted to find the optimal diameter and bit number combination.

5.2.5   Wave packet propagation

To transmit information along the CNT, we need to know the distance over which information can move before lost. In the system of CNT, we do not have a standard measurement to specify when the information is lost. The threshold point after which we lose transmission depends on the system noise arising from system nonidealities such as electron-phonon interaction. Such nonidealities are beyond the scope of this study. Here we just shed light on the packet behavior as it propagates along the tube.

The wrapped around packet propagates with small spreading in the direction of motion. Fig.(5.10) shows the packet at different time instants. This packet can travel for relatively long distances. However, we can not make spatial multiplexing

Figure 5.10: **Wrapped around packet at** $t = 0fs$**,** $t = 100fs$ **and** $t = 200fs$**.**

with other packets that may carry other information.

The behavior of the pulsed shape packet is different from the wrapped around packet. This packet is not a single mode packet as it contains different components of k_y. This results in a significant spreading to the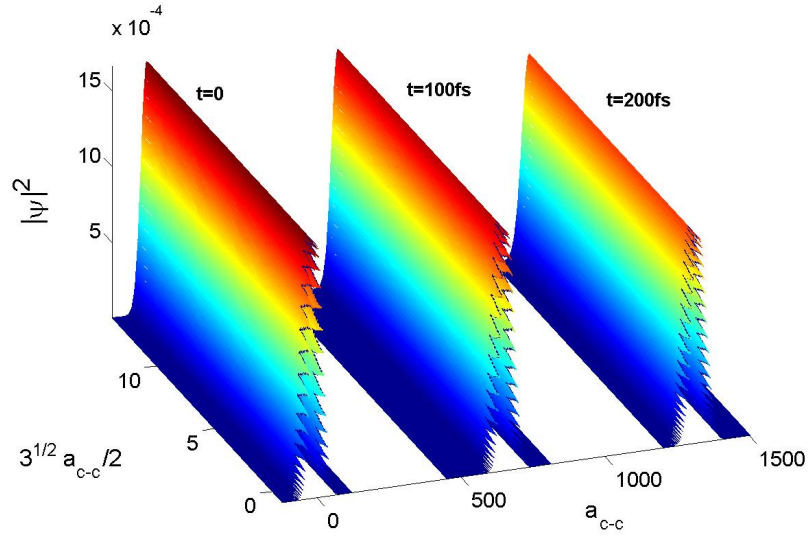 packet in the y direction (CNT circumference). The velocity of the packet in the x direction is determined by the the initial momentum k_0. As there is no initial momentum in the y direction, the packet splits and moves to the left and to the right as depicted in Fig.(5.11-5.14). However, due to the circular cross section of the tube, the packet is collected again after certain period of time determined by the mode velocities and tube diameter. In our simulations of for (19,0) CNT this period is $65fs$.

5.3 Conclusion

In this chapter, we could successfully construct a single mode bell shaped wrapped around packet propagating along the CNT. This packet is a single mode one. This makes it suitable for long distance transmission. However, we can not send dif-
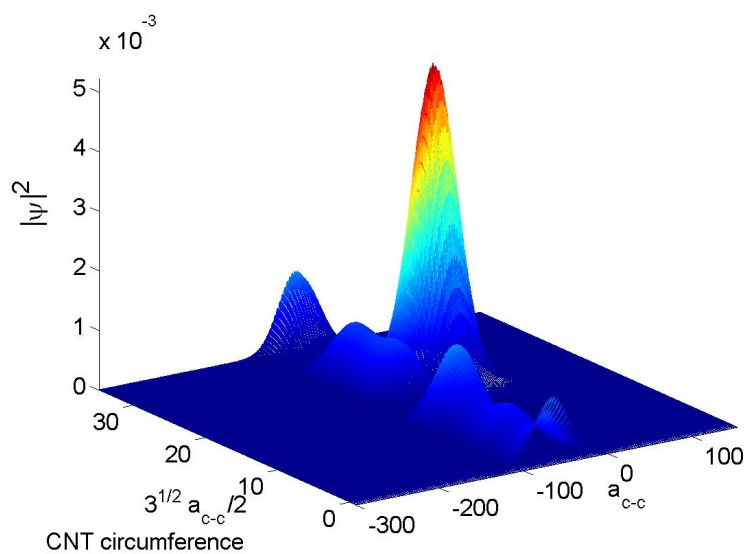
Figure 5.11: **Pulsed packet at** $t = 20fs$
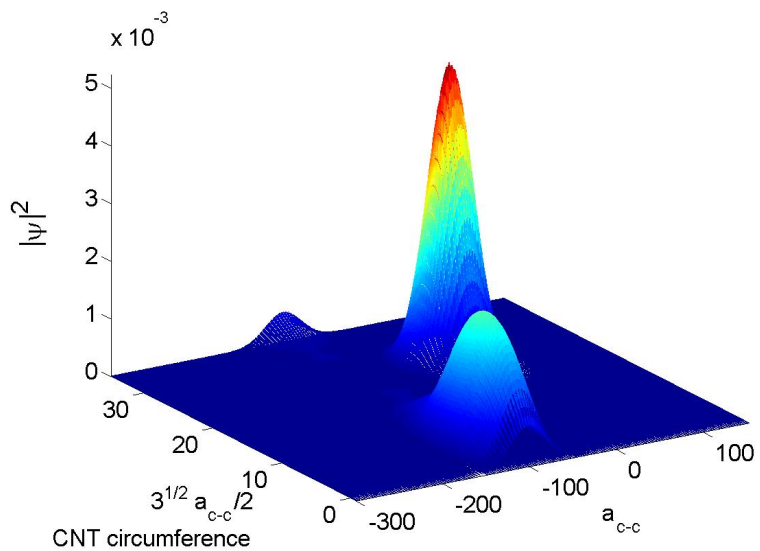
Figure 5.12: **Pulsed packet at** $t = 30fs$
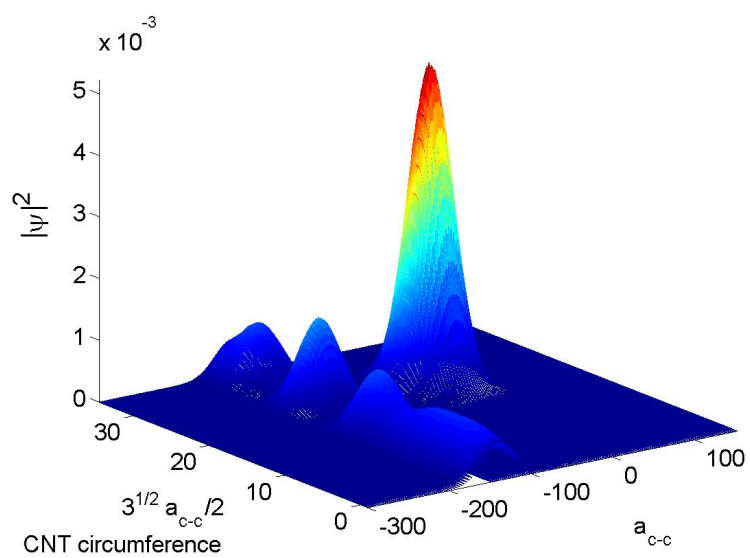
Figure 5.13: **Pulsed packet at** $t = 40fs$
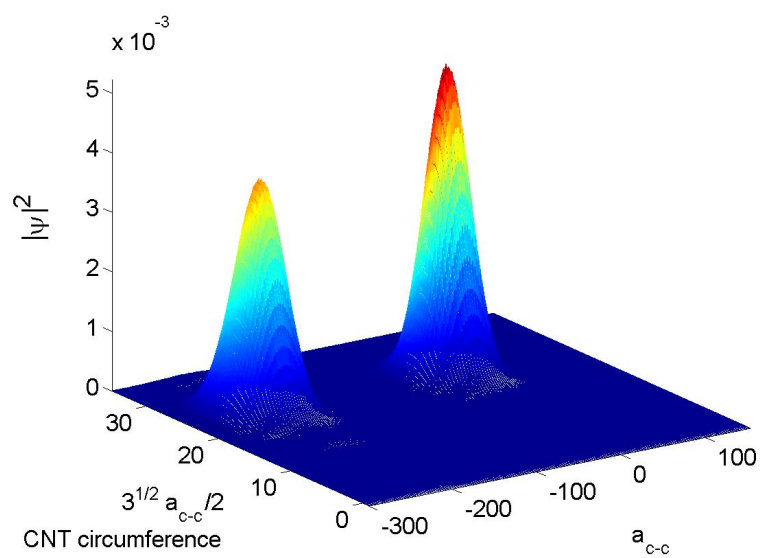
Figure 5.14: **Pulsed packet at** $t = 65fs$

ferent packets simultaneously as we will not be able to extract them. This will be possible if we find a method that can differentiate between the packets according to their modes. We can send simultaneous packets using spatial multiplexing. In this case, we should use pulsed shape packet. Unfortunately, this packet type suffers from strong spreading because it is not a single mode one.

Chapter 6

Conclusion and future work

This work investigates the possible contributions of CNTs to the future electronics in short and long terms. In the short term, CNTs will enhance the performance of traditional CMOS transistors. We investigated the performance of Carbon Nanotube Field Effect Transistors in digital circuits. We chose SB CNTFET because it is the most robust type of CNTFET as it was fabricated and verified by many research groups. This transistor showed acceptable performance in digital circuits and satisfied high performance applications requirements specified by ITRS. The performance we get for SB CNTFET is not as good as we expect compared to the extraordinary properties of CNTs.

This conclusion is based on the results we obtained for the inverter circuit. To get more verified results, this study should be extended to cover more complex logic gates. In addition, other types of the CNTFET family should be also evaluated in the same way.

Then we changed our study scope to investigate the possibility of making novel CNT wires that can carry multiple signals like optical fiber. Our study showed that we can construct a single mode propagating packet over the CNT surface. We argue the possibility of making spatial multiplexing over the nanotube surface to transmit multiple packets simultaneously.

More studies should be conducted to suggest possible multiplexing schemes

and obtain the most efficient one. Besides, this study should be extended to other types of CNTs as we were concentrating on zigzag CNTs. Transmitters and receivers of mentioned wave packets need extensive studies.

Actually, the basic contribution of this study is that it shed light on the hidden capabilities of the CNTs. It also directs the researchers to think about nontraditional applications of CNTs.

References

[1] G. E. Moore, "Cramming more components onto integrated circuits," *Electronics*, vol. 38, Apr. 1965.

[2] "International technology roadmap for semiconductors," 2007. Available online: `http://www.itrs.net/Links/2007ITRS/Home2007.htm`.

[3] S.-H. Lo, D. A. Buchanan, Y. Taur, and W. Wang, "Quantum-mechanical modeling of electron tunneling current from the inversion layer of ultra-thin-oxide nMOSFETs," *IEEE Electron Device Letters*, vol. 18, May 1997.

[4] H.-S. P. Wong, "Beyond the conventional transistor," *IBM Journal of Research and Development*, vol. 46, Mar. 2002.

[5] T. Kaueraufa, B. Govoreanua, R. Degraevea, G. Groesenekena, and H. Maesa, "Scaling CMOS: Finding the gate stack with the lowest leakage current," *Solid-State Electronics*, vol. 49, Feb. 2005.

[6] M. Ieong, V. Narayanan, D. Singh, A. Topol, V. Chan, and Z. Ren, "Transistor scaling with novel materials," *Materials today*, vol. 9, June 2006.

[7] B. G. Streetman and S. Banerjee, *Solid State electronic Devices*. Prentice Hall, 2000.

[8] R. Chau, S. Datta, and A. Majumdar, "Opportunities and challenges of III-V nanoelectronics for future high-speed, low-power logic applications," *IEEE Compound Semiconductor Integrated Circuit Symposium (CSIC)*, Nov. 2005.

[9] R. Chau, M. Doczy, B. Doyle, S. Datta, G. Dewey, J. Kavalieros, B. Jin, M. Metz, A. Majumdar, and M. Radosavljevic, "Advanced CMOS transistors in the nanotechnology era for high-performance, low-power applications," *Proceedings of the 7th International Conference on Solid State and Integrated Circuit Technology*, vol. 1, pp. 26 – 30, Oct. 2004.

[10] H. Wakabayashi, S. Yamagami, N. Ikezawa, A. Ogura, M. Narihiro, K. ichi Arai, Y. Ochiai, K. Takeuchi, T. Yamamoto, and T. Mogami, "Sub-10-nm planar-bulk-CMOS devices using lateral junction control," *IEEE International Electron Devices Meeting, 2003. Technical Digest.*, vol. 9, Dec. 2003.

[11] K. K. Likharev, "CMOL: A new concept for nanoelectronics," in *12th Int. Symp. on Nanostructures Physics and Technology (St. Petersburg, Russia)*, 2004.

[12] K. K. Likharev, "Electronics below 10 nm," in *Nano and Giga Challenges in Microelectronics* (J. Greer, A. Korkin, and J. Labanowski, eds.), pp. 27–68, 2003.

[13] S. Iijima, "Helical microtubules of graphitic carbon," *Nature*, vol. 354, Nov. 1991.

[14] Y. L. Mao, X. H. Yan, Y. Xiao, J. Xiang, Y. R. Yang, and H. L. Yu, "The viability of 0.3 nm diameter carbon nanotubes," *Nanotechnology*, vol. 15, pp. 1000 – 1003, Aug. 2004.

[15] X. Zhao, Y. Liu, S. Inoue, T. Suzuki, R. Jones, and Y. Ando, "Smallest carbon nanotube is 3 in diameter," *Physical Review Letters*, vol. 92, Mar. 2004.

[16] L. X. Zheng, M. J. OConnel, S. K. Doorn, X. Z. Liao, Y. H. Zhao, E. A. Akhadov, M. A. Hoffbauer, B. J. Roop, Q. X. Jia, R. C. Dye, D. E. Peterson, S. M. Huang, J. Liu, and Y. T. Zhu, "Ultralong single-wall carbon nanotubes," *Nature Materials*, vol. 3, Oct. 2004.

[17] R. Saito, G. Dresselhaus, and M. S. Dresselhaus, *Physical Properties of Carbon Nanotubes.* Imperial College Press, 1997.

[18] M. S. Dresselhaus, G. Dresselhaus, and P. Avouris, *Carbon Nanotubes: Synthesis, Structure, Properties and Apllications.* Springer, 2001.

[19] S. Datta, *Quantum Transport: Atom to Transistor.* Cambridge University Press,, 2005.

[20] J. Guo, *Carbon Nanotube Electronics: Modeling, Physics, and Applications.* PhD thesis, Purdue University, 2004.

[21] P. Avouris, J. Appenzeller, R. Martel, and S. J. Wind, "Carbon nanotube electronics," *Proceedings of the IEEE*, vol. 91, Nov. 2003.

[22] J. W. Mintmire and C. T. White, "Electronic and structural properties of carbon nanotubes," *Carbon*, vol. 33, no. 7, 1995.

[23] M. Ouyang, J.-L. Huang, and C. M. Lieber, "Fundamental electronic properties and applications of single-walled carbon nanotubes," *Accounts of Chemical Research*, vol. 35, Aug. 2002.

[24] J. Guo, S. Datta, M. Lundstrom, and M. Anantram, "Towards multi-scale modeling of carbon nanotube transistors," *International Journal for Multiscale Computational Engineering, special issue on multiscale methods for emerging technologies*, vol. 2, 2004.

[25] Z. Yao, C. L. Kane, and C. Dekker, "High-field electrical transport in single-wall carbon nanotubes," *Physical Review Letters*, vol. 84, Mar. 2000.

[26] J.-Y. Park, S. Rosenblatt, Y. Yaish, V. Sazonova, H. Ustunel, S. Braig, T. A. Arias, P. W. Brouwer, and P. L. McEuen, "Electron-phonon scattering in metallic single-walled carbon nanotubes," *Nano Letters*, vol. 4, Feb. 2004.

[27] A. Javey, J. Guo, M. Paulsson, Q. Wang, D. Mann, M. Lundstrom, and H. Dai, "High-field quasiballistic transport in short carbon nanotube," *Physical Review Letters*, vol. 92, Mar. 2004.

[28] P. Sundqvist, F. J. Garcia-Vidal, F. Flores, M. Moreno-Moreno, C. Gomez-Navarro, J. S. Bunch, and J. Gomez-Herrero, "Voltage and length-dependent phase diagram of the electronic transport in carbon nanotubes," *Nano Letters*, vol. 7, Feb. 2007.

[29] S. Tomonaga, "Remarks on bloch's method of sound waves applied to many-fermion problems," *Progress of Theoretical Physics*, vol. 5, June 1950.

[30] J. M. Luttinger, "An exactly solvable model of a many-fermion system," *Journal of Mathematical Physics*, vol. 4, no. 9, 1963.

[31] J. Voit, "One-dimensional fermi liquids," *Reports on Progress in Physics*, vol. 58, Sept. 1995.

[32] A. J. Schofield, "Non-fermi liquids," *Contemporary Physics*, vol. 40, Mar. 1999.

[33] M. Bockrath, D. H. Cobden, J. Lu, A. G. Rinzler, R. E. Smalley, L. Balents, and P. L. McEuen, "Luttinger-liquid behaviour in carbon nanotubes," *Nature*, vol. 397, Feb. 1999.

[34] Z. Yao, H. W. C. Postma, L. Balents, and C. Dekker, "Carbon nanotube intramolecular junctions," *Nature*, vol. 402, Nov. 1999.

[35] R. Chau, S. Datta, M. Doczy, B. Doyle, B. Jin, J. Kavalieros, A. Majumdar, M. Metz, and M. Radosavljevic, "Benchmarking nanotechnology for high-performance and low-power logic transistor applications," *IEEE Transactions on Nanotechnology*, vol. 4, Mar. 2005.

[36] A. G. Rinzler, J. H. Hafner, P. Nikolaev, P. Nordlander, D. T. Colbert, R. E. Smalley, L. Lou, S. G. Kim, and D. Tomanek, "Unraveling nanotubes: Field

emission from an atomic wire," *Science*, vol. 269, pp. 1550 – 1553, Sept. 1995.

[37] G. Amaratunga, "Watching the nanotube," *IEEE Spectrum*, vol. 40, pp. 28 – 32, Sept. 2003.

[38] B. Q. Wei, R. Vajtai, and P. M. Ajayan, "Reliability and current carrying capacity of carbon nanotubes," *Applied Physics Letters*, vol. 79, Mar. 2001.

[39] G. W. Hanson, "Fundamental transmitting properties of carbon nanotube antennas," *IEEE Transactions on Antennas and Propagation*, vol. 53, Nov. 2005.

[40] J. Hao and G. W. Hanson, "Infrared and optical properties of carbon nanotube dipole antennas," *IEEE Transactions on Nanotechnology*, vol. 5, Nov. 2006.

[41] P. J. Burke, S. Li, and Z. Yu, "Quantitative theory of nanowire and nanotube antenna performance," *IEEE Transactions on Nanotechnology*, vol. 5, July 2006.

[42] A. A. Essawi, H. A. H. Fahmy, and N. H. Rafat, "Characterization of a coaxial mid-gap SB CNTFET inverter," *Microprocesses and Nanotechnology, 2007 Digest of Papers*, Nov. 2007.

[43] S. J. Tans, A. R. M. Verschueren, and C. Dekker, "Room-temperature transistor based on a single carbon nanotube," *Nature*, vol. 393, May 1998.

[44] C. P. Auth and J. D. Plummer, "Scaling theory for cylindrical, fully-depleted, surrounding-gate MOSFETs," *IEEE Electron Device Letters*, vol. 18, Feb. 1997.

[45] J. Guo, S. Goasguen, M. Lundstrom, and S. Datta, "Metal-insulator-semiconductor electrostatics of carbon nanotubes," *Applied Physics Letters*, vol. 81, Aug. 2002.

[46] S. Heinze, J. Tersoff, R. Martel, V. Derycke, J. Appenzeller, and P. Avouris, "Carbon nanotubes as schottky barrier transistors," *Physical Review Letters*, vol. 89, Sept. 2002.

[47] M. Radosavljevic, S. Heinze, J. Tersoff, and P. Avouris, "Drain voltage scaling in carbon nanotube transistors," *Applied Physics Letters*, vol. 83, Sept. 2003.

[48] Z. Chen, J. Appenzeller, J. Knoch, Y. ming Lin, and P. Avouris, "The role of metal-nanotube contact in the performance of carbon nanotube field-effect transistors," *Nano Letters*, vol. 5, June 2005.

[49] A. Javey, R. Tu, D. B. Farmer, J. Guo, R. G. Gordon, and H. Dai, "High performance n-type carbon nanotube field-effect transistors with chemically doped contacts," *Nano Letters*, vol. 5, no. 2, pp. 345 – 348, 2005.

[50] A. Javey, J. Guo, D. B. Farmer, Q. Wang, D. Wang, R. G. Gordon, M. Lundstrom, and H. Dai, "Carbon nanotube field-effect transistors with integrated ohmic contacts and high-k gate dielectrics," *Nano Letters*, vol. 4, no. 3, pp. 447 – 450, 2004.

[51] J. Appenzeller, Y.-M. Lin, J. Knoch, Z. Chen, and P. Avouris, "Comparing carbon nanotube transistorsthe ideal choice: A novel tunneling device design," *IEEE Transactions on Electron Devices*, vol. 52, Dec. 2005.

[52] A. Javey, J. Guo, D. B. Farmer, Q. Wang, E. Yenilmez, R. G. Gordon, M. Lundstrom, and H. Dai, "Self-aligned ballistic molecular transistors and electrically parallel nanotube arrays," *Nano Letters*, vol. 4, no. 7, pp. 1319 – 1322, 2004.

[53] A. Hazeghi, T. Krishnamohan, and H.-S. P. Wong, "Schottky-barrier carbon nanotube field-effect transistor modeling," *IEEE Transactions on Electron Devices*, vol. 54, Mar. 2007.

[54] K. Natori, Y. Kimura, and T. Shimizu, "Characteristics of a carbon nanotube field-effect transistor analyzed as a ballistic nanowire field-effect transistor," *Journal of Applied Physics*, vol. 97, Jan. 2005.

[55] A. Hazeghi, T. Krishnamohan, and H.-S. P. Wong, "Schottky-barrier cnfet," Mar 2007. Available online: `http://www.nanohub.org/resources/2465/`.

[56] J. M. Rabey, A. Chandrakasan, and B. Nikolic, *Digital Integrated Circuits: A Design Perspective.* Pearson Education International, 2003.

[57] Z. Chen, J. Appenzeller, Y.-M. Lin, J. Sippel-Oakley, A. G. Rinzler, J. Tang, S. J. Wind, P. M. Solomon, and P. Avouris, "An integrated logic circuit assembled on a single carbon nanotube," *Science*, vol. 311, p. 1735, mar 2006.

[58] Y. Lu, S. Bangsaruntip, X. Wang, L. Zhang, Y. Nishi, and H. Dai, "DNA functionalization of carbon nanotubes for ultrathin atomic layer deposition of high k dielectrics for nanotube transistors with 60 mv/decade switching," *Journal of American Chemical Society*, vol. 128, pp. 3518–3519, mar 2006.

[59] P. J. Burke, "AC performance of nanoelectronics: towards a ballistic THz nanotube transistor," *Solid-State Electronics*, vol. 48, p. 19811986, jun 2004.

[60] P. J. Burke, "Luttinger liquid theory as a model of the gigahertz electrical properties of carbon nanotubes," *IEEE Transactions on Nanotechnology*, vol. 1, Sept. 2002.

[61] K. Nabors and J. K. White, "FASTCAP: A multipole-accelerated 3-d capacitance extraction program," *IEEE Transactions on Computer-Aided Design of Integrated Circuits and Systems*, vol. 10, p. 14471459, nov 1991.

[62] A. Keshavarzi, A. Raychowdhury, J. Kurtin, K. Roy, and V. De, "Carbon nanotube field-effect transistors for high-performance digital circuitstran-

sient analysis, parasitics, and scalability," *IEEE Transactions on Electron Devices*, vol. 53, Nov. 2006.

[63] J. Appenzeller, J. Knoch, M. Radosavljevic, and P. Avouris, "Multimode transport in schottky-barrier carbon-nanotube field-effect transistors," *Physical Review Letters*, vol. 92, jun 2004.

[64] A. Svizhenko, M. P. Anantram, and T. R. Govindan, "Ballistic transport and electrostatics in metallic carbon nanotubes," *IEEE Transactions on Nanotechnology*, vol. 4, pp. 557 – 562, sep 2005.

[65] L. Yang, M. P. Anantram, and J. P. Lu, "Band-gap change of carbon nanotubes: Effect of small uniaxial and torsional strain," *Physical Review B*, vol. 60, pp. 13874–13878, nov 1999.

[66] Y. Yoon, D. Kienle, J. K. Fodor, G. Liang, A. Matsudaira, G. Klimeck, and J. Guo, "CNTbands 2.0," Dec 2006. Available online: `http://www.nanohub.org/resources/1838/`.

[67] R. L. Liboff, *Introductory Quantum Mechanics*. Addison-wesley, 2002.